Epitaxial growth and characterization of NiMnSb layers for novel spintronic devices

Dissertation zur Erlangung des
naturwissenschaftlichen Doktorgrades der
Julius-Maximilians-Universität Würzburg

vorgelegt von
Florian Lochner
aus Bayreuth

Würzburg
2011

Eingereicht am: .....
bei der Fakultät für Physik und Astronomie

1. Gutachter: Prof. Dr. Laurens W. Molenkamp
2. Gutachter: Prof. Dr. Vladimir Dyakonov
der Dissertation.

1. Prüfer: Prof. Dr. Laurens W. Molenkamp
2. Prüfer: Prof. Dr. Vladimir Dyakonov
3. Prüfer: Prof. Dr. Björn Trauzettel
im Promotionskolloquium.

Tag des Promotionskolloquium: .....

Doktorurkunde ausgehändigt am: .....

Contents

List of Abbrevations

AFM - **A**tomic **F**orce **M**icroscope
CIP - **C**urrent-**I**n-**P**lane
CPP - **C**urrent-**P**erpendicular-to-**C**urrent
FMR - **F**erromagnet **R**esonance
GIXRD - **G**racing **I**ncident **X**-**R**ay **D**iffraction
GMR - **G**iant **M**agneto **R**esistance
HRXRD - **H**igh **R**esolution **X**-**R**ay **D**iffraction
MBE - **M**olecular **B**eam **E**pitaxy
MOKE - **M**agneto-**O**ptical **K**err **E**ffect
MRAM - **M**agnetoresistive **R**andom **A**ccess **M**emory
MRFM - **M**agnetic **R**esonance **F**orce **M**icroscope
PID - **P**roportional-**I**ntegral-**D**erivative
RHEED - **R**eflection **H**igh **E**nergy **E**lectron **D**iffraction
RSM - **R**eciprocal **S**pace **M**ap
SEM - **S**canning **E**lectron **M**icroscope
STO - **S**pin **T**orque **O**scillator
STT - **S**pin **T**ransfer **T**orque
SQUID - **S**uperconducting **QU**antum **I**nterference **D**evice
TMR - **T**unneling **M**agneto **R**esistance
UHV - **U**ltra**h**igh **V**acuum
XRD - **X**-**R**ay **D**iffraction

List of Figures

List of Tables

1. Introduction

In recent years, many new technologies have become available for people all around the world. The amount of information increases every day. Faster computers and larger storage systems have been engineered since J. Bardeen, W.H. Brattain and W.B. Shockley developed the transistor in 1947 [Bar48]. Their technology was and still is based on the charge of electrons. At the end of the 50s of the last century, another pioneering technology was established in electric engineering.

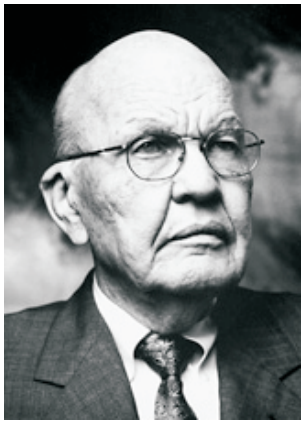

Figure 1.1.: Jack S.Kilby, * November 8, 1923 †June 20, 2005.

Jack Kilby demonstrated the first IC [1] consisting of two bipolar transistors on a Ge substrate [Kil76]. That was the starting point for processors and computers as we know them today. In 2000, he received the Nobel prize in physics for his work.

With the development of faster and more ICs per area, Gordon E. Moore predicted in the year 1965 in an article for the journal *Electronics* that every year the amount of IC on a computer chip would be doubled [Moo65]. 10 years later, he corrected his declaration, in present days known as *Moores Law*, concerning space of time up to two years (Fig.1.2). On the Intel development forum (IDF) in 2007, Moore proclaimed the termination of his law in the following 10-15 years. 6 months later Pat Gelsinger repealed Moores proposition and announced the termination of Moores law by the year 2029. The end is determined by the boundaries of physical laws. For that reason, a lot of scientists all around the globe tried to figure out new prospects for new technologies. One approach is the exploitation of the spin of the electrons in addition to their charge for transport and storage of information. Techniques exploiting the spin are summarized under the topic spintronic. The two states 0 and 1 are now not presented by charged or uncharged but spin-up and spin-down. But a spin injector with ideally 100% spin-polarized electrons is needed. Thus drove the initial interest in NiMnSb. It is a half-metallic ferromagnet with theoretical 100% spin-polarization at the Fermi edge combined with a high Curie temperature far above room temperature. These two features make NiMnSb a perfect spin injector for spintronic devices at room temperature. Starting in the 1950s till now NiMnSb is under heavy investigation not only for spin injection experiments but also because of its low magnetic damping.

The topic of this work is the epitaxial growth and characterization of NiMnSb layers for

[1] **I**ntegrated **C**ircut

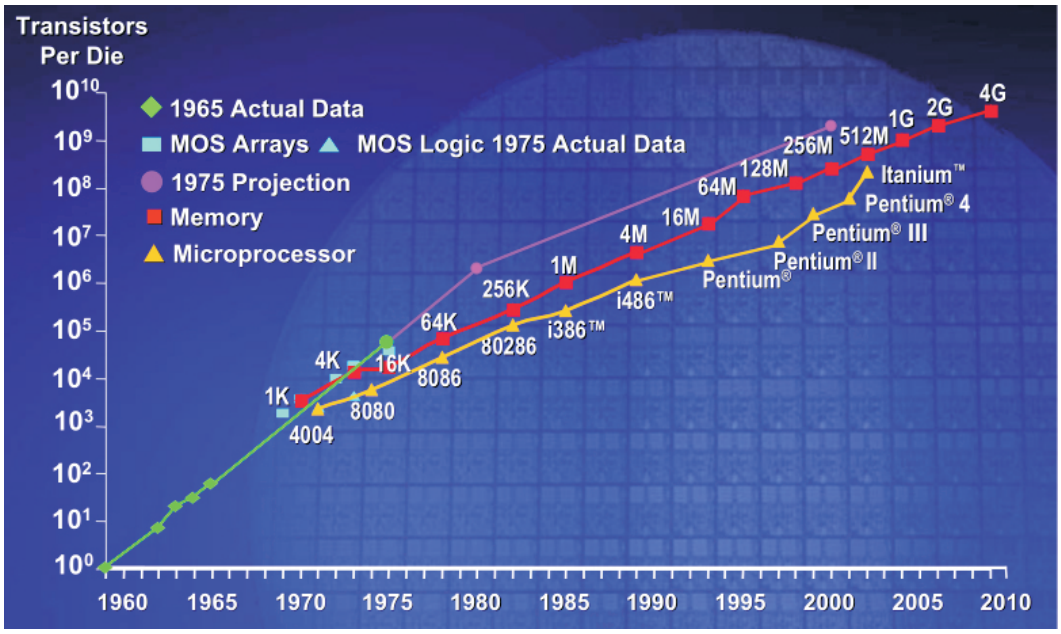

Figure 1.2.: Moores law and transistor counts between the years 1965 and 2010. From [Nex11].

applications in novel spintronic devices.
Chapter 2 starts with general description of the structural and physical properties of NiMnSb.
Chapter 3 explains two spintronic effects, namely the ***G**iant **M**agneto **R**esistance* (GMR) and the ***S**pin **T**orque **O**scillator* (STO).
The following chapter 4 describes the used experimental setups and their physical principles. It includes growth and characterization methods.
The growth of NiMnSb on (001) oriented substrates is the main subject of chapter 5. Here the growth process of NiMnSb is shown as well as additional preparations before the actual growth process of the half-Heulser alloy. It contains the processing of the InP substrate, the growth process of the (In,Ga)As buffer layer and all important parameters for the successful growth of NiMnSb(001).
In chapter 6 the growth process of NiMnSb on (111) oriented substrates is discussed. The difference between the two possible substrate orientations and the resulting growth process is illustrated. In this subsection, the growth of undoped and n-doped (In,Ga)As buffer layers and of NiMnSb is explained.
Chapter 7 gives an overview of the structural and magnetic properties of the grown layers. Used techniques are e.g. ***X**-**R**ay **D**iffraction* (XRD) and ***F**erro**m**agnet **R**esonance*(FMR).

In chapter 8 the possible 80K anomaly in NiMnSb is investigated. Measurements and results of our layers are presented.
Chapter 9 shows the results from NiMnSb based applications done by different groups with layers grown in this work. The produced devices are:

- a Giant Magneto Resistance device
- a Spin Torque Oscillator
- a Frequency Controlled Magnetic Vortex Memory

A look at future work and development is taken in the following section.
The conclusion is a summary of the complete work with all main results.
Generally all chemical elements and compounds used in this work are named with their short cut as used in the periodic table.
Crystal directions are written with [ ] and crystal planes with ( ). Negative directions are marked with an overbar e.g. $[\overline{111}]$ is the opposite direction to [111].

2. The half-metallic ferromagnet NiMnSb

2.1. Preface and crystal structure

On June 18th 1901, Dr. Fritz Heusler announced in the archive of the German Physical Society that he discovered some special behaviour with Mn and its alloys [Heu03]. The alloys showed magnetic behaviour even though, at this time, the single elements where known to be non-magnetic and Heusler could not explain this at that time. Only with the scientific development of quantum mechanics in the 1920s it was possible to understand this behaviour. This class of materials is now known as "Heusler alloys". Depending

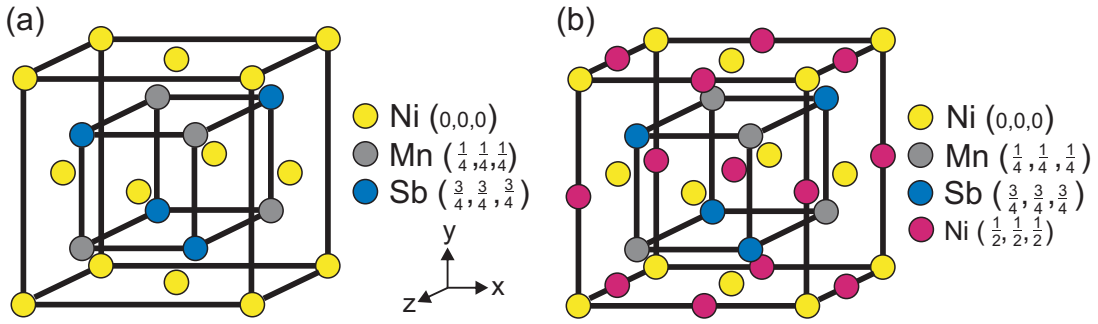

Figure 2.1.: (a) $C1_b$ crystal structure from *half*-Heusler $NiMnSb$. (b) $L2_1$ crystal structure from *full*-Heusler Ni_2MnSb.

on their crystal structure they can be divided into two classes: The *full*-Heusler alloys which crystallize in the $L2_1$ structure and the *half*-Heusler alloys with the $C1_b$ structure (Fig. 2.1). The space group of these crystal structures is $F\bar{4}3m$. Both crystals consist of four interpentrating fcc[1] lattices shifted by a fourth at the body diagonal. The difference between the two Heusler alloy crystal structures is the unoccupied position $(\frac{1}{2}, \frac{1}{2}, \frac{1}{2})$ in the $C1_b$ structure. As can be seen from Fig.2.1, both structures are similar to the zinc blende structure from widely used semiconductors, e.g. InP (Fig. 2.2). NiMnSb crystallizes in the $C1_b$ structure with a lattice constant $a_{NiMnSb} = 5.903$Å[Cas55]
The stacking sequence for NiMnSb consists of trilayers of Mn-Ni-Sb-□-Mn-Ni-Sb-□ along the [111] direction. InP consists of bilayers with a stacking sequence In-P-□-□-In-P-□-□ along the same direction.

[1] ***f**ace-**c**entered **c**ubic*

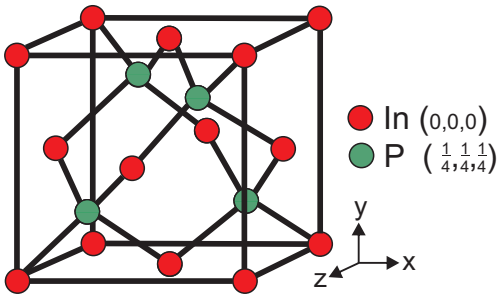

Figure 2.2.: Zincblende crystal structure from the III-V semiconductor InP.

2.2. Physical properties

When comparing the two crystal structures of the Heusler alloys, especially the point symmetry of the Mn sites, we can see that the inversion symmetry is broken. It changes from $O_h{}^2$ in the $L2_1$ type to $T_d{}^3$ in the $C1_b$ type (Fig.2.3). That circumstance has

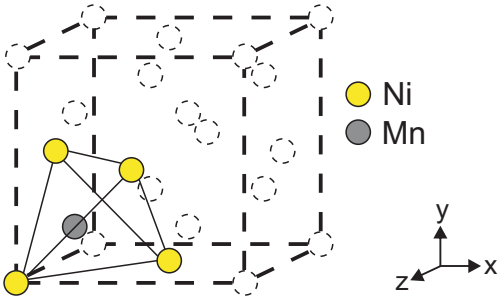

Figure 2.3.: T_d point symmetry in NiMnSb. For better illustration some atoms are only implied compared to Fig. 2.1a).

important consequences for the band structure of NiMnSb. In Fig.2.4 the band structure is presented calculated with the augmented-spherical-wave method of Williams, Kübler and Gelatt (WKB) done by de Groot *et al.* [Gro83]. For the majority-spin direction the band structure is similar to a metal with no band gap. On the other hand the band structure for the minority-spin direction behaves like a semiconductor with a band gap of $0.5eV$. The special feature from NiMnSb is that

Both band structures are in the same material at the same time !

As a consequence, NiMnSb shows 100% spin-polarization at the Fermi edge which makes it a perfect spin injector.
In half-metallic ferromagnets, three elements play an important role:

- the crystal structure

[2] octahedron horizontal
[3] tetrahedron diagonal

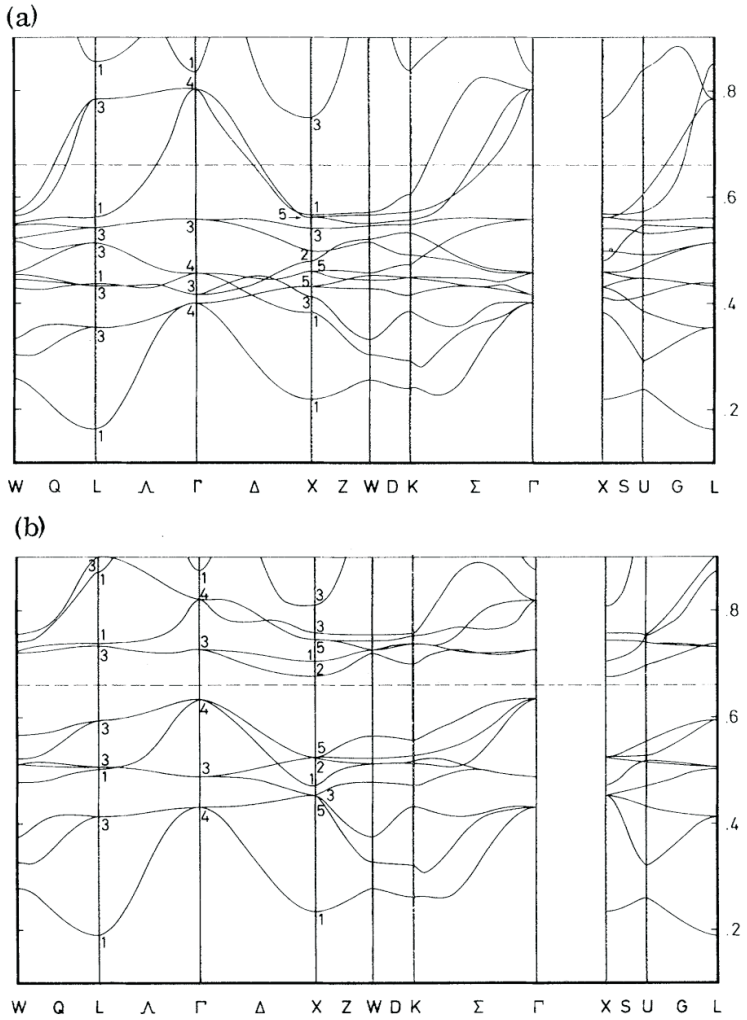

Figure 2.4.: Band structure of NiMnSb for: a) the majority-spin direction and (b) the minority-spin direction (b). A band at low energies (< 0.2 Ry) of mainly Sb-s character has been omitted. From [Gro83].

- the valence-electron count and covalent bonding
- the large exchange splitting of the Mn 3d-electron band states

The consequence of the broken symmetry from O_h to T_d is not only breaking the time-reversal symmetry, but also the conjugation symmetry which causes that the distinction between the t_{2g} d and p character of the electrons is lost and the bindings, e.g. between the Sb p electrons and the Mn t_{2g} electrons, are now different compared to the *full*-Heusler alloys. As a result, NiMnSb has the band structure shown in Fig. 2.4. Castelliz [Cas55] and later Kabani, Roshko and Moodera [Kab90] determined the magnetization per unit cell as 4.0 μ_B for NiMnSb. Castelliz also investigated the Curie temperature. His result was a surprising value for T_C of $\approx$ 730K, which is well above room temperature.

2.3. 80K anomaly

In 1988 M.J. Otto *et al.* also investigated the structure and magnetic properties of NiMnSb and related inter-metallic compounds [Ott01]. Additionally they investigated the transport properties of NiMnSb [Ott02]. In their measurements they presented the electrical resistivity and the Hall effect of NiMnSb and discussed the results in terms of a simple phenomenological theory.

The observed resistivity ρ as a function of the temperature shows the behaviour characteristic for magnetic metals [Fig.2.5]. The resistivity of ferromagnetic metals at low temperature usually has a term proportional to T^2, ascribed to one-magnon scattering of conduction electrons (spin-flip scattering). In their resistivity data for NiMnSb Otto *et al.* have seen little or no evidence for such a T^2 contribution and concluded that in half-metallic ferromagnet at low temperature all states at the Fermi level are spin-polarised and spin-flip scattering is not possible and thus for half-metallic ferromagnet one expects the absence of a T^2 term in the resistivity.

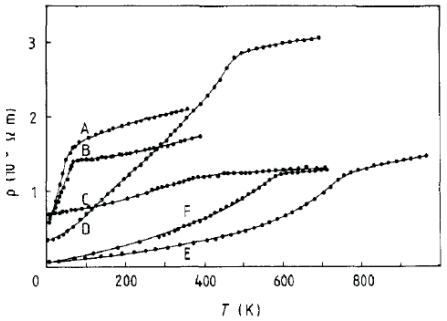

Figure 2.5.: Electrical resistivity ρ as a function of temperature for different magnetic materials from [Ott02]. A: CuMnSb, B: AuMnSb, C: PtMnSn, D: CoMnSb, E: NiMnSb, F: PtMnSb.

The ordinary Hall effect in semiconductors and metals is caused by the Lorentz force on the charge carriers and is proportional to the applied magnetic field. In a ferromagnet there is an additional contribution in the Hall effect, the so-called anomalous Hall effect (AHE). The AHE is proportional to the magnetisation (Hurd 1972). For NiMnSb we can write the total Hall resistivity as:

$$\rho_{xy} = \frac{E_y}{j_x} = R_0 B_z + R_s \mu_0 M_z \qquad (2.1)$$

with j_x being the longitudinal current and E_y being the transverse electric field appearing for j_x. R_0 is the ordinary Hall coefficient, R_s is the anomalous Hall coefficient, μ_0 is the magnetic field constant[4] and M_z the spontaneous magnetization. In Fig.2.6 and Fig.2.7 the ordinary Hall coefficient and the anomalous Hall coefficient is shown. The observation of a positive ordinary Hall effect in NiMnSb is in agreement with band-structure calculations and show that electrical conduction is due to holes in a partly occupied Sb 5p band.

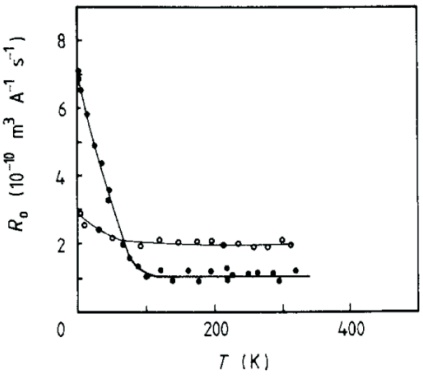

Figure 2.6.: Ordinary Hall coefficient R_0 as a function of temperature for NiMnSb (•) and PtMnSb (○). From [Ott02].

Otto *et al.* explained the behaviour of the anomalous Hall coefficient with two main

[4] $\mu_0 = 1.2566 \cdot 10^{-6} \frac{H}{m}$, from [Kit01]

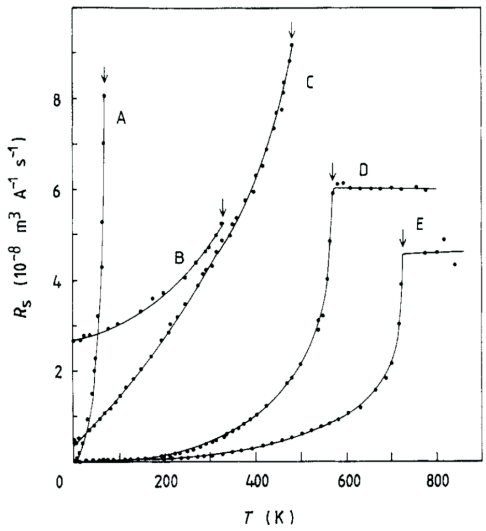

Figure 2.7.: Anomalous Hall coefficient R_S as a function of temperature from [Ott02]. An arrow indicates the Curie temperature. A: AuMnSb, B: PtMnSb, C: CoMnSb, D: PtMnSb, E: NiMnSb.

contributions. They found that side-jump contribution dominates over the contribution of skew scattering. With the assumption of a proportionality between the spin-polarization of the charge carriers and the total magnetisation, they were able to separate the two contributions. As a result of their assumption and phenomenological theory they concluded that this proportionality is an important fact like the electronic structure of NiMnSb changes with increasing temperature.
J.S. Moodera and D.M. Mootoo also did transport studies on NiMnSb [Moo94]. For NiMnSb the resistivity decreased with temperature, as Otto *et al.* already have seen in their measurement data. But in a more detailed way Moodera *et al.* saw a more rapid decrease of ρ below about 100K (Fig.2.8) and a linear dependence of ρ vs T. As mentioned before, if there are no spin-down states at E_F, then spin-flip scattering for spin-up charge carriers due to magnons is forbidden. From that assumption follows an absence of T^2 dependence of ρ and an increase in the mobility of the charge carriers. Due to the high Curie temperature from NiMnSb (730K), no one expects many magnons at low temperature, meaning that the absence of T^2 dependence of ρ does not necessarily proof the absence of spin-down states at E_F. The ordinary Hall coefficient rises in the temperature range from 0K-80K. This behaviour points to significant changes in the carrier concentration and mobility. The mobility has to increase considerably to explain the visible drop in the measured resistivity in this temperature range. They concluded that their interpretation appeared to be consistent with a gap for minority spin carriers at E_F.

Another group focused again on the resistivity and the magnetization of NiMnSb [Hor96]. They observed a crossover in the temperature dependence of magnetization and resistivity near 70K. The magnetization varies as $T^{\frac{3}{2}}$ under and as T^2 over 70K [Fig.2.9]. This means that they have two different magnets, a Heisenberg ferromagnet

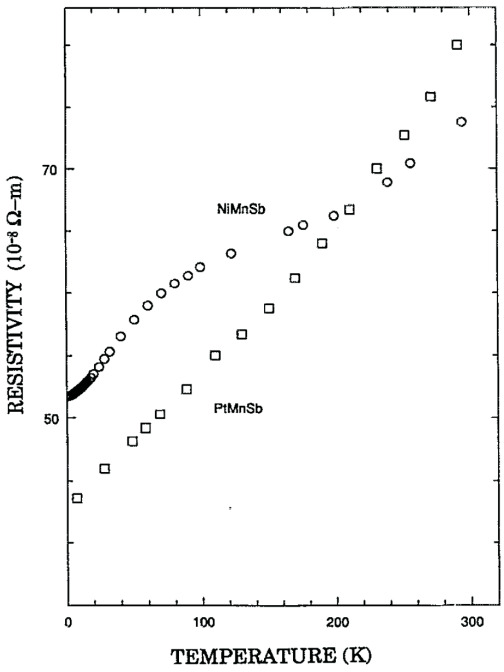

Figure 2.8.: Temperature dependence of the resistivity for NiMnSb and PtMnSb compound thin films. For NiMnSb a rapid drop in resistivity below 100K is visible. Measurements from [Moo94].

where the classical spin wave law is valid ($T^{\frac{3}{2}}$) and an itinerant magnet above 70K (T^2).

In resistivity, the behaviour follows T^2 under 50K and increases rapidly around 70K and flattens above. A suggestion is that some type of excitations become possible near that temperature. Above 100K the resistivity follows the power law with $n \approx 1.35$. The increase of resistivity and change in magnetization and maybe also the increase in the Hall coefficient could be explained by the opening of a new scattering channel near 80K. This opening is responsible for the rapid decrease of the expected spin-down population below 80K. No spin-flip scattering will occur for spin-up electrons, which should increase their mean free path and mobility and also the amplitude of the ordinary Hall coefficient. C. Hordequin *et al.* [Hor00] re-examined NiMnSb in a more detailed way. Their results are shown in Fig.2.10. Near 80K a change in the resistivity behaviour was observed. Contrary to Moodera and Mootoo (Fig.2.8), Hordequin *et al.* see a nearly quadratic behaviour of ρ below 50K. Below 50K ρ follows:

$$\rho = \rho_0 + BT^\alpha \text{ for } 1.7 < \alpha < 2.2 \tag{2.2}$$

and above:

$$\rho = A_2 + B_2 T^{\alpha_2} \text{ for } 1.3 < \alpha_2 < 1.5 \tag{2.3}$$

The development of the ordinary Hall coefficient R_H ($= R_0$) varies precisely as in the measurements done by Otto *et al.*. The positive sign of R_H indicates a dominant hole character. The anomalous Hall term increases in the temperature range between 80K-300K, also in line with the observations of Otto *et al.*. But they recognized an additional

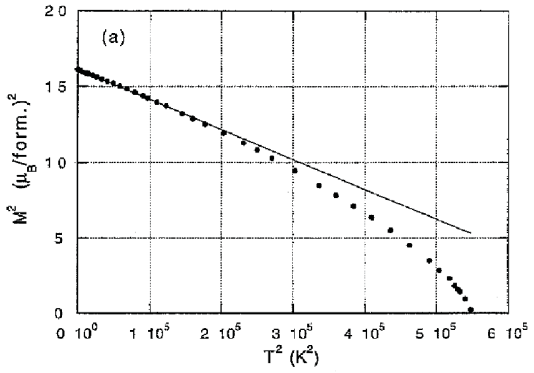

Figure 2.9.: Square of the magnetization per formula unit versus square of temperature of a polycrystalline sample up to the Curie point. From [Hor96].

upturn in the range between 0K-80K. Hordequin *et al.* say that the behaviour in R_H and $\mu_0 R_H M_S$ between 80K and 0K should be attributed to a change in the electronic structure and/or to an increase in the mobility of carriers. With all their observations

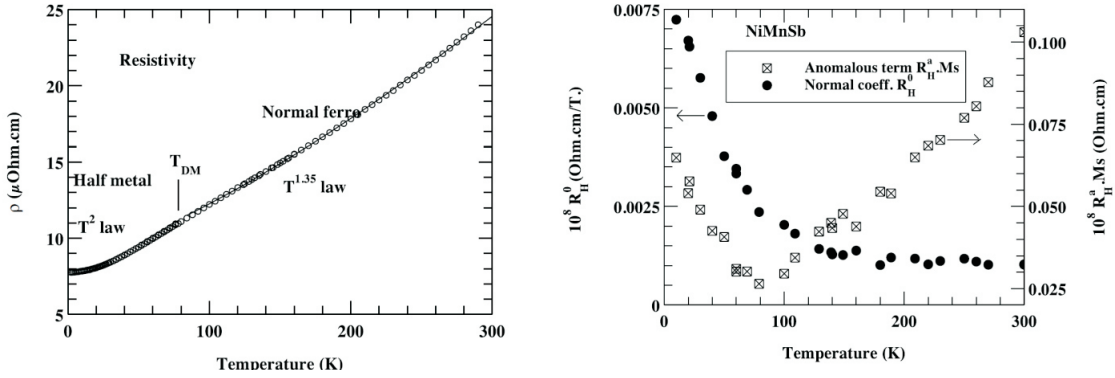

Figure 2.10.: *Left:* Resistivity over temperature for polycrystal NiMnSb. *Right:* Anomalous Hall term ⊠ and normal Hall coefficient • for polycrystal NiMnSb. From [Hor00].

and measurements, they concluded that at 80K a cross-over from a half-metal to a normal ferromagnet in NiMnSb occurs. The proof or disproof of this statement is the topic of chapter 8, describing the process of the necessary sample structure and the cryostat measurements with our NiMnSb sample.

3. Spintronic effects

3.1. Giant Magneto Resistance (GMR)

The GMR effect was discovered in 1986 by Peter Grünberg[1][Gru86] and simultaneously by Albert Fert[2][Bai88]. In their experiments they investigated multilayers of ferromagnet/non-magnet (Fe/Cr). It has been shown that at Cr layer thickness of 1nm the magnetization of the Fe layers are aligned antiparallel.

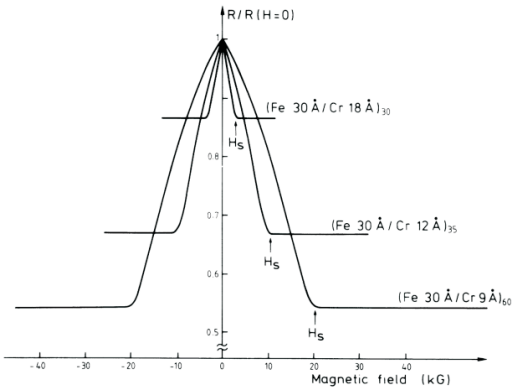

Figure 3.1.: GMR effect at 4.2K of a Fe/Cr superlattice with different thick Fe and Cr layers. From [Bai88].

When applying a magnetic field to such a stack, it is possible to change the direction of the magnetic layers parallel or antiparallel. This behaviour can be influenced by different thicknesses of the non-magnetic layers. When measuring the electrical resistance of such a Fr/Cr superlattice stack while sweeping an external magnetic field, the graph in Fig.3.1 is detected [Bai88]. In the parallel case the resistance is low and high for the antiparallel case of the magnetic layers. We can discern three geometries of the GMR effect, namely the configurations ***c**urrent **i**n **p**lane* (CIP), ***c**urrent **p**erpendicular to **p**lane* (CPP) and the so-called *spin valve*. The orientation of the layers and the direction of the applied current is diagrammed in Fig.3.3. Fig.3.1 is a typical measurement of GMR in cpp configuration. An important parameter for the efficiency for a GMR device is spin-polarization. The spin-polarization P_N is defined as:

$$P_N = \frac{D\uparrow(E_F) - D\downarrow(E_F)}{D\uparrow(E_F) - D\downarrow(E_F)} \tag{3.1}$$

with $D\uparrow$ density of states of the spin up electrons at the Fermi level and $D\downarrow$ density of states of the spin-down electrons at the Fermi level. The reason for a GMR effect is the spin-dependent scattering at the ferromagnet/non-magnet interface. As a result, we have different resistance values for both spin directions. The magnitude of the GMR effect is defined as:

$$GMR = \frac{R_{AP} - R_P}{R_P} \tag{3.2}$$

with R_{AP} being the resistance of the stack with the magnetizations oriented antiparallel and R_P being the resistance for the parallel orientation of the magnetizations. Following

[1]* 18. May 1939, Pilsen, Nobel prize 2007

[2]* March 7th 1939, Carcarssonne, Nobel prize 2007

the properties of NiMnSb described in chapter 2, the half-Heusler alloy NiMnSb should be a good choice for a GMR device due to its theoretical 100% spin-polarization and its high Curie temperature.
When using *Magneto-Optical Kerr-Effect*(MOKE) as the measuring technique, data like in Fig.3.2 is measured (from [Zin90]). The measured stack consists of Co/Au/Co layers with different coercive fields in the two Co films. The different coercive fields are achieved by different thicknesses of the Co films. The measurements occur at 10K and at room temperature. Starting with no external magnetic field up to 300mT, the first magnetic layer switches (symbolized by red arrow) and the resistance is high due to the antiparallel configuration of the two magnetic layers.
At a certain point the magnetic force is too strong and the second magnetic layer also switches (symbolized by blue arrow). Sweeping backwards from 300mT to 0mT to -300mT, the resistance remains small till a small negative magnetic field and the first magnetic layer (red arrow) switches again and the antiparallel configuration is restored, resulting in a high resistance. At higher negative fields the second layer also switches again and the parallel case of the magnetizations is present again. With the behaviour of magnetic/non-magnetic layer stacks in an external field it is possible to use the GMR effect for read heads of computer hard drives or as a memory device. The different resistance states can be used as a binary system of 0 (low resistance) and 1 (high resistance). In chapter 9.1 we present the results on our built GMR device. One disadvantage of GMR devices is the necessary external field. A new approach for novel spintronic devices uses the ***S**pin **T**ransfer **T**orque* (STT) mechanism [Ral02]. An useful device is the STO. The STO functionality and the necessary physical principles are the topic of the following section.

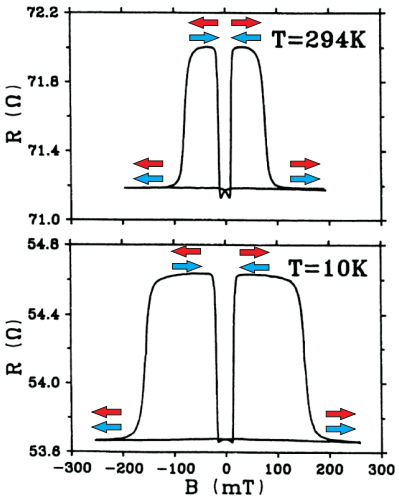

Figure 3.2.: Resistance of a Co/Au/Co stack measured at 10K and at 294K. From [Bar48].

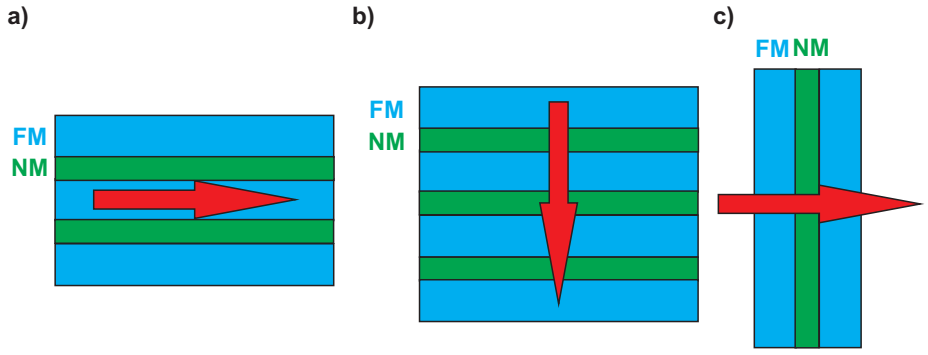

Figure 3.3.: Different current directions (red arrow) through a magnet/non-magnet/magnet stack. a) cip, b) cpp and c) spin-valve.

3.2. Spin Torque Oscillator (STO)

A spin-polarized current bears a torque which can interact with the magnetization of a magnetic layer and generates a precession of the magnetization [Slo96],[Ber96]. As a consequence the resistance of such a device oscillates. This can be detected either through GMR or ***T****unneling* ***M****agneto* ***R****esistance* (TMR) effect. The so-called spin transfer torque can activate a GHz oscillation in the magnetization direction of the magnetic film. A device using that function is called a STO. To understand this behaviour we use a spin-polarized current injected into a magnetic material. As already explained in connection with the GMR effect, the electrical resistance depends on the direction of the magnetization of the magnetic films. If the direction of both is antiparallel, the spin-polarized current bears a torque on the magnetic layer. Let us assume that the spin-polarization points right and the magnetization of the magnetic material points up. Then at the interface between the non-magnetic layer NM (spin injector) and the magnetic material FM, the magnetization is rotated a little bit clockwise till at a certain point the magnetization points back up (Fig.3.4). This absorption of the current causes

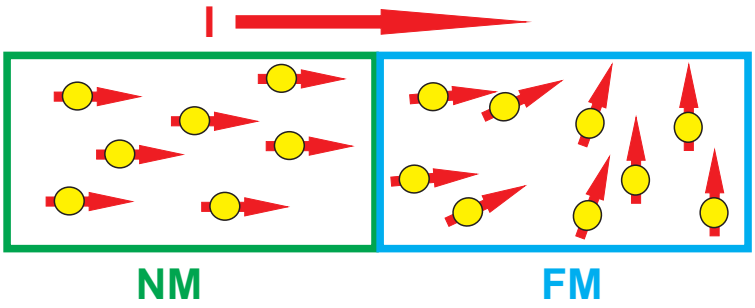

Figure 3.4.: Behaviour of a spin-polarized current on a magnetic film. This functional principle is called the spin transfer torque. Graphic in imitation of [Tun05].

a torque on the magnetic film and tries to rotate it clockwise. If the current is highly spin-polarized and strong enough, it can switches the magnetization direction completely and then we can use such a device as a magnetic memory with two states represented through the two magnetization directions, known in a binary system as 0 and 1. The torque on the magnetization caused by the current can be described as:

$$\Gamma_{ST} = -\gamma a M \times (M_P \times M) - \gamma b (M \times M_P) \tag{3.3}$$

The first term is the spin torque term and the second one the effective field term. The spin torque term can behave like a damping or anti-damping term. This depends on the current direction. This means that a spin torque can generate e.g. a steadily magnetic precession. This is possible because the magnetization steadily pumps energy into the polarized current to compensate the energy loss caused by Gilbert damping [Gil55],[Tse02]. The resulting frequency in this situation is in the GHz range and depends on the applied current density and degree of polarization . In our device the spin torque

drives a continuing precession of the magnetization resulting in GHz frequencies.
This device now is called the STO. The advantage of a STO compared to a conventional LC circuit is the size of only a few hundred nm^2, the higher Q-factor and the tunability. When building a STO it is desirable to use a material with a low magnetic damping where the magnetization can be engineered with less energy. To show that NiMnSb is a good candidate for a STO device, FMR measurements are shown in chapter 7.2.1. The measurements and results of our STO are the topic of chapter 9.2.

4. Experimental setups and their physical principles

With the technique of ***M**olecular **B**eam **E**pitaxy* (MBE) you have a tool for a controlled transfer of atoms from effusion sources to a substrate. This means that it is possible to grow layers in atomic dimensions and thus to produce smooth surfaces. An important advantage of MBE against other vacuum deposition techniques is the very precise control of the beam fluxes and growth conditions. This assumes that an ultrahigh vacuum is present in a MBE system and this gives MBE another additional unique advantage over other thin film deposition techniques. This advantage is the possibility to use the in-situ surface sensitive control method ***R**eflection **H**igh **E**nergy **E**lectron **D**iffraction* (RHEED)(see section 4.3.3).
The principle of MBE and different analysis techniques for epitaxial thin films are the topic of the following chapter.

4.1. Molecular beam epitaxy

In this work the technique of MBE is used for the preparation of the investigated layers. This chapter gives an overview of the technique and the physical principle behind epitaxial growth. First of all the growth process in MBE occurs under ultrahigh vacuum conditions. In general, if pressures are under a value of $p \leq 1.33 \cdot 10^{-9} Torr$, then the vacuum is called ***u**ltra**h**igh **v**acuum* (UHV). To reach such small pressures a system of different pumps and pumping mechanism is needed.
A MBE system consists of different essential elements. Fig.4.2a gives an overview of such a system. It is divided into three zones, namely:

- I) molecular beam generation zone
- II) vapor elements mixing zone
- III) substrate crystallization zone

In zone I the molecular beams are generated in Knudsen effusion cells under UHV condition. This means that we are allowed to treat such an effusion cell as a point source because the diameter of the orifice of a Knudsen cell is small compared to the distance between effusion cell and substrate. In Fig.4.1 on the left side a sketch of a Knudsen cell is shown. The crucible with the element is wrapped by a heat foil and a foil tube. To control the temperature of the effusion cell a thermocouple is connected

to it. Additional water cooling is installed for safety reasons. On the right side our used Mn-effusion cell from the NiMnSb chamber is shown. The effusion cells are only controlled by thermocouples and ***p**roportional-**i**ntegral-**d**erivative* (PID) controllers. The generated beams can be turned on or off by opening or closing the effusion cell shutters (see Fig.4.2). The beam from one effusion cell starts to mix with all beams from the other effusion cells at a certain distance from the substrate. The exact point depends both on geometry parameters of the growth chamber and the amount of effusion cells with open shutters at the same time. This place is zone II before the growth process occurs in zone III . In the growth process a series of important surface processes are

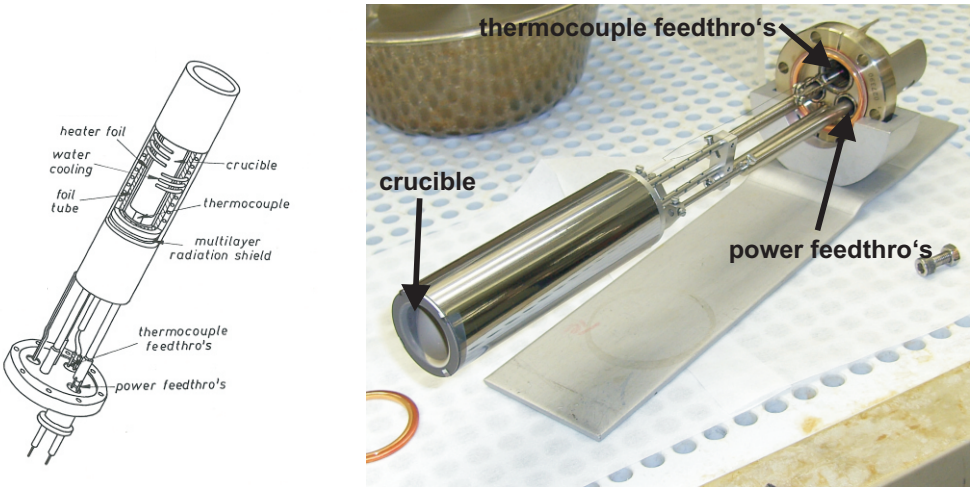

Figure 4.1.: *Left:* Sketch of a Knudsen cell with all important parts (from [Her89]. *Right:* Mn Knudsen cell used in our NiMnSb MBE chamber.

involved:

- adsorption of the constituent atoms or molecules impinging on the substrate surface
- surface migration and dissociation of the absorbed molecules
- incorporation of the constituent atoms into the crystal lattice of the substrate or in the already grown epilayer
- thermal desorption of the species not incorporated into the crystal lattice

In Fig.4.3 the different surface processes are illustrated. These processes depend on the properties of the crystal where the impinging molecules or atoms interact. The adsorption process is divided into physical adsorption and chemisorption. The two adsorption mechanisms vary in the way they bind. In physical adsorption there is no electron transfer and the forces are van der Waals type. Chemisorption on the other hand uses an electron transfer e.g. chemical reaction and the forces are then of the type occurring in the appropriate chemical bond.
Chemisorption has higher adsorption energies than physical adsorption.

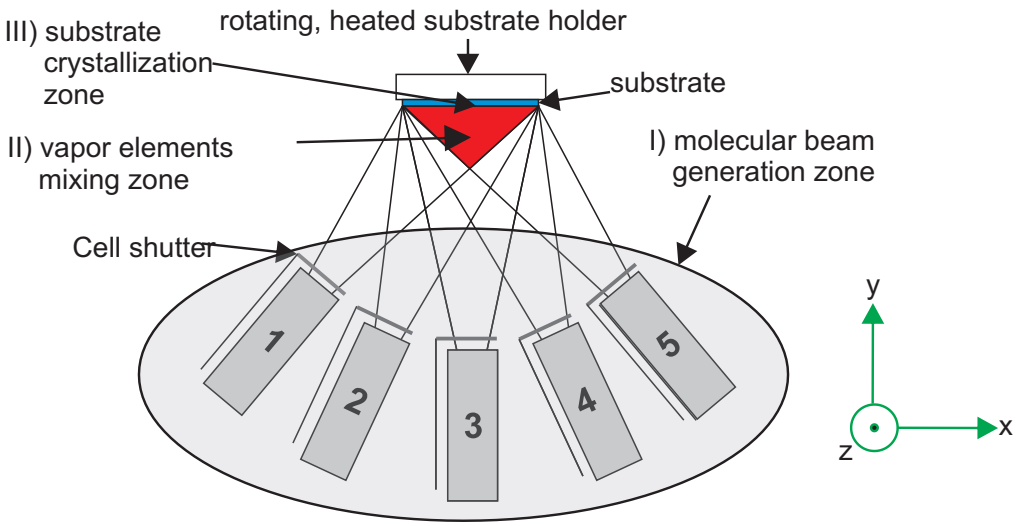

Figure 4.2.: Essential parts of a MBE system. The three zone I), II) and III) are marked light grey, blue and red.

In general, the growth process is an accumulation of many no-equilibrium process. The theoretical description is difficult and exceeds the complexity of this work. A detailed description of all process can be found in [Her89]. We just want to retain two main parameters of crystal growth, the substrate temperature and the single temperature of the effusion cells.

Three crystal growth modes are accepted in MBE (Fig.4.4). In the *Volmer-Weber* or *island* mode Fig.4.4 a) small islands are generated at the surface caused by the directly nucleated clusters at the surfaces. This is the result if the bonding between the incoming atoms or molecules is stronger than to the substrate. The clusters then act as centres for the impinging atoms and an island is generated.

The *Frank-van der Merve* or *layer-by-layer* mode (Fig.4.4 b)) shows flat surfaces. The crystal grows monolayer by monolayer because the atoms are bonded more to the substrate/surface than to each other.

Also there is a mixing of both already mentioned growth modes. It is called the *Stranski-Krastanov* or *layer plus island* mode Fig.4.4 c). First *layer-by-layer* is formed, but after a few monolayers this growth mode is unfavourable and islands are formed on the last layer. This growth mode can happen if the monotonic decrease in binding energy characteristics by the *Frank-van der Merve* mode is disturbed.

To meet our demands for the layers, the *Frank-van der Merve* mode is the preferred growth mode for our heterostructures.

Due to the different materials needed for our samples, we have access to a cluster of different MBE chambers. An overview is given in Fig.4.5. With this setup it is possible to grow a buffer layer in chamber GaAs I and then transfer the sample without breaking the UHV into the Heusler chamber. In addition, the different layers don't have to necessarily be from the same group of the periodic table. That means that we are able to grow a II-IV semiconductor on a III-V semiconductor and vice versa. In this work the

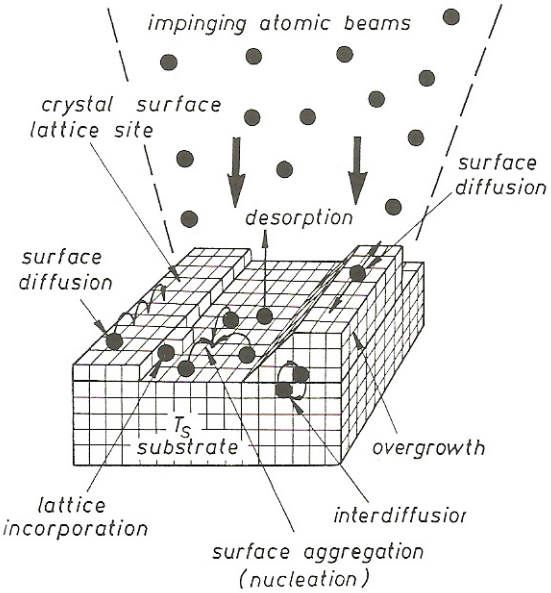

Figure 4.3.: Surface processes occuring during film growth. From [Her89].

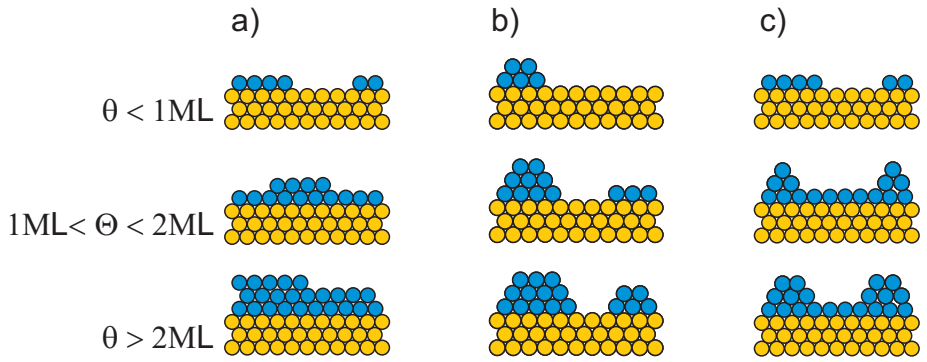

Figure 4.4.: Illustration of main growth processes a) *Frank-van der Merve*, b) *Volmer-Weber*, c) *Stranski-Krastanov*.

chamber GaAs I chamber and Heusler chamber are used plus the in-situ metallisation. In Fig.4.6 both MBE chambers' geometries are illustrated. The main difference between the chambers is the configuration of the effusion cells. In chamber Fig.4.6 a) the fluxes hit the substrate horizontally. Different in Fig.4.6 b), where the fluxes hit the substrate vertically. The GaAs I chamber is build like Fig.4.6 a) with 8 effusion cells respectively 4 cells on a circle around the substrate. Fig.4.6 b) is the setup configuration of the NiMnSb chamber where all cells are in one circle. That concludes that the fluxes hit the substrate at different angles in both chambers which changes the size of the vapor elements mixing zone (see Fig.4.2 II). Another point is the pump system used in every chamber. The NiMnSb chamber is only pumped by a cryo pump and a liquid H_2O shroud. In the GaAs I chamber a cryo pump, ion getter pump and a liquid N_2 shroud

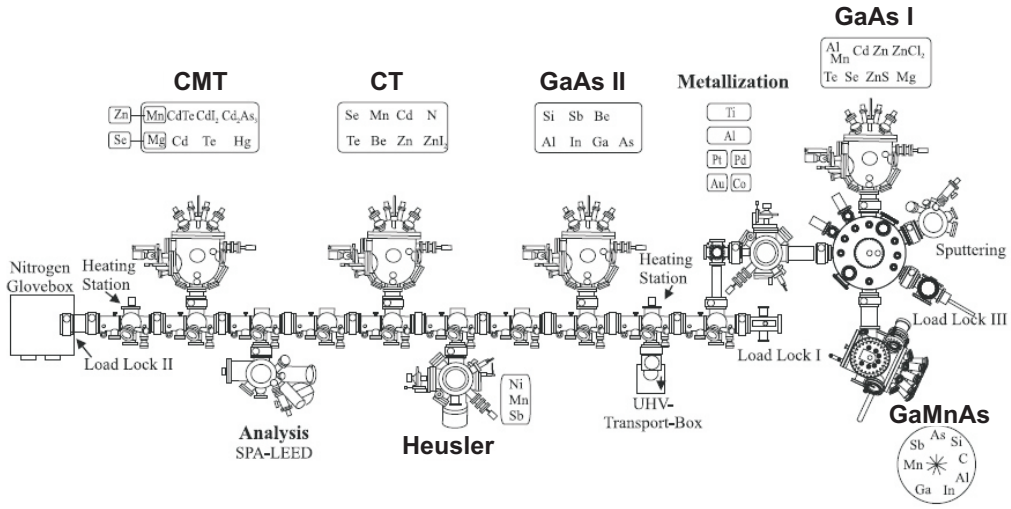

Figure 4.5.: MBE Cluster at the chair of physics *Experimentelle Physik* 3 at university of Würzburg.

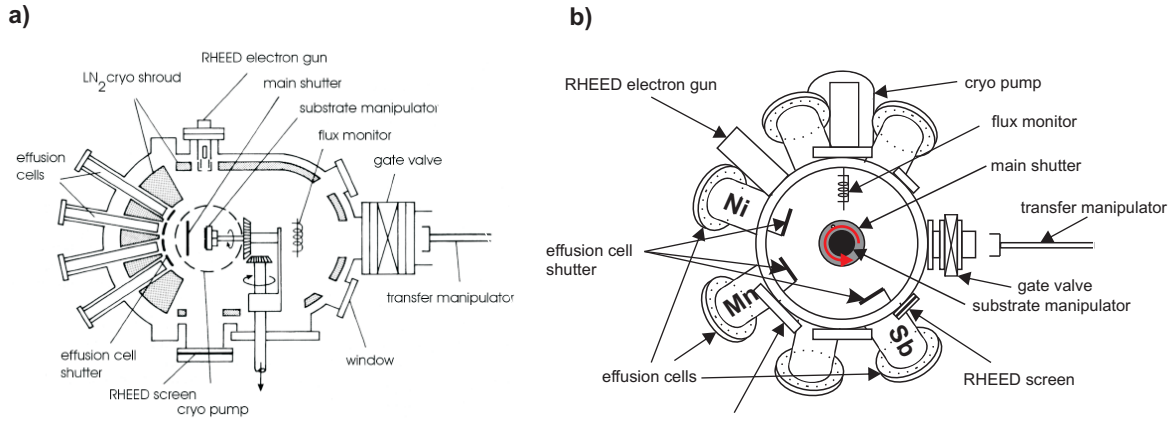

Figure 4.6.: Plane view of a) Riber 2300 chamber and b) 2" UHV chamber from mbe-komponenten GmbH.

is used for pumping to reach UHV conditions.
As mentioned earlier a lot of different material systems can be grown and combined in such a cluster system. Typically all wafers brought into the UHV systems will be degased in one of the two heating stations and afterwards transferred to the predetermined chamber.
The detailed description of the growth processes for the buffer layer and the half-metallic ferromagnet layer are explained in chapter 5 and chapter 6. Next the principle of different techniques for characterizing thin films will be discussed.

4.2. Reciprocal space

For many problems in solid state physics the real crystal lattice is not the best choice when trying to find a solution. A better choice is the so-called reciprocal lattice. The conversion from real space with the basis vectors $\vec{a_1}, \vec{a_2}, \vec{a_3}$ to reciprocal space with the basis vectors $\vec{b_1}, \vec{b_2}, \vec{b_3}$ is defined as:

$$\vec{b_1} = \frac{2\pi}{V}(\vec{a_2} \times \vec{a_3}) \qquad \vec{b_2} = \frac{2\pi}{V}(\vec{a_3} \times \vec{a_1}) \qquad \vec{b_3} = \frac{2\pi}{V}(\vec{a_1} \times \vec{a_2}) \tag{4.1}$$

Every reciprocal basis vector is perpendicular on two basic vectors from real space. This means that

$$\vec{b_i} \cdot \vec{a_j} = 2\pi\delta_{ij} \quad \text{with} \quad i, j = 1, 2, 3 \tag{4.2}$$

δ_{ij}=1 if i=j and δ_{ij}=0 if i≠j. Every point in the reciprocal space can be described through vectors:

$$\vec{G} = v_1\vec{b_1} + v_2\vec{b_2} + v_3\vec{b_3} \quad \text{with} \quad v_1, v_2, v_3 \quad \text{are integers} \tag{4.3}$$

Such a vector $\vec{G}$ is a **reciprocal lattice vector**. The electron density $n(\vec{r})$ in three dimensions is given by

$$n(\vec{r}) = \sum_{\vec{G}} n_{\vec{G}} e^{(i\vec{G}\cdot\vec{r})} \tag{4.4}$$

The derivation from Eq.(4.4) can be found in many solid state physics books e.g. [Kit01]. The vectors $\vec{G}$ in this Fourier row are accurately the reciprocal lattice vectors from Eq.(4.3). With them the Fourier development of the electron density fulfill the invariance to the crystal translation $\vec{T} = u_1\vec{a_1}+u_2\vec{a_2}+u_3\vec{a_3}$. With this assumptions Eq.(4.4) becomes

$$n(\vec{r}+\vec{T}) = \sum_{\vec{G}} n_{\vec{G}} e^{(i\vec{G}\cdot\vec{r})} e^{(i\vec{G}\cdot\vec{T})} \tag{4.5}$$

In this equation $e^{(i\vec{G}\cdot\vec{T})} = 1$ because

$$e^{(i\vec{G}\cdot\vec{T})} = e^{[i(v_1\vec{b_1}+v_2\vec{b_2}+v_3\vec{b_3})\cdot(u_1\vec{a_1}+u_2\vec{a_2}+u_3\vec{a_3})]} = e^{[i2\pi(v_1u_1+v_2u_2+v_3u_3)]} \tag{4.6}$$

These results shows us that Eq.(4.4) is only valid for vectors $\vec{G}$ (Eq.(4.3)).

4.3. Structural analysis

All grown samples were investigated by different analysis methods to determine the quality of the layers. The following section concentrates on two techniques to check the quality: in-situ with RHEED and ex-situ with ***H**igh **R**esoultion **X**-**R**ay **D**iffraction*(HRXRD).

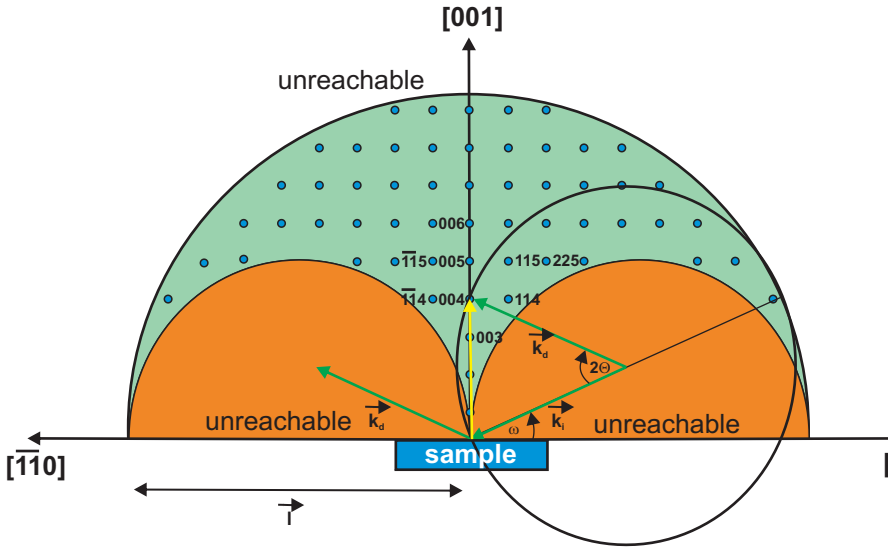

Figure 4.7.: Ewald construction in reciprocal space. The Ewald construction is valid for electron and x-ray diffraction.

4.3.1. High resolution x-ray diffraction

As mentioned in the section before, RHEED is an in-situ technique to observe crystal growth and the quality of the grown layers, but only with RHEED you don't have access to important parameters like the lattice constant, lattice-match or mismatch to the substrate or the interface quality of the layers. The rays discovered by Conrad Wilhelm Röntgen[1] and the technique of HRXRD are a very good tool for determining these parameters. Fig.4.8 represents the basic situation if a monochromatic x-ray beam hits a perfect crystal structure.
The incident angle Θ is the so-called *Bragg angle* Θ_B . The distance between two parallel planes of the crystal is marked as *d*. *d* is smaller than the lattice constant *a*. That is obvious when looking at the shown InP crystal. Keep in mind that a plane does not reflex the whole incident beam. If that would be the case only the first plane could be examined. Just 10^{-8} of the intensity is reflected. To receive constructive interference the path lengths of two or many beams are only allowed to differ by either zero or a whole number of wavelength λ. In most cases the Cu $K_{\alpha 1}$ wavelength is used. The value is 1.54092Å. The difference in path lengths between ray 1 and 2 is the red line in Fig.4.8. It can be calculated with basic geometry inside the rectangular triangle by

$$sin\Theta = \frac{\delta}{d} \Rightarrow \delta = d \cdot sin\Theta \tag{4.7}$$

This resulting value has to be doubled to get the complete path length difference. To get constructive interference, the difference has to be either zero or a whole of λ. This

[1]* March 27, 1845 †February 10, 1923. W.C. Röntgen discovered on November 8, 1895 the x-rays at the university of Würzburg

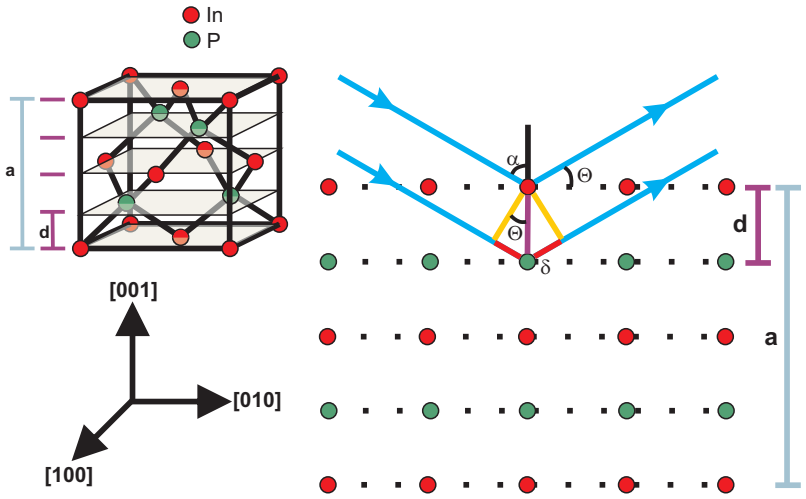

Figure 4.8.: Diagram for derivation of *Bragg's law*.

leads to

$$2d \cdot sin\Theta = n \cdot \lambda \tag{4.8}$$

with

$$d = \frac{a}{\sqrt{h^2 + k^2 + l^2}} \tag{4.9}$$

where n is an integer and h,k,l are the Miller indices. Eq.(4.8) is known as *Bragg's law*. This derivation satisfies the x-ray diffraction under ideal conditions, namely a perfect and infinite crystal and a perfect parallel monochromatic x-ray beam. If measuring a sample consisting of different material systems with different lattice constants we would expect to receive three sharp lines when plotting intensity over angle. One for every material system. Under non-ideal conditions these assumptions are not true any more, especially the grown crystal is not perfect and finite. This leads to a broadening of the expected peaks. If we assume that the path difference between the scattered rays of the first two planes differs slightly from an integer number of used wavelength λ, then the plane for destructive interference of the scattered ray from the first plane lies deep in the crystal. In a finite, thin layer this plane might not exist and accordingly a complete cancellation of all scattered rays will not result. To explain this behaviour we modify the graphic from Fig.4.8. We consider that the rays A and B in Fig.4.9 deviate by a small angle ε from the Bragg angle Θ_B. We see that ray A has an incident angle $(\Theta_B + \varepsilon)$ with the result that ray C' from the mth plane, below the scattering plane from ray A, is $(m{+}1)$ wavelength out of phase with A'. Accordingly a plane in the middle between the plane from ray A and the plane from ray D scatters with a phase shift of $(m{+}\frac{1}{2})$ wavelengths. This means that all rays scattered by the first half of the crystal planes annul those scattered by the second half of the crystal planes and the intensity of the diffracted beam at $(2\Theta_B + \varepsilon)$ is zero. The same applies to the rays B' and D' with the angle $(\Theta_B - \varepsilon)$. But between the angle range $(\Theta_B + \varepsilon)$ to $(\Theta_B - \varepsilon)$, the diffracted beam intensity is unequal to zero with a maximum at $2\Theta_B$. The measured intensity distribution is shown in Fig.4.10. It can be described with a relation between line width

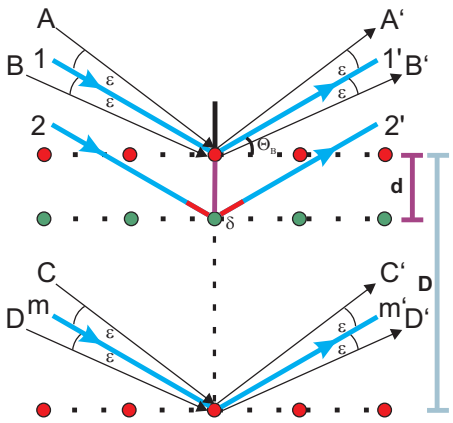

Figure 4.9.: Reason for peak broadning.

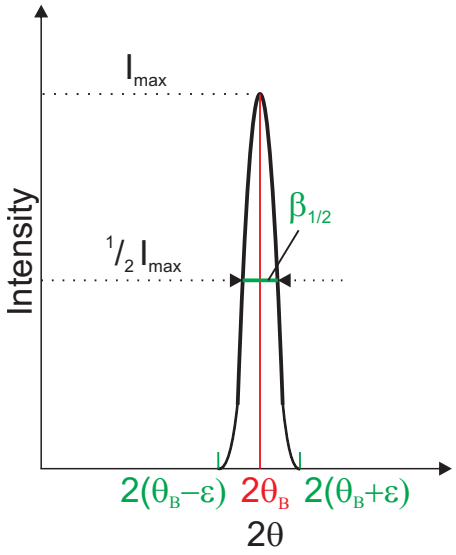

Figure 4.10.: Peak broadning effect caused by layer thickness, expressed by the Scherrer formula.

and crystal size and is known as the Scherrer formula [Pal69]:

$$\beta_{1/2} = \frac{0.9\lambda}{D \cdot cos\Theta_B} \tag{4.10}$$

The next important point is the possibility to have access to the material composition of grown layers. For ternary semiconductors, in our case (In,Ga)As, the material composition can be calculated from the relaxed binary alloys lattice constants a_1, a_2 with Vergard's law [Veg21]:

$$x = \frac{a_x - a_1}{a_2 - a_1} \tag{4.11}$$

This is helpful for our wanted, on the substrate InP, lattice matched (In,Ga)As layer.

Another feature of an one dimensional scan with a symmetrical reflex is the determination of the layer thickness. Good quality layers show thickness fringes beside the

main peak of a layer. These thickness fringes are not only usable for calculation of the thickness, they also give a hint of the quality of the grown layer. In good approximation we can calculate the thickness out of the distance between the thickness fringes as:

$$S = \frac{\lambda \cdot sin\epsilon}{t \cdot sin2\Theta} \tag{4.12}$$

with S being the spacing between fringes, t the thickness, λ the wavelength, ϵ the angle between sample surface and the diffracted beam. Another method is the measurement of a **r**eciprocal **s**pace **m**ap (RSM). To understand this scan method the principle of the reciprocal space and the Ewald construction will help us.
Starting with Fig.4.7, we see a two-dimensional diffraction plane of the scattering process with the wave vectors of the incident beam $\vec{k_i}$ and the diffracted beam $\vec{k_d}$. The incident angle ω_i is equal to the diffraction angle ω_d, meaning that we have elastic scattering and hence both wave vectors have the same length $\frac{1}{\lambda}$. The scattering vector (yellow arrow) is defined as the difference between k_i and k_d. By knowing the wavelength λ, we can deduct that all possible scattering vectors are on a circle around the origin of $\vec{k_i}$. These are the Ewald circles. In three dimensions the circles becoming spheres. We also have to take into account the size of the sample. Taking a look at the orange semi-circles, we see that they meet in the middle of the sample and that the diameter of one semi-circle is the radius $\vec{l}$ of the green semi-circle. That means we can write $\vec{l}$ as

$$\vec{l} = \vec{k_i} + \vec{k_d} = \vec{k_i} + \vec{k_i} = 2 \cdot \vec{k_i} = 2 \cdot \frac{1}{\lambda} = \frac{2}{\lambda} \tag{4.13}$$

Furthermore $2 \cdot \vec{l}$ gives us the maximum possible range because inside that semi-circle the maximum momentum change at backscattering is reached. This is clear when we take a look at the angle 2Θ. It becomes 180° when maximum momentum change is measured. In our XRD measurements we are using the so-called Bragg geometry meaning that the angle of incident ω_i and diffraction ω_d is greater than zero. With that geometry the areas inside the orange Ewald circles are not reachable.
For the Ewald construction of diffraction explained above, the reciprocal space of a crystal[2] is needed. The conversion from real space with the basis vectors $\vec{a_1}, \vec{a_2}, \vec{a_3}$ to reciprocal space with the basis vectors $\vec{b_1}, \vec{b_2}, \vec{b_3}$ follows section 4.2 as:

$$\vec{b_1} = \frac{2\pi}{V}(\vec{a_2} \times \vec{a_3}) \qquad \vec{b_2} = \frac{2\pi}{V}(\vec{a_3} \times \vec{a_1}) \qquad \vec{b_3} = \frac{2\pi}{V}(\vec{a_1} \times \vec{a_2}) \tag{4.14}$$

Max von Laue[3] proclaimed for his theory that the scattering vector is a linear combination of integer of the reciprocal basis vectors $\vec{b_1}$, $\vec{b_2}$, $\vec{b_3}$. The derivation of the Laue condition can be found e.g. here [Kit01]. The Laue condition declares that constructive interference only occurs if the change of the wave vector $\Delta\vec{k}$ (= scattering vector) is a reciprocal lattice vector:

$$\vec{k_i} - \vec{k_d} = \vec{G} = \Delta\vec{k} \tag{4.15}$$

[2]lattice is present in 2 dimension and becomes a crystal in 3 dimensions
[3]* October 9, 1879 †April 24, 1960

4.3.2. Reciprocal space maps

When measuring a heterostructure using a symmetrical reflex e.g (002) or (004), with the measured data you can only obtain a good value for the vertical lattice constant $a_\perp$. To get information about how different layers are grown on a substrate, for example if you want to know if the layers are grown relaxed or strained or the lateral lattice constant, a reciprocal space map has to be measured. Here we give an explanation what a reciprocal space map is and how we can measure it.
For an easier understanding we use a simple cubic lattice with the lattice constant a_S. The reciprocal lattice is also a cubic lattice with the lattice constant $\frac{2\pi}{a_S}$. In Fig.4.11 a two

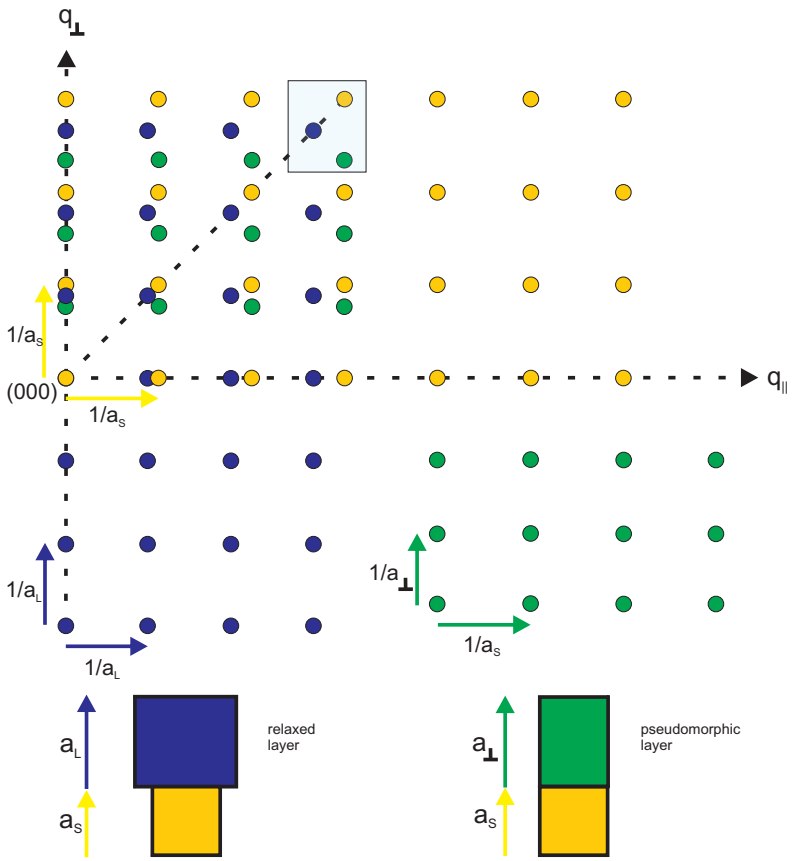

Figure 4.11.: Reciprocal lattice of cubic heterostructure. Position of the atoms if the layer is grown pseudomorphical (turquiose) on the substrate (yellow) or relaxed (blue).

dimensional cut through the reciprocal lattice of a heterostructure inside the diffraction plane is diagrammed. In a heterostructure the lattice constant of the substrate and the grown layers is different. Depending on how big this lattice mismatch is, the layer first starts to grow with the lateral lattice constant of the substrate $a_{S\parallel} = a_{L\parallel}$ and so the layer is grown pseudomorphical. For cubic crystals two cases have to be taken into account:

$$\begin{aligned} &(1) \quad a_S < a_L \quad \text{then} \quad a_{L\perp} > a_{L\parallel} \\ &(2) \quad a_S > a_L \quad \text{then} \quad a_{L\perp} < a_{L\parallel} \end{aligned} \tag{4.16}$$

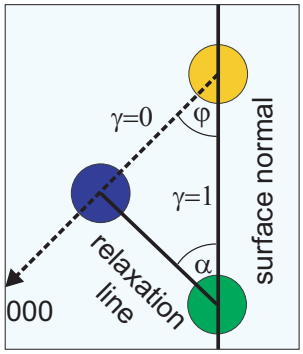

Figure 4.12.: Enlarged detail from 4.11. Reciprocal space map of an asymmetrcial reflex of a heterostructure.

In case (1) there is a compressive strain in $a_{L\parallel}$ and elongation in $a_{L\perp}$ and vice versa in case (2). At a certain point this energy reaches a level where dislocations can be created and the grown crystal starts to grow in its own lattice constant. From this point the grown layer is relaxed. With a two-dimensional scan we can determine the growth characteristics of different layers like the lattice mismatch or strain. With a measurement as shown in Fig.4.11 we can determine the lattice mismatch from layer to substrate. We have to discern two lattice mismatch parameters. First there is a lattice mismatch in growth direction. This parameter is defined as:

$$\frac{\Delta a}{a_\perp} = \frac{a_\perp - a_S}{a_S} \tag{4.17}$$

The nomenclature of the lattice constants in Eq. (4.16) is in conformance with Fig.4.11. For determination of this value a symmetrical reflex is sufficient. For the lattice mismatch of the lateral lattice constant of the substrate and the layer, an asymmetrical reflex has to be used and a reciprocal space map must be measured. It can be expressed like Eq.(4.17):

$$\frac{\Delta a}{a_\parallel} = \frac{a_\parallel - a_S}{a_S} \tag{4.18}$$

In the case of a pseudomorphicaly grown layer Eq. (4.18) becomes 0 and > 0 for a relaxed layer. But not only pseudomorphical or completely relaxed layers can occur, but also stages in between, meaning partly relaxed layers. Enlarging the light blue highlighted rectangle from Fig.4.11, we can determine the degree of relaxed, partly relaxed or pseudomorphical layers. For a pseudomorphical layer the substrate point and the layer point in reciprocal space are on the surface normal. On the other hand the points of a completely relaxed layer and the substrate are lying on the perpendicular line through the origin. The distortion parameter $\gamma = 1$ for a pseudomorphical layer and $=0$ for a complete relaxed. γ is defined as:

$$\gamma = 1 - \frac{\frac{a_\parallel - a_S}{a_S}}{\frac{a_L - a_S}{a_S}} \tag{4.19}$$

For our work it would desirable to have $\gamma = 1$ for the (In,Ga)As and NiMnSb layers. Measurements of reciprocal space maps are presented in chapter 7.

4.3.3. Reflection high energy electron diffraction

With RHEED we are able to investigate the surface of grown layers. The electron beam hits the surface at an angle smaller than 3°. We are talking about a grazing incident electron beam.
In a very simple way the situation at the surface is diagrammed in Fig.4.13. In a)

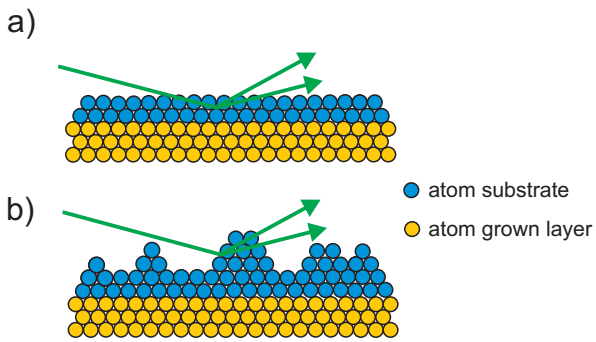

Figure 4.13.: At electron diffraction at a surface reflection a) and transmission b) can occur.

the growth of the layers occurs under the *Frank van der-Merve* growth mode and the incident electron beam is reflected from the flat surface. But if the surface is not flat like in b) the electron is not only reflected but also transmitted through some parts of the upper layers. When the diffracted electron beam now hits the fluoresce display we see stripes for the reflected and spots for the transmitted beam. These observations give us an idea of the quality of the grown layers: are they flat or rough?

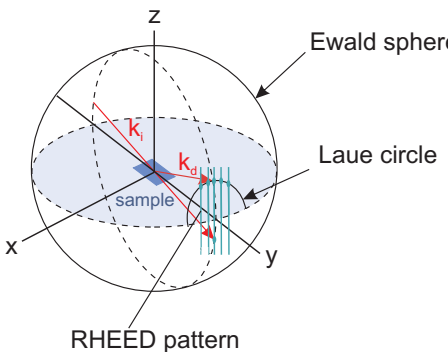

Figure 4.14.: Figurative RHEED configuration and important parts for understanding the principle of RHEED. Graphic in imitation of [Her89].

To understand the principle of RHEED and what we see on the RHEED display we assume elastic scattering for the incoming and scattered electrons. Again using the construction of the Ewald sphere in reciprocal space following chapter 4.3.1, the determination of constructive interference condition is possible. It can be seen in Fig.4.13 that the incident electron beam only interacts with a few monolayers at the surface. If a rod of the reciprocal space intersects the Ewald sphere the diffraction condition is fulfilled.
This circumstance leads to an extreme broadening of the reflected beam perpendicular to the sample surface and the electron beam "sees" a two-dimensional lattice instead of a three-dimensional lattice. As a result, the reflected beam appears as a vertical line and the reciprocal space of the sample surface can be treated as a series of infinite rods extending perpendicularly to the sample surface. Now we can describe the diffraction conditions as follows:

In our MBE system the RHEED technique is used with voltages between 15kV and 20kV. This means that our generated electrons have a high energy and a short wavelength. From chapter 4.3.1 we know that the radius of the Ewald sphere is $\frac{1}{\lambda}$. From this we can deduct that the Ewald sphere is much larger than the spacing between the reciprocal lattice rods. Where the rods are intersecting the Ewald sphere there is merely a weak bending of the sphere more that the rods now intersect a plane. The 0^{th} order line with the clearest spot is the specular spot. The lines from 1^{th} order or higher beside the 0^{th} order line are caused by the broadening of the Ewald sphere and the rods. This broadening is caused by defects during growth, thermal vibrations, the energy distribution of the electrons and the divergence of the electron beam. Fig.4.14 shows the principle construction of a RHEED with the Ewald sphere, Laue circle, sample surface and electron beam.
For the reason that this work is focused on the technique of growing epitaxial layers by molecular beam epitaxy and the necessary structural characterization methods to determine mainly the crystal quality of the grown layers, all magnetic and electrical characterization methods will be defined in a short version directly where the associated measurements are shown.

5. Growth on InP(001)

5.1. Pre-Advisements and sample structure

Wim van Roy and his group have already grown NiMnSb with molecular beam epitaxy [Roy00], [Roy01]. They used GaAs as the substrate.

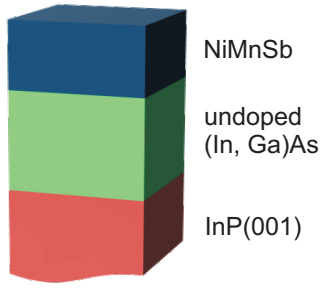

Figure 5.1.: Grown heterostructure on substrate InP(001)(red) with (In,Ga)As buffer layer (green) and NiMnSb (blue).

One problem with GaAs as the substrate is the difference in the lattice constants of GaAs and NiMnSb. The lattice mismatch is pretty high with a value of 4.4% . As a consequence NiMnSb starts to grow lattice-matched and after 2-3nm with its own lattice constant. This behaviour in general was already explained in section 4.3.2. The existence of a change from lattice-matched to relaxed growth leads to the creation of misfit dislocations. These misfit dislocations relieve the homogeneous strain energy till the energy is too weak and the layer starts to relax. This means that these created defects harm the electrical as well as the magnetic properties of NiMnSb. To obviate such possible problems it is desirable to grow NiMnSb on a substrate with nearly the same lattice constant.
Starting with the lattice constant from NiMnSb, we try to find a reasonable substrate with a similar lattice constant. Looking at the band gap vs. lattice constant graph in Fig.5.2, a good choice is InP. InP has a lattice constant $a_{InP} = 5.868$Å. Compared to the lattice constant from NiMnSb $a_{NiMnSb} = 5.903$Å, the lattice mismatch to NiMnSb is only 0.6%. As a buffer layer, which we need to get a flat surface for the growth start of NiMnSb, we are using the ternary semiconductor (In,Ga)As. This semiconductor can be grown lattice matched to InP with a mixing ratio of $In_{53}Ga_{47}As$. The complete heterostructure is diagrammed in Fig.5.1. All (001) oriented heterostructures are grown on InP(001) substrates from Inpact[1]. For samples with conducting substrate, a doping of S is used and for isolating a doping of Fe is used. The specification are listed in detail in Tab.1. All temperatures in the following chapters are read out by thermocouples. The resulting values could be up to 20°C less than the real present temperatures on the sample. One useful tool for obtaining the real present temperature is a pyrometer but unfortunately no pyrometer was available.

[1] www.inpactsemicon.com

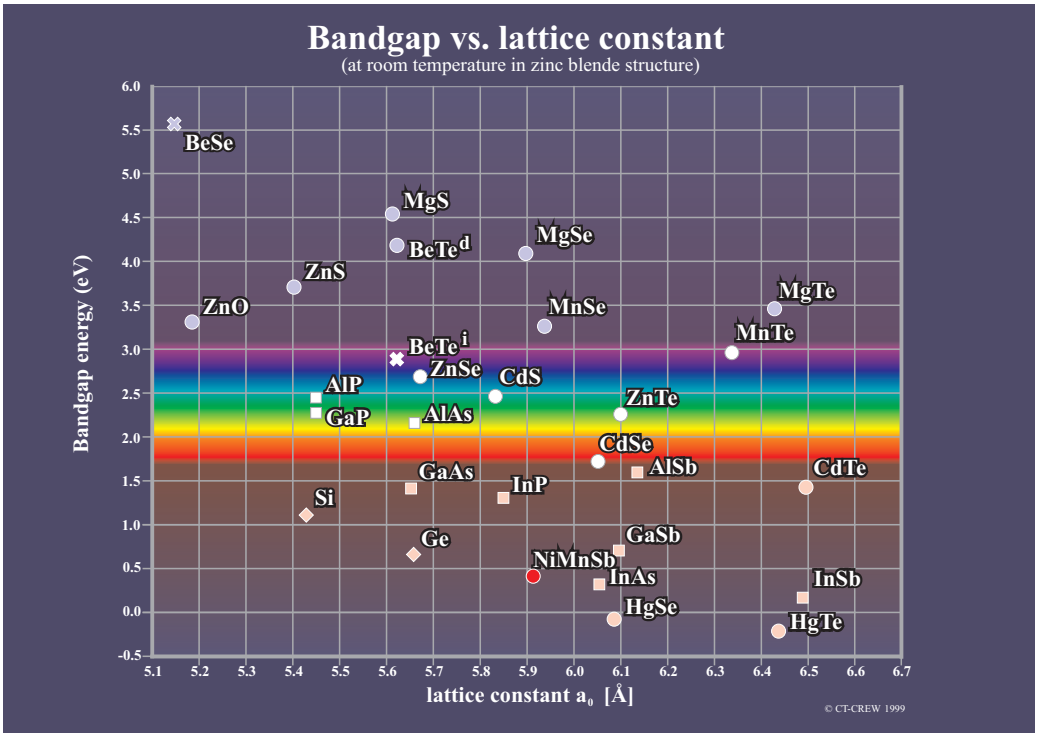

Figure 5.2.: Band gap versus lattice constant of different III-V and II-VI semiconductors. NiMnSb is marked red at a lattice constant 5.903Åand band gap energy of 0.5eV.

Parameters InP(001) substrates

Electrical			
Doping	S	Fe	undoped
Carrier concentration	$3 - 10 \cdot 10^{18}$	$1 \cdot 10^{7}$	$2 - 5 \cdot 10^{15}$
Mobility	1300-1600	N/A	4000-4600
Geometry			
Diameter (mm)	50+/-0.5	50+/-0.5	50+/-0.5
Thickness (μm)	350+/-25	350+/-25	350+/-25
Orientation	(100)	(100)	(110)°
Bulk			
EPD($/cm^2$)	< 500	< 30000	-
Xray diffrac. (FWHM)	12±1 arc sec	15±2 arc sec	-

Table 5.1.: Properties from different doped InP(001) substrates manufactured by Inpact (www.inpactsemicon.com).

5.2. Sample preparation

Before we can use our substrate in the MBE-Cluster at Experimentelle Physik 3, we have to glue it to a molybdenum holder which fits into all necessary equipment. Under atmospheric pressure the molybdenum holder is put on a hotplate at 200°C. As glue we use In formed in pellets. With a forceps one In pellet is taken and pressed on the molybdenum block. After a few seconds the In pellet starts to melt and it can be dispersed on the surface of the molybdenum holder. Only the area of the size of the substrate should be covered by the In glue and also the layer thickness of the glue should be thin.
If a too large area is covered with In or too much In glue is on the holder different problems can occur during the growth process. On the one hand if there is too much In it can diffuse in the substrate and change the electrical and structural properties. On the other hand if the glue layer is too thick the desorption point is changed and can lead to higher degas temperatures and accordingly desorption of P of the InP substrate is possible and a rough surface is created.
In the next step the substrate can be placed on the molybdenum holder and moved slightly in all directions to get a sufficient sticking. Now the sample can be brought into the MBE-Cluster.
With a system of carts on chains the samples can be moved into the UHV system. The first process step is the removal of any humidity from the sample with the heating station, see Fig.4.5. The temperature is set to 250°C and kept there for 10min. After cooling down to 200°C the sample can be transferred into the chamber GaAs I for the growth process of the buffer layer (In,Ga)As. The details of this process are described in the following section.

5.3. Growth process buffer layer (In,Ga)As on InP(001)

After the substrate is degased at the heating station, it is transferred to the GaAs I chamber. The first step is the desorption of the protective oxide layer. When the substrate holder temperature of the GaAs I chamber is 200°C or less, the substrate is inserted into the chamber. While rotating all the time with a temperature gradient of 20K/min, the substrate is heated up. At 300°C an As_4 overpressure is established to obviate the desorption of phosphor when the oxide layer starts to desorb. At $\approx$ 475°C a (2x4) reconstruction is visible and becomes broader at 490°C with a clear specular spot. It is important to observe this reconstruction because we need it for the determination of our growth temperature.
In Fig.5.3 the RHEED pattern for the observed reconstruction is shown. When the oxide layers desorbs, the reconstruction changes to (4x2). This normally happens in the temperature range between 510°C - 530°C. The growth temperature can now be determined as follows: take actual temperature when the surface reconstruction changes from (2x4) to (4x2) and round up to the next full decade. This value is our desorption temperature T_{Des}. That point plus 10°C is our heating temperature T_{Heat}, minus 10°C

from the desorption point is our growth temperature T_{Growth}. Fair values are 522°C → desorption temperature T_{Des} = 530°C → heating temperature T_{Heat}= 540°C → growth temperature T_{Growth}= 520°C. The substrate is left for 1s at the heating temperature T_{Heat} before cooling down to growth temperature. To get a constant temperature over the complete sample, we wait 60s before opening the In und Ga shutter when growth temperature is reached. Directly after opening the shutters from the group III elements the reconstruction switches in a short period of time to (2x4). This should happen in a time range of 10s. Longer times are a sign of a too high growth temperature and a pronounced 3D RHEED pattern directly after growth start is a sign of a too low growth temperature. It is possible to see some roughness at the growth start. After 120s the RHEED pattern should only show flat parts. To get a 180nm thick (In,Ga)As layer

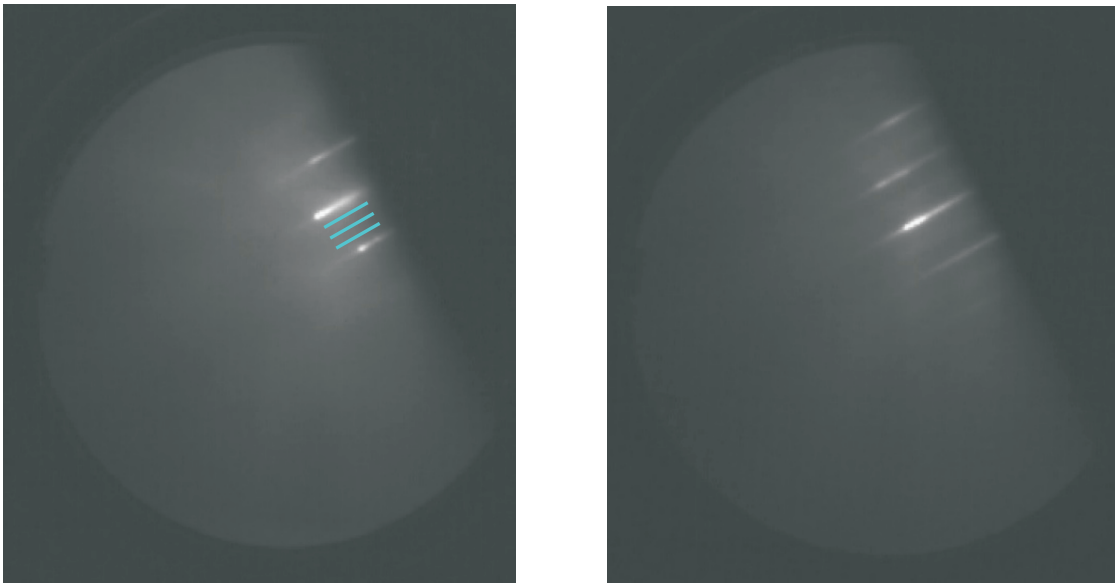

Figure 5.3.: RHEED pattern while growing (In,Ga)As on InP(001) at estimated growth temperature. The $\frac{d}{2}$ streaks along [110] direction are clearly visible (right). Along [1$\bar{1}$0] direction the $\frac{d}{4}$ are weak. For better visibility the streaks are marked in the RHEED pattern.

we have to leave all shutters open for 1476s. This means that we have a growth rate of $1.22\frac{\mathring{A}}{s}$. After closing the shutters from In and Ga, the sample is cooled down with 20K/min. The As_4 overpressure is kept alive up to a substrate temperature of 350°C to prevent the desorption of As from the buffer layer. Now the valve of the As cracker cell is closing. During the cooldown the RHEED pattern switches again from (2x4) to (4x3) around 480°C. When the growth of (In,Ga)As is done, we have a flat surface and the sample is ready for the growth of NiMnSb. After cooling down to 200°C the sample is transferred to the NiMnSb chamber. At this temperature a (4x3) reconstruction, flat with a clear and sharp specular spot, is still visible (Fig.5.4).

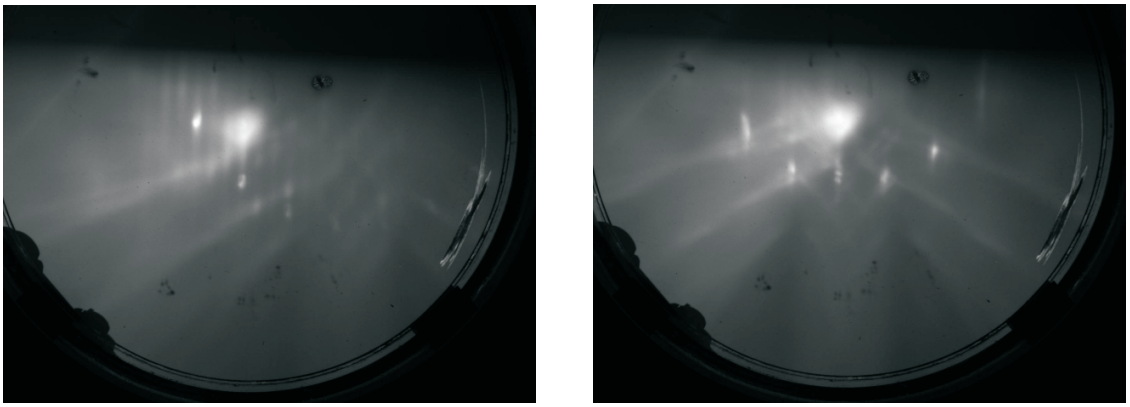

Figure 5.4.: RHEED pattern (In,Ga)As on InP(001) at 200°C. Sample is already transferred into the NiMnSb MBE chamber. Along [110] direction the $\frac{d}{4}$ streaks are visible (right). Along $[1\bar{1}0]$ direction the $\frac{d}{3}$ are visible.

5.4. Growth process NiMnSb on (In,Ga)As/InP(001)

In the early stages, NiMnSb was grown on GaAs(001) ([Roy00],[Roy01]) and also on InP(001) by MBE ([Bac05],[Bac03]) and sputtered ([Eic07], [Ris00]). ([Roy00],[Roy01]) and ([Bac05],[Bac03]) used the following flux ratios:

- Sb:Ni = 10:1
- Mn:Ni = 3:1

We now use these flux ratios:

- Sb:Ni = 14.5:1
- Mn:Ni = 4.2:1

Not only the flux ratios are different: a main change in our growth process is that the Ni cell now works under the melting point of Ni [2]. This has large-scale consequences for the growth. First of all the flux density from all cells is lowered by one magnitude. That also means that the growth rate is changed to a lower value. The growth conditions are considerably different to the growth parameters from [Bac05].
At a substrate holder temperature of $200°C$, the sample from GaAs I chamber is put into the NiMnSb chamber and heated with a ramp of 10K/min to the growth temperature of $250°C$. From [Bac05] it has been shown that this temperature provides a good growth of NiMnSb on (In,Ga)As. When the sample is heated to growth temperature the substrate rotation is already turned on. Following Fig.4.6, first the cell shutters of Ni, Mn and Sb are opened for 600s while the main shutter is closed. We do this to get more stable fluxes than before where the time was 180s [Bac05]. While the main shutter is closed we can see a clear (4x3) reconstruction from (In,Ga)As layer with a clear specular

[2] the melting point from Nickel is $1455°C$

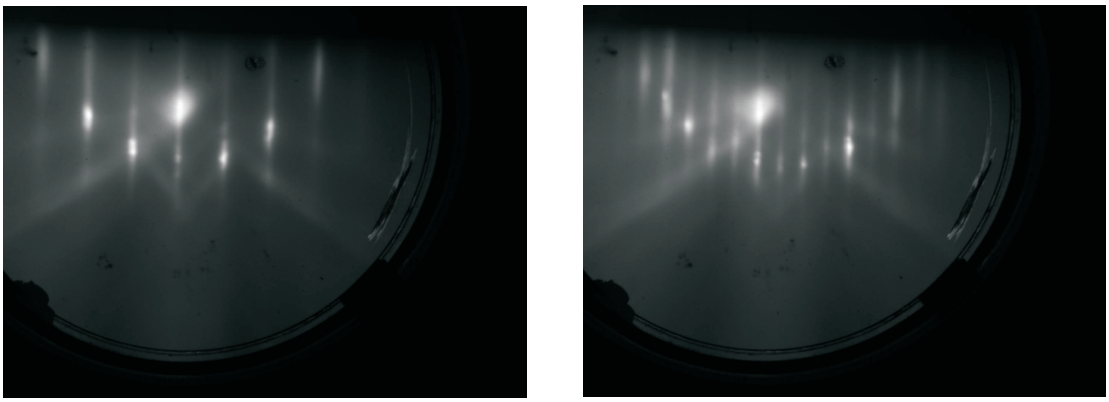

Figure 5.5.: RHEED pattern NiMnSb on (In,Ga)As/InP(001) while growing at 250°C substrate temperature. Along [110] direction the $\frac{d}{2}$ streaks are clearly visible (right). Along [1$\bar{1}$0] direction the 1 reconstruction is seen.

spot (Fig.5.4), like already observed in the GaAs I chamber. The growth starts with the opening of the main shutter. After 20s the buffer reconstruction changes to (2x1) from NiMnSb with an absolutely clear visible specular spot (Fig.5.5). There are no signs of roughness in the RHEED pattern. After 2-3nm a slight roughness can occur and is not visible any more after 1nm again. When the wanted thickness of the layer is reached all shutters are closed and the sample is cooled down without any temperature gradient. When the substrate temperature of 200°C or less is reached, the sample can be transferred out of the chamber. One part of our produced stacks are taken out directly to atmospheric pressure, the other parts are transferred to the in-situ metallisation station and a Ti/Au capping layer is deposited.
Fig.5.6 shows a flow-chart of the main steps for growing NiMnSb layers on InP(001). Keep in mind that this flow-chart only includes in-situ characterisation tools and observations during growth. It is indispensable to do x-ray diffraction measurements on the grown sample.

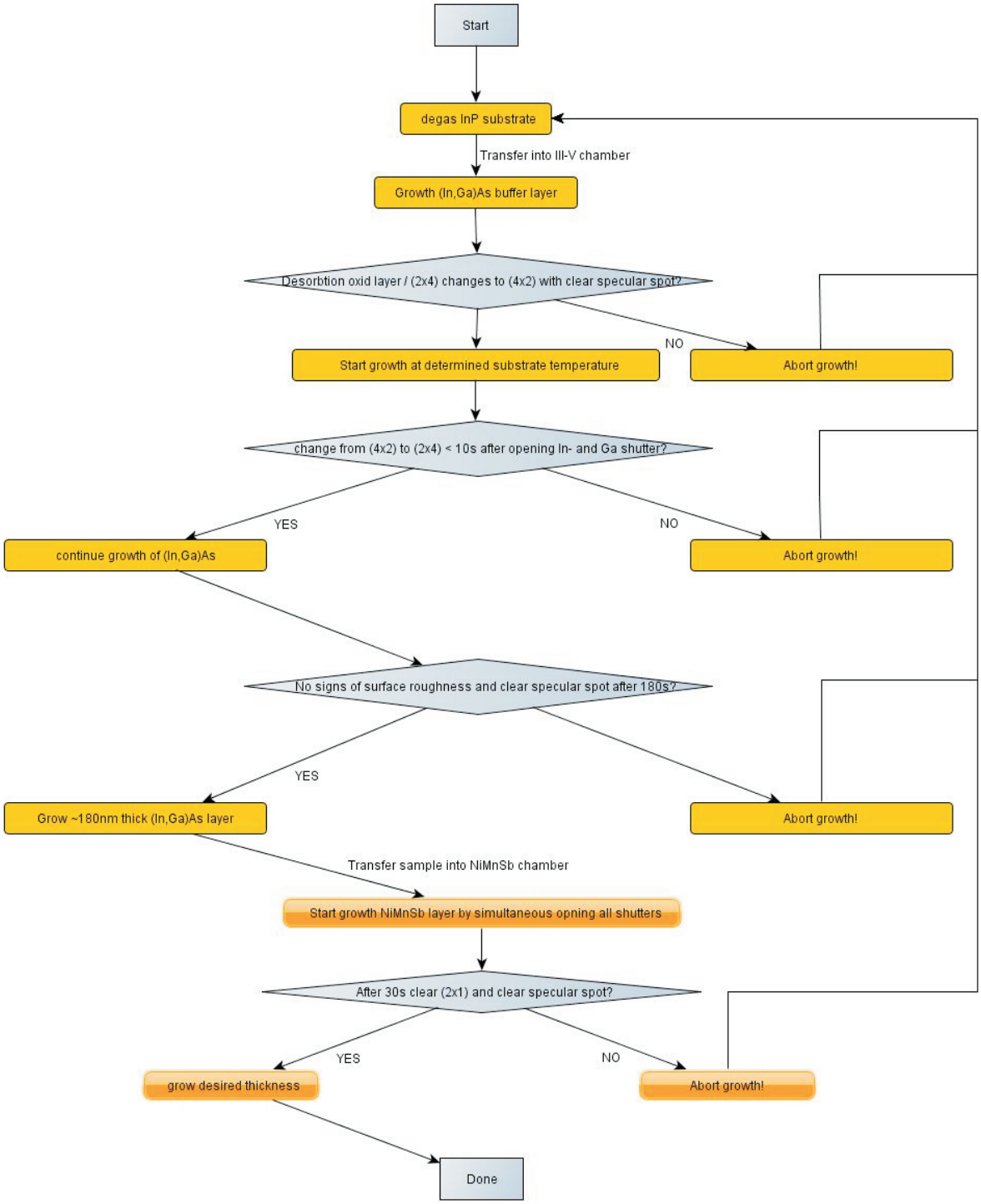

Figure 5.6.: Flow-chart of the main steps for growing NiMnSb layers on InP(001) substrate with a lattice matched (In,Ga)As buffer layer.

6. Growth on InP(111)

Remembering the properties of NiMnSb described in chapter 2 and its special feature with two different band-structures, one for the majority and one for the minority charge carriers, NiMnSb would be a perfect spin injector at room temperature.

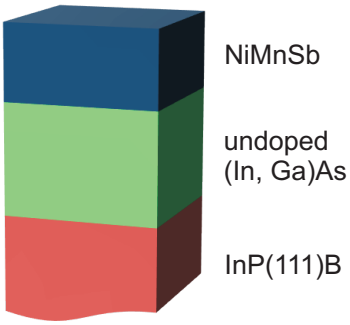

Figure 6.1.: Grown heterostructure on substrate InP(111)B(red) with (In,Ga)As buffer layer (green) and NiMnSb (blue).

But to take advantage of this property, we can not use (001) oriented NiMnSb. Theoretically it has been shown that only (111) interfaces are half-metallic [Wij01]. For realising a so-called spin injection experiment, a n-doped semiconductor is needed. In our case we are able to grow n-doped (In,Ga)As. As a substrate we have to use an (111) oriented starting material. The complete grown heterostructure is shown in Fig.6.1. First of all we take a look at the (111) surface. There are two possible configurations, A and B. In an InP crystal A represents Indium and B Phosphor. S.S. Bose, W.I. Wang *et al.* [Bos88] have shown that Si can act as an acceptor or donor in GaAs(111). [Bos88] has demonstrated that Si is a n-dopant for (001), (211), (311), (511), (711) and (911). For A-sides only up to (311) planes Si is a p-dopant. For all higher index planes Si always behaves as a n-type dopant. When using B-side (111) Si is a donor and the GaAs layer is n-doped, otherwise using A-side (111) substrate, the GaAs layers is p-doped. This termination type dependence was investigated with grown samples on different oriented substrates. In the case of [Bos88] they used GaAs(001), GaAs(311)A and GaAs(311)B substrates and did Hall measurements, Photothermal Ionization spectra and Photoluminescence spectra. In Fig.6.2 a summary of all measurements is shown. There it is clearly visible that Si acts as a n-dopant for (001) and (311)B oriented layers and as a p-dopant in (311)A oriented layers. The results of Bose *et al.* combined with those of Wang *et al.* lead to the assumption that it is very likely that (In,Ga)As grown in InP(111)B substrates will result in a n-doped (In,Ga)As layer when using Si as a doping material.

6.1. The (111) surface

The difference in the A and B configuration of an (111) oriented InP crystal can be seen in Fig.6.3. Topside is the (111)A-side from the zinc blende InP crystal terminated with In atoms. The bottom side represents the (111)- side terminated with P atoms. For

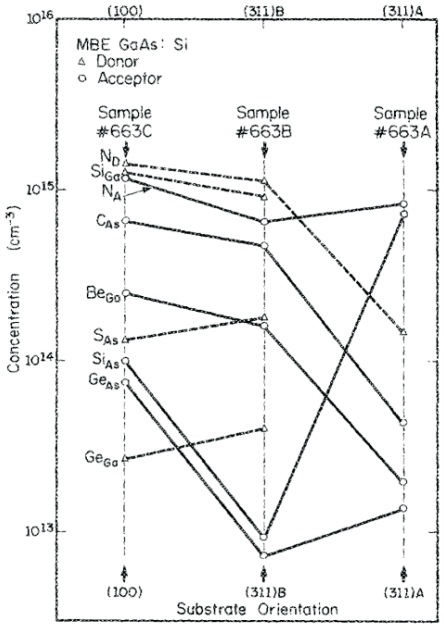

Figure 6.2.: Concentrations of the total donor and acceptor impurities and the individual impurities for three orientations. The solid lines indicate acceptor concentrations and the dashed lines indicate donor concentration. From [Bos88].

clarity the crystal direction $[110], [1\bar{1}0]$ and $[111]$ are marked in the crystal structure. There it can be seen that the In atoms are located on a line in $[110]$ direction and the Phosphor atoms are located on a line in $[1\bar{1}0]$ direction. Contrary to InP(001) the (111) oriented InP crystal has three instead of two cleaving edges, namely $[1\bar{1}0], [10\bar{1}]$ and $[01\bar{1}]$. The three cleaving edges are symmetrical identical and enclose an angle of 60°. This rotational symmetry behaviour leads to an additional problem in epitaxial growth. It is possible that the impinging atoms crystallize in the wurtzite structure. This is clear when looking at the symmetrical properties of a zinc blende and wurtzite crystal. Both can be transferred into each other by rotation of 60° along [111] (zinc blende) respectively [1111] (wurtzite).
Another issue is the almost inert behaviour of a (111) surface concerning in particular the low sticking coefficient of impinging atoms on such a surface. This leads to the case that an atom floats over the surface and attaches itself to a little existing step on the surface. These little steps are distributed randomly over the surface. But this also means that over time more and more atoms nucleate at these steps and bear a bigger size which leads to a rough surface and creates other planes than (111) oriented. But this would destroy our chance of achieving 100% spin-polarization in our NiMnSb layer. If these kinds of defects occur we are talking about pyramid-like defects. To avoid this problem a (111) substrate with a little miscut of about 1°-2° in $[11\bar{2}]$ is used. This means that the crystal is cut along $[11\bar{2}]$ direction. This direction points into the surface. The resulting steps are acting as nucleation centres. The surface of the step terraces are still (111) oriented. This growth is known as the "step flow" growth mode [Rat93]. Not

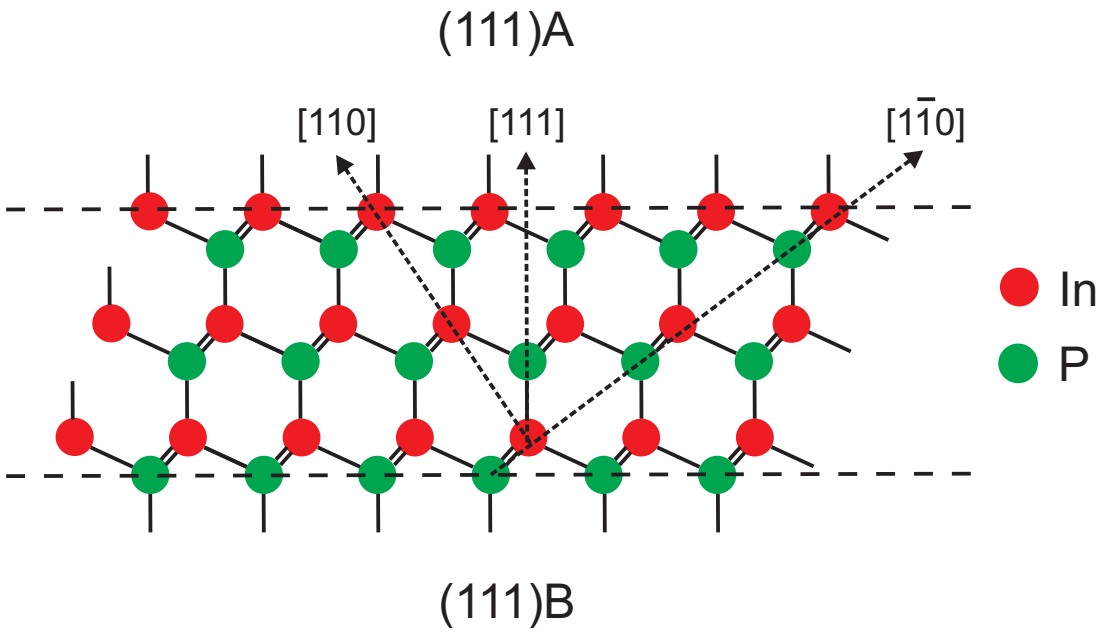

Figure 6.3.: InP(111)viewed along the [01$\bar{1}$] direction, showing A(In) and B(P) surfaces.

all defects mentioned above can be avoided with this "trick", but they can be reduced significantly. Fig.6.4 shows an (111) oriented substrate with a miscut along [11$\bar{2}$].

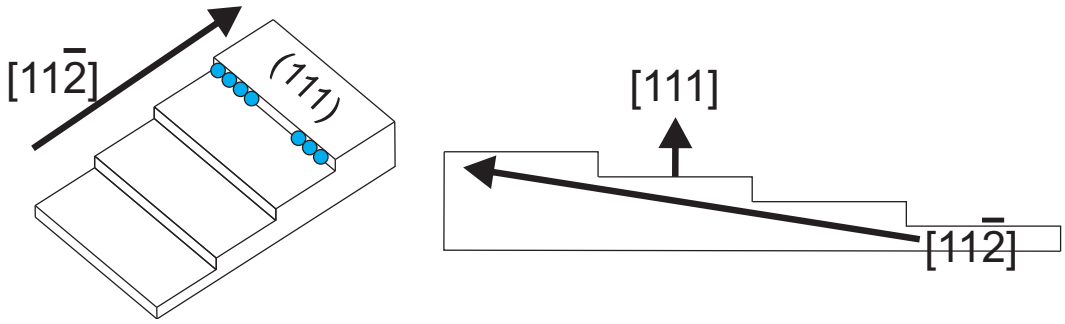

Figure 6.4.: *Left:* The steps caused by the miscut along [11$\bar{2}$] are acting as nucleation centers for the impinging atoms (blue). *Right:* Side view of (111) oriented surface with created steps by the miscut along [11$\bar{2}$]. The terrace surface normal is parallel to the [111] direction.

6.2. Growth process

The growth process on InP(111) is different to the growth on InP(001). First we have to decide whether we take A or B side substrates. In early stages of growing NiMnSb at Experimentelle Physik 3 the difference in growth on both orientation sides have been investigated [Bac05]. Out of these results we have chosen InP(111)B for our growth project. The InP substrates are glued with In on molybdenum blocks and degased for

Parameters InP(111) substrates

Dopant	**Resistivity** $[\Omega \cdot cm]$	**Mobility** $[cm^2V^{-1}s^{-1}]$	**Carrier Conc.** $[cm^{-3}]$
Fe	Not specified	>= 1000	Semi-insulating

Table 6.1.: Properties from doped InP(111) substrates manufactured by Wafer Technology Ltd. (www.wafertech.co.uk).

10min at 250°C at the heating station.
Afterwards the samples are transferred to the III-V-chamber GaAsI to grow the (In,Ga)As buffer layer 4.5. Different parameters while growing (In,Ga)As on InP(111)B have to be taken into account:

- degas time
- ratio III:V
- waiting time at growth temperature before shutters are opened

In comparison to the growth on InP(001) it is much more difficult to determine the desorption point of the oxide layer. Because of this problem we have taken the average value of the determined desorption temperature from InP(001) plus 10°C. This leads to a value of 540°C. The influence of the waiting time at that temperature can be seen in Fig.6.5. It's clear that 1s is better in our case because the surface roughness is lower.

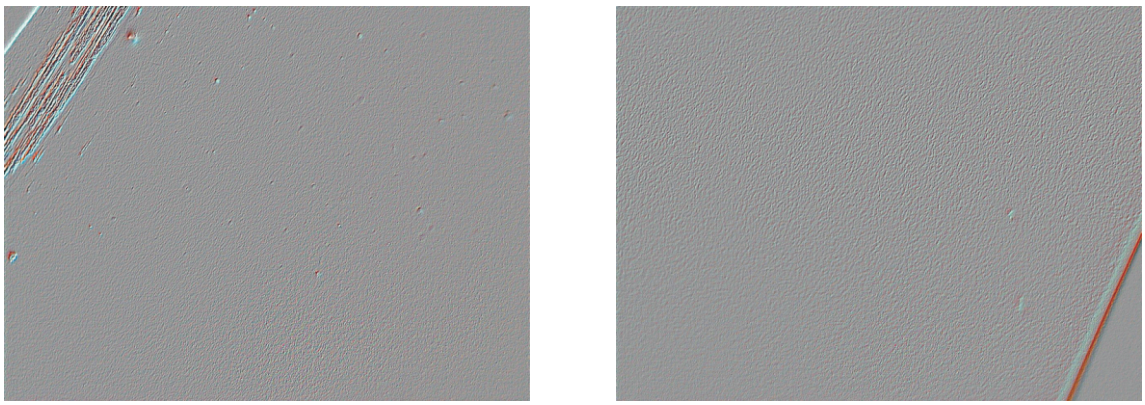

Figure 6.5.: Influence of waiting time at heating temperature T_{Heat} between 1s (*left*) and 60s (*right*).

To have a constant temperature gradient the waiting time at the growth temperature is varied. We change this time from 60s to 120s and detect that 120s is the better choice as can be seen in the Nomarski pictures in Fig.6.6.

6.2.1. Buffer layer (In,Ga)As on InP(111)B

The growth of the (In,Ga)As layer on InP(111)B has some additional problems than growing on InP(001). First, as a result of the different surface configuration of InP(111)B, the desorption temperature can not be determined in the easy way like on InP(001). We

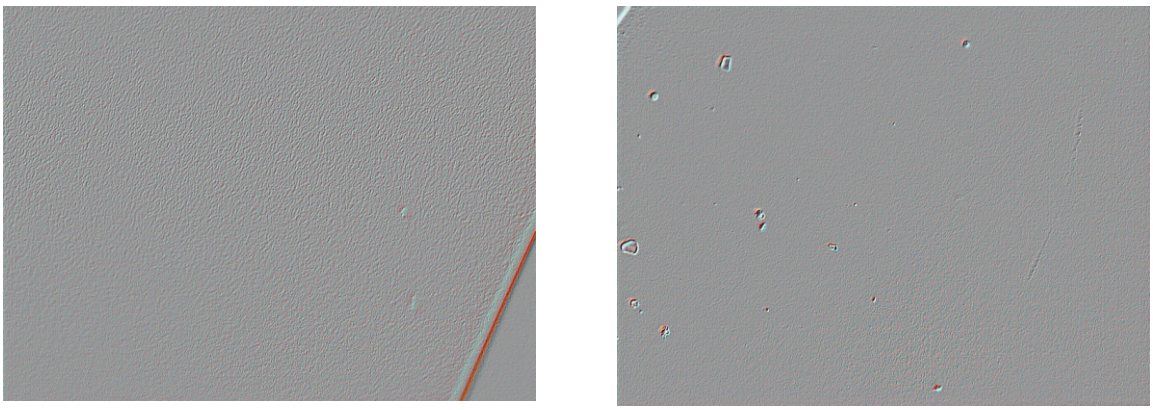

Figure 6.6.: Influence of waiting time at growth temperature T_{Growth} before growth starts between 60s (*left*) and 120s (*right*).

do not see the characteristic change in the RHEED pattern from (2x4) to (4x2). The only hint when the desorption of the oxide starts is a change in the specular beam spot. But mostly the exact point is hard to identify. For our buffer layers we decide to take as the degas temperature T_{Heat} = 540°C, keep it for 1s and cool down to T_{Growth}=530°C and wait for 120s before the In and Ga shutters are opened. Starting with degasing the sample in the heating station for 10min at 250°C, it is transferred into the III-V chamber. Starting at a substrate temperature of 200°C, the sample is heated with 30K/min up to 300°C. Now the As overpressure is established. Its value is $1.2e^{-5}$ Torr. At 300°C the heating speed is reduced to 20K/min and the sample is heated up to T_{Heat} and then lowered to T_{Growth} (see above for the values of T_{Heat} and T_{Growth}). Before the shutters of In and Ga are opened, the pressure from As is lowered to $3.3e^{-6}$ Torr. The following ratios are presented during the growth process:

- As : In,Ga = 10.4
- In : Ga = 2.3

The growth time is 1476s and results in a layer thickness of about 180nm. Fig.6.7 shows the RHEED pattern from a 100nm thick (In,Ga)As at 530°C along $[1\bar{1}0]$ and $[11\bar{2}]$. In no direction a reconstruction can be seen. After the desired growth time, the In and Ga shutters are closed and the As pressure is raised again to the value $1.2e^{-5}$Torr. At 350°C and falling, the As valve and shutter is closed and at 200°C the sample get out of the III-V chamber and transferred under UHV conditions into the NiMnSb chamber. This growth process is described in subsection 6.2.3.

6.2.2. n-doped (In.Ga)As on (In,Ga)As/InP(111)B

To get a n-doped (In,Ga)As layer, Si is used as a donor (see section 6 and [Bos88]). The cell temperature from Si is set to 980°C. No flux measurement is possible because the flux from Si is too low to get a good value in combination with the background pressure inside the chamber. The growth process follows the description in 6.2.1. Additional to

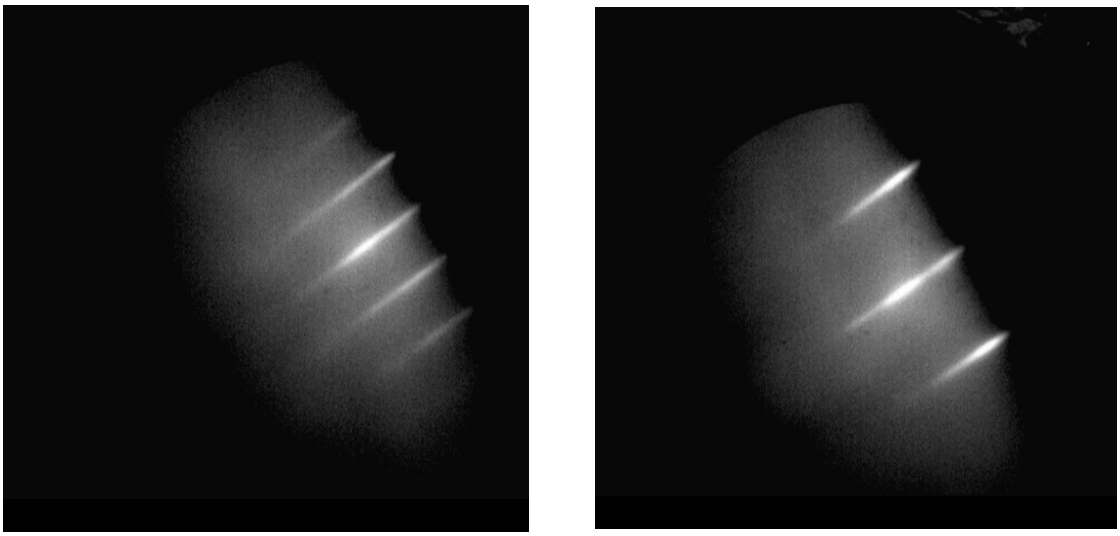

Figure 6.7.: Reconstruction of a 100nm thick (In,Ga)As layer on InP(111)B at 530°C. In no direction a reconstruction can be seen, $[1\bar{1}0]$ *left* and $[11\bar{2}]$ *right*.

the 180nm undoped (In,Ga)As layer, a 20nm thick n-doped (In,Ga)As layer is grown by opening the Si shutter in addition to the other open shutters. No change in RHEED pattern is observed. This is clear because in a perfect n-doping process the Si atoms occupy lattice spots from the group-III elements.
All growth parameters are the same as for the undoped layer. The measurements of the doping concentration are topic of chapter 7.2.2.

6.2.3. NiMnSb on (In,Ga)As/InP(111)B

For the growth of NiMnSb on InP(111)B the same parameters are used as for growth on InP(001). After the InP(111)B substrate with doped or undoped buffer layer is transferred, the sample is heated to 250°C with 10K/min and the sample holder is rotating. The flux ratios are set to:

- Sb:Ni = 14.5:1
- Mn:Ni = 4.2:1

Again the main shutter is 600s closed longer than the shutters of the three elements Ni, Mn and Sb to obtain stable fluxes from the effusion cells. Directly after opening the main shutters the growth starts with a unreconstructed RHEED pattern. After 20s the RHEED pattern changes to an (2x2) along $[1\bar{1}0]$ and (6x6) along $[11\bar{2}]$ reconstruction. Fig.6.8 shows both visible RHEED pattern. In both directions a clear specular spot is present with long main streaks and no spots. In both directions the second order streaks are clearly visible, all streaks next to the main streaks are not visible. In addition the d/2 streaks along $[11\bar{2}]$ direction are very weak. The d/3 streaks on the other hand are quite strong in this direction. These observations are a hint for a low surface roughness. After

$\approx$ 10nm the specular spot gets diffuse and the transmission effect of the electron beam appears, which means that the *layer-by-layer* growth is interrupted and thus leads to a rough surface (see section 4.3.3). Compared with the growth of NiMnSb on InP(001),

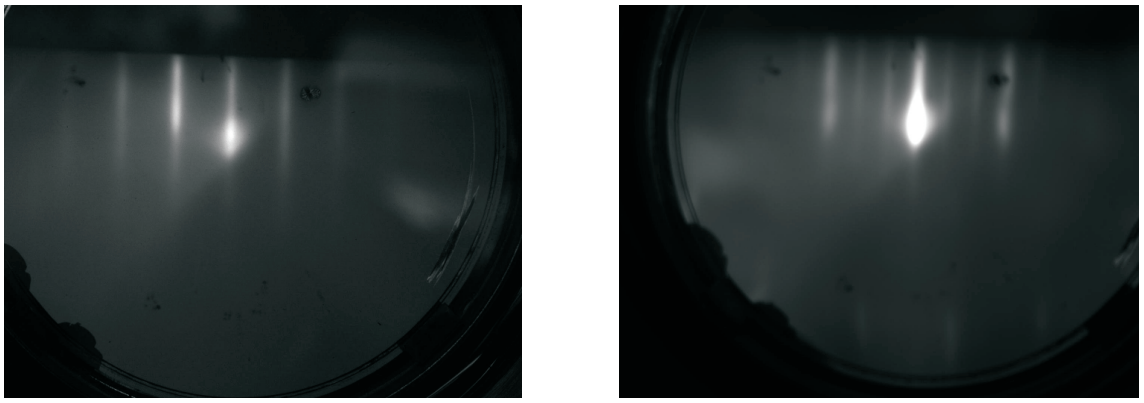

Figure 6.8.: Reconstruction of a 5nm thick NiMnSb layer on InP(111)B at 250°C. *Left:* (2x2) reconstruction along $[1\bar{1}0]$.*Right:* (6x6) reconstruction along $[11\bar{2}]$.

the roughness of the grown layer at $\approx$ 10nm appears very early. A possible explanation for this behaviour is the fact that the used vicinal surface can help to prevent the creation of twin and pyramid-like defects but not a 100%. This means that at a certain point it is energetically favourable for the crystal to grow in a different geometry than at growth start. As a consequence only layers up to a thickness of a maximum of 10nm can be used for spin injection samples.

7. Quality and properties

In the early stages of the growth process from NiMnSb, different flux ratios and temperatures were used to produce NiMnSb layers on (In,Ga)As/InP respectively on GaAs/GaAs layers. The growth process of that time follows the description in [Bac05] chapter 4 (NiMnSb (001)) and chapter 8 (NiMnSb (111)) for NiMnSb on (In,Ga)As/InP and [Roy00], [Roy02] for NiMnSb on GaAs/GaAs(001). The obvious difference between growing NiMnSb on GaAs substrates and InP substrates is the lattice mismatch to NiMnSb. When comparing the lattice constants

- $a_{NiMnSb} = 5.903$Å
- $a_{InP} = 5.868$Å
- $a_{GaAs} = 5.653$Å

we get a lattice mismatch of 4.4% compared to GaAs and 0.6% compared to InP, leading to a much earlier relaxing of the grown NiMnSb layer on GaAs. This chapter gives an overview of the achieved quality and properties reached with our new growth process and also gives a comparison of differences to NiMnSb layers grown on InP with the old process and on GaAs. For (111) oriented InP substrates undoped (In,Ga)As and n-doped (In,Ga)As on InP(111)B and NiMnSb on undoped (In,Ga)As/InP(111)B are considered.

7.1. Layers on (001) oriented substrates

7.1.1. Structural properties

Buffer layer (In,Ga)As

As mentioned before the aim of the buffer layer is to provide a flat surface for the growth start of NiMnSb. With HRXRD technique we are able to determine the structural quality of our produced layers ex-situ. For our measurements we use the high-resolution x-ray diffractometer from Philips with the wavelength Cu$K_{\alpha 1} = 1.54059$Å. As already explained in chapter 4, with *Bragg's law* an evidence about the quality of the layer can be made. With a symmetrical reflex, like (004), the intensity of the peaks shows how many parallel planes are in the grown crystal and accordingly a more or less well-ordered crystal can be expected. When we are looking at the (004) reflex measurement of a (In,Ga)As on InP(001) sample(Fig.7.1), we see clear thickness fringes in the complete measurement range from 30.15° up to 31.9°. The amount and clearness of the thickness

fringes give us proof of very flat interfaces in the grown layer. At 31.05° the peak from InP is visible. The slightly asymmetrical form of the peak is caused by the not absolutely lattice-matched buffer layer (In,Ga)As. But the buffer layer is still in the range of good lattice match to the substrate. We are able to determine the thickness by using the position of the thickness fringes. With the kinematic step model introduced by Segmüller and Blakeslee [Seg73] it is possible to determine the thickness of the (In,Ga)As layer. In the measurement shown in Fig.7.1 we get a thickness of 185nm. By knowing the growth time of the buffer layer we are able to determine the growth rate from (In,Ga)As on InP(001) as

$$growthrate = \frac{layer - thickness}{growth - time} = \frac{185nm}{1517s} = 1.22\frac{\mathring{A}}{s} \tag{7.1}$$

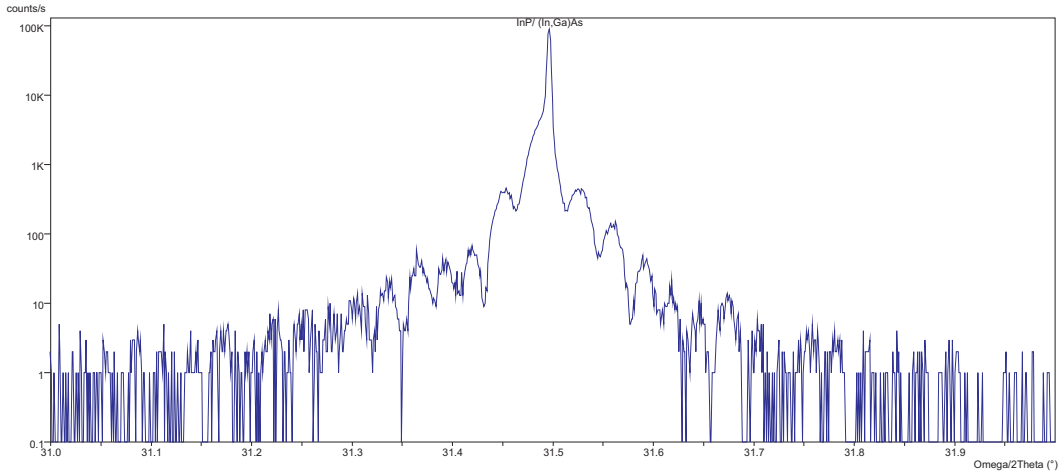

Figure 7.1.: HRXRD measurement from (In,Ga)As on InP(001). The (004) reflex is used for measurement.

Half-metallic ferromagnet NiMnSb

To calculate the growth rate of NiMnSb we determined the thickness of NiMnSb with a symmetrical HRXRD-scan and divided the received thickness by the time the shutters of all three effusion cells were opened. With a thickness of 400Åand a growth time of 6240s we get with 7.1 a result for the growth rate of NiMnSb $growthrate_{NiMnSb} = 0.0641\frac{\mathring{A}}{s}$. Vice versa that means e.g. that we need a growth time of 3120s for a 20nm thick layer. With HRXRD we examined the (002) reflex. This reflex has a higher intensity for the half-Heusler layer. Fig.7.2 shows the measured data. The substrate peak is visible. It includes the perfect lattice-matched (In,Ga)As layer. Due to the fact that the lattice constant from NiMnSb is slightly larger than InP (0.6%), the resulting peak is on the left side of the substrate peak. From the peak position from NiMnSb we can calculate the vertical lattice constant with *Bragg's law* and Eq. (4.9) to $a_{vertical-NiMnSb} = 5.960$Å. If

we implicate the lattice constant between substrate and half-metallic ferromagnet plus the measuring inaccuracy into the calculation we get the following:

$$a_{NiMnSb-Lit} = 5.903\mathring{A} \Rightarrow 0.6\% = 0.035\mathring{A} \tag{7.2}$$

The measurement inaccuracy in respect to the measured lattice constant

$$a_{NiMnSb-measured} \Rightarrow \pm 0.5\% = 0.0298\mathring{A} \tag{7.3}$$

With that values we can calculate:

$$a_{\perp-NiMnSb} - 0.035\mathring{A} = 5.925\mathring{A} \tag{7.4}$$

This value is in good agreement inside the error bars with the value found in literature [Cas55]. With the measurements of the (002) reflex we can give statements concerning

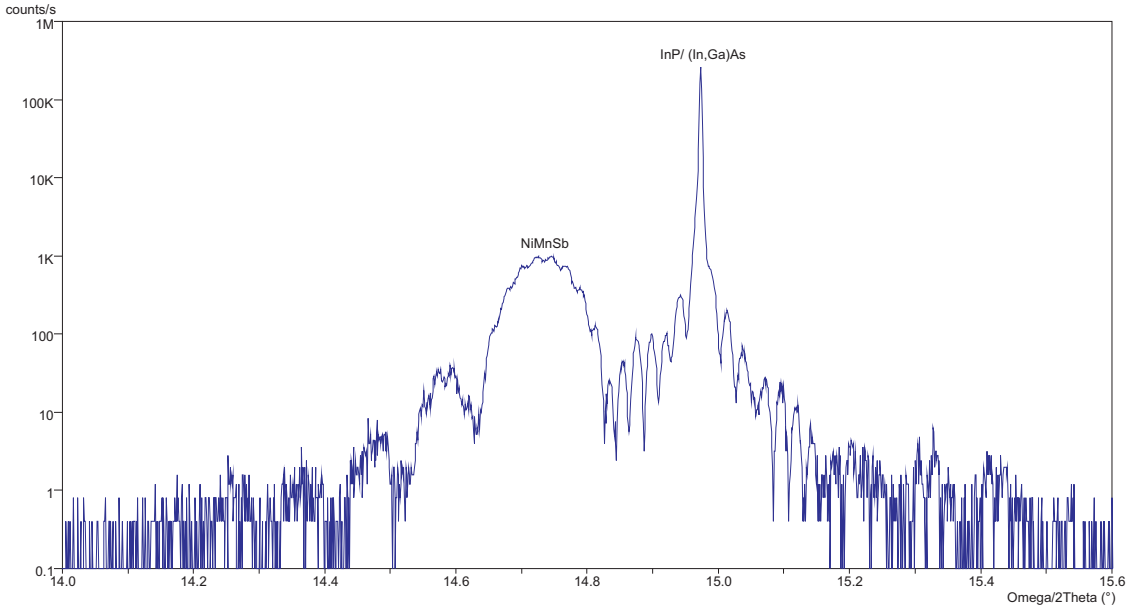

Figure 7.2.: HRXRD measurement from NiMnSb/(In,Ga)As on InP(001). (002) reflex is used for measurement.

the crystal quality of the grown NiMnSb layer. Between 14.65° and 14.8° the peak from the NiMnSb layer is visible with a maximum intensity of more than 1000 counts/s. Additional thickness fringes of the NiMnSb layer and the buffer layer are present. The NiMnSb thickness fringes are visible again over a wide range from 14.1° to 15.5°. As a comment, the peak from (In,Ga)As is completely covered by the InP peak. Compared with XRD measured from samples grown with a higher growth rate and different flux ratios by [Bac05] show one big difference. When calculating the vertical lattice constant in our sample compared to samples from Bach, we have achieved a closer value to the substrate lattice constant and to the wanted lattice constant of NiMnSb found in literature in combination with a good structural quality. This means that we have

significantly improved the growth process of NiMnSb on (In,Ga)As/InP(001).
Fig.7.3 shows two HRXRD scans from almost equally thick NiMnSb layers (41nm vs. 42nm) grown on undoped (In,Ga)As/InP(001). The red dyed data (41nm) is from a NiMnSb layer grown with the best flux ratios from [Bac05]:

- Sb:Ni = 10:1
- Mn:Ni = 3:1

and the black dyed data (42nm) is grown with the new flux ratios (see section 5.4) used in this work. It is clear that with the new flux ratios a better lattice match to the substrate is achieved in addition to a higher intensity of the NiMnSb peak, 800 counts versus 1150 counts, with the result that the crystal quality is higher than before. Wim

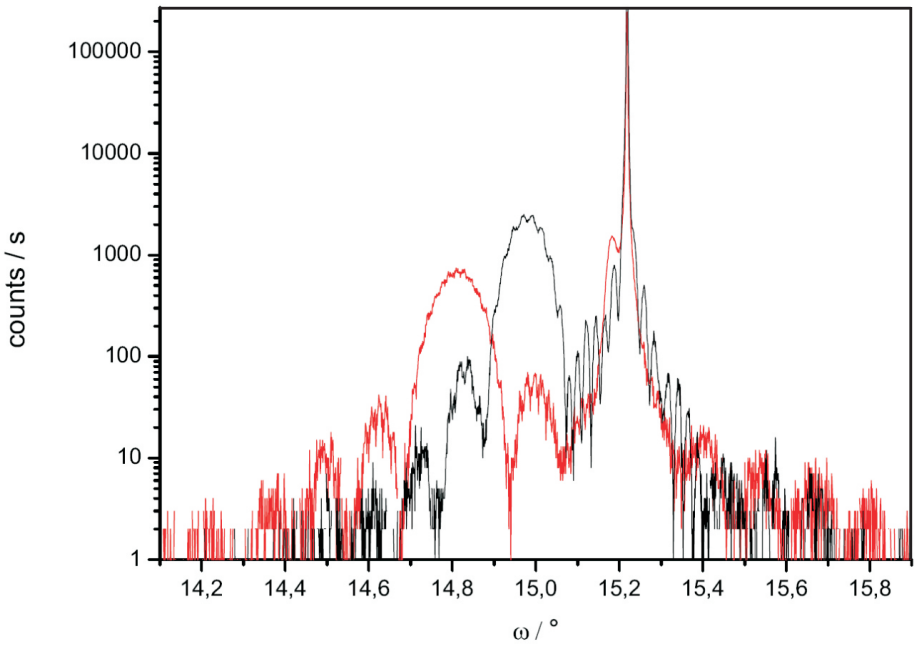

Figure 7.3.: HRXRD measurement from NiMnSb/(In,Ga)As on InP(001). Red: old flux ratios, black: new flux ratios. (002) reflex is used for measurement.

van Roy also did XRD measurements with our samples and compared the measurements with his NiMnSb/GaAs(001) samples. The measurements are shown in 7.6. The aim of the measurements was to analyze the sample on any conclusions inside the NiMnSb layer. All binary compounds from Ni, Mn and Sb can form possible inclusions, namely NiSb, MnSb and NiMn. As a comment NiMn is very unlikely and the focus was only on NiSb and MnSb. All measurements were done using the $(1\bar{1}1)$ reflex. The green line in Fig.7.6 is the data from our sample. No inclusions of any form could be detected. In the Sb-rich sample (red line), many inclusion of MnSb and NiSb are detected. This result seems to be illogical because we have also grown our NiMnSb layer with an excess of Sb.

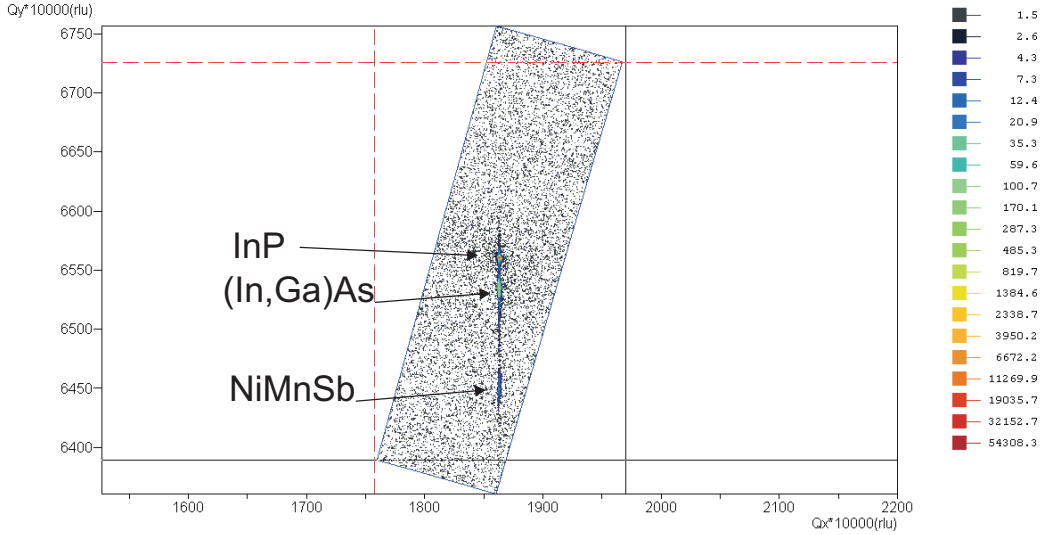

Figure 7.4.: Reciprocal space map of a 40nm thick NiMnSb layer on (In,Ga)As/InP(001) measured with the Philips X'Pert HRXRD. The marked peaks from InP, (In,Ga)As and NiMnSb are all on a perpendicular line indicating a pseudomorphical growth of the buffer and half-metallic ferromagnet layer on the substrate.

This leads to the assumption that the big lattice mismatch between substrate and buffer to NiMnSb causes an excess of Sb to nucleate at the crystal defects in the grown layer before they are build in the crystal and Ni and Mn start to create the binary compounds NiSb and MnSb. The Sb-poor sample shows the same behaviour like our sample. One problem which is still under discussion are the peaks at 29.5°, 59.55°, 92.6° and 95.5°. This peaks can be caused by a MnAs layer created at the interface between (In,Ga)As terminated with As and the Mn atoms when growing NiMnSb.
With a symmetrical reflex only the vertical lattice constant can be measured and no evidence about the lateral lattice constant can be made. We have access to this parameter. A reciprocal space map with an asymmetrical reflex has to be measured. Fig.7.4 shows such a reciprocal space map. On the left side the data of the (115) reflex scan is shown with special units on both axes. We see that all three peaks corresponding to InP, (In,Ga)As and NiMnSb are on one vertical line indicating a pseudomorphic growth of the (In,Ga)As and NiMnSb layer (see chapter 4.3.2). The axes of the reciprocal space map shown in Fig.7.4 are in reciprocal lattice units. These units are dimensionless and are representing the Miller indices (hkl). In our reciprocal space map scan, using the (115) reflex, the Miller indices h and k are equal. The y-axis is in direction to [00l] and the x-axis in [hh0] direction. With this precondition we can convert the reciprocal lattice constants $q_{\parallel}$ and $q_{\perp}$ into the real space lattice constants $a_{\parallel}$ and $a_{\perp}$ with the following

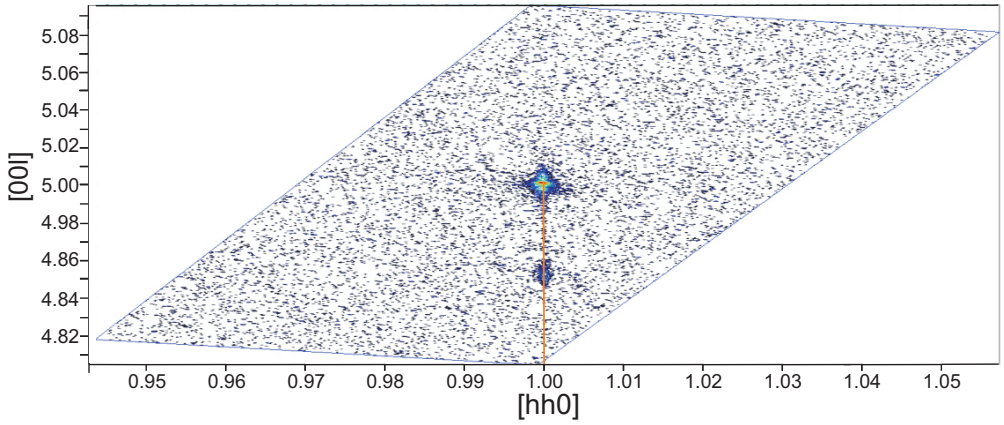

Figure 7.5.: (115) reflex used for reciprocal space map of a 40nm thick NiMnSb layer on (In,Ga)As/InP(001) measured with the Philips X'Pert HRXRD with [hh0] along the x-axis and [00l] along the y-axis. The red, perpendicular line is at [hh0] = 1. The peaks are all on that line indicating a pseudomorphical growth.

equation:

$$\begin{pmatrix} q_{\parallel} \\ q_{\parallel} \\ q_{\perp} \end{pmatrix} = \begin{pmatrix} h \\ k \\ l \end{pmatrix} \cdot \begin{pmatrix} \frac{a_{sub}}{a_{\parallel}} \\ \frac{a_{sub}}{a_{\parallel}} \\ \frac{a_{sub}}{a_{\perp}} \end{pmatrix} \tag{7.5}$$

From Fig.7.4 we know that the InP, (In,Ga)As and NiMnSb peaks are on one straight, perpendicular line. This means that all peaks have the same [hh0] value. With the result from Eq.7.5 and a_{sub} is a_{InP}, we can calculate the [00l] value from the NiMnSb peak to 4.9519. For the InP peak the [hh0] value is 1, because $a_{sub} = a_{InP} = a_{\parallel}$. This implicates that the [hh0] value from the NiMnSb peak is also 1 and $a_{\parallel - NiMnSb}$ has the same value as InP, namely $a_{\parallel - NiMnSb}$= 5.868Å. The measured data in Fig.7.4 can now be plotted in $q_{\parallel}$ and $q_{\perp}$ along [hh0] and [00l] as shown in Fig.7.5. The distortion parameter γ can now be calculated with Eq. (4.19) as:

$$\gamma = 1 - \frac{\frac{a_{\parallel} - a_S}{a_S}}{\frac{a_L - a_S}{a_S}} = 1 - \frac{5.868\mathring{A} - 5.868\mathring{A}}{5.925\mathring{A} - 5.868\mathring{A}} = 1 - 0 = 1 \tag{7.6}$$

This result means that we have a complete pseudomorphical grown NiMnSb layer on InP(001).
The relaxation behaviour of NiMnSb and how it can be influenced will be discussed in section 7.1.3. But not only the crystal quality is improved, but also the magnetic quality. The results are the topic of the next section.

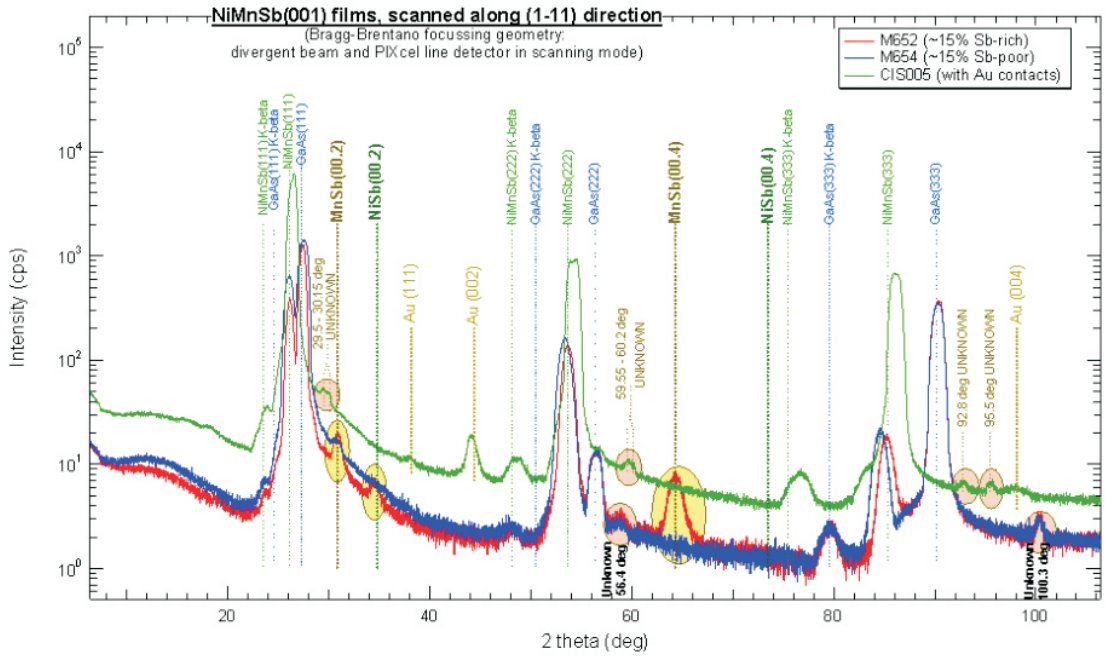

Figure 7.6.: XRD measurements from NiMnSb layers with different Sb content on GaAs(001) compared to NiMnSb layer on InP(001) using the $(1\bar{1}0)$ reflex. With NiMnSb layer grown on InP(001) no inclusions can be detected.

7.1.2. Magnetic properties

It is interesting and necessary to investigate the magnetic properties of NiMnSb, which is a half-metallic ferromagnet. In this work, two different techniques are used to determine these properties. These are FMR and SQUID.

Ferromagnet resonance

With FMR we can measure the magnetic properties like anisotropies and magnetic damping. In principle we detect the precessional motion of the magnetization in our NiMnSb samples.
In our setup, we apply a transverse rf[1] field with microwaves of 8-14 GHz and sweep the magnetic field from 0 to 300mT. When applying a magnetic field, the total magnetic moment of the sample starts to precess around the local field $\vec{H}_{eff}$ of the NiMnSb sample. This precessional motion of the magnetization is described by the Landau-Lifshitz-Gilbert equation:

$$\frac{\partial \vec{M}}{\partial t} = -\gamma(\vec{M} \times \vec{H}_{eff}) + \frac{G}{\gamma M_S}[\vec{M} \times \frac{\partial \vec{M}}{\partial t}] \tag{7.7}$$

[1] radio frequency

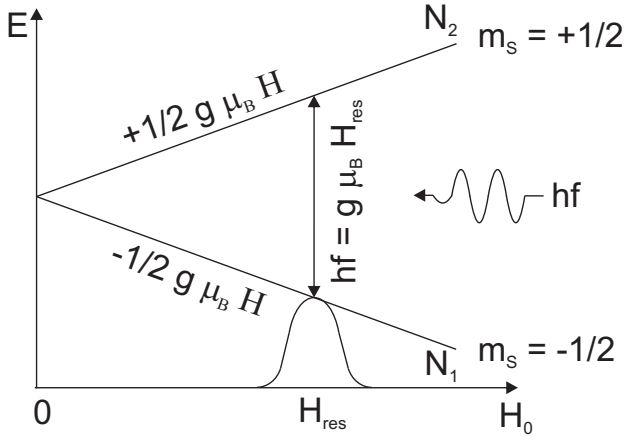

Figure 7.7.: Used principle by FMR measurements. An applied magnetic field $\vec{H}_0$ excites a Zeeman splitting of the energy levels, $m_S = +1/2, -1/2$. A microwave excites a magnetic dipole transition between these Zeeman split levels.

G is the *Gilbert damping constant* and $\gamma = \frac{g\mu_B}{\hbar}$ the *gyromagnetic ratio*. To understand the measurement we start with Fig.7.7. The applied magnetic field $\vec{H}_0$ excites a Zeeman splitting of the energy levels, $m_S = +1/2, -1/2$. At the same time the microwave excites magnetic dipole transition between these Zeemann split levels. If a magnetic field is applied to a particle with a spin then this spin starts to precess around the applied $\vec{B}$ field with the Larmor precession[2] ω_{Larmor}. The Larmor precession depends on $\vec{B}$ and the gyromagnetic ratio as follows:

$$f_{Larmor} = \frac{\gamma}{2\pi} \cdot |B| \rightarrow \omega = \gamma \cdot |B| \tag{7.8}$$

Secondly the Zeeman splitting depends linear on $\vec{B}$

$$E_{pot} = m\mu_B B \tag{7.9}$$

If B is swept the spins start to precess around the applied magnetic field with ω and at a certain point ω/ω_{Larmor} is equal to the frequency of the rf microwave and an absorption occurs. In our FMR measurements we measure the absorption derivative from Eq. (7.8) and the direct signal. The direct signal shows a Lorentzian line shape with a line width ΔH. The line width is directly connected to the relaxation process. The Gilbert damping describes this relaxation process and accordingly gives us information about the magnetic quality of the investigated material.
To determine the damping value of a NiMnSb layer, we usually use the frequencies 8GHz, 12.5GHz and 14GHz for the rf microwave. When plotting the line width ΔH_{8GHz}, $\Delta H_{12.5GHz}$, ΔH_{14GHz} over the swept B-field and using a linear fit, the slope represents our damping value.

[2]named after Joseph Larmor, * July 11, 1857 †May 19, 1942

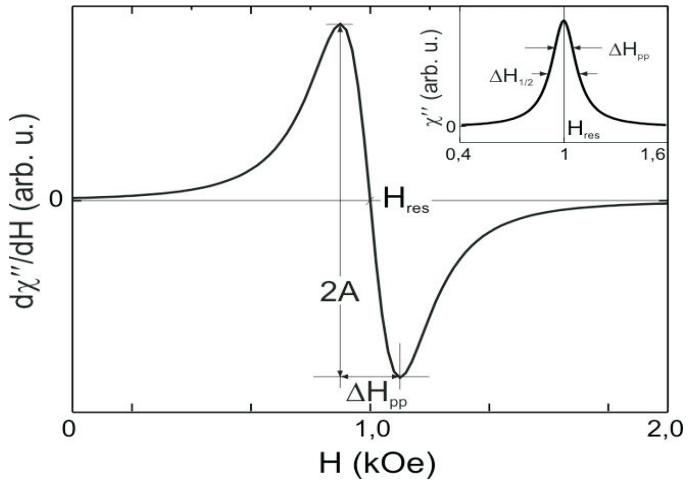

Figure 7.8.: FMR setup measures the absorption derivation and beside the direct signal (insert). The direct signal shows a Lorentzian line shape with a line width ΔH.

In the measurement procedure described above, the angle of the magnetic field and edge of the sample are not changed, here $\vec{B}||[110]$. To get access to the anisotropy behaviour or to see if there is actually any anisotropy, an angle-dependent scan is done. That means that we start with an angle of 0° ($\vec{B}||[110]$) and measure every 5° over 90° ($\vec{B}||[1\bar{1}0]$) up to 180° ($\vec{B}||[\bar{1}\bar{1}0]$) at a constant frequency. In our case the frequency is set to 12.5GHz. From that data we can determine the anisotropy field H_{ani} and the line width ΔH.
All measurements are performed at room temperature and the external field is applied in-plane. First, a set of measurements is done along the $[1\bar{1}0]$ direction at three different

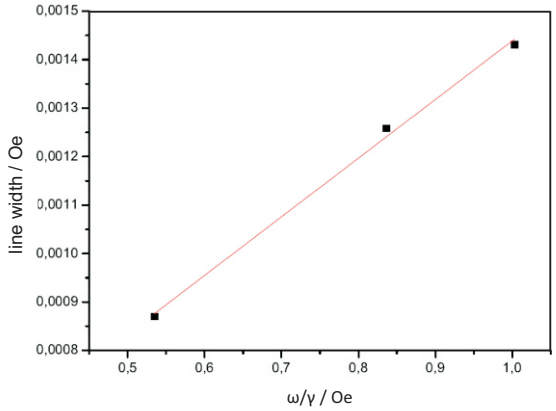

Figure 7.9.: FMR measurements of a 40nm thick NiMnSb layer at frequencies 8GHz, 12.5GHz and 14GHz for determination of α.

frequencies of 8GHz, 12.5GHz and 14GHz. The resulting line widths are shown in (Fig.7.9). From these values we obtain a damping value for the dimensionless parameter

α of $1.78e^{-3}$. We have to correct this result with an offset of 0.00141 caused by the FMR setup. As a final result we achieve a damping parameter $\alpha = 3.19e^{-3}$.
In order to investigate the crystalline anisotropy, angle-dependent FMR measurements are done at a frequency of 12.5 GHz. For these measurements the field is always kept in the plane and the angle is varied in steps of 5^o. The resonance field indicates a fourfold anisotropy with an anisotropy field of 50Oe (Fig.7.10)(black circles). The line width also reflects the fourfold anisotropy (Fig.7.10)(red circles). The minimum line width ΔH= 8 Oe. This line width ΔH is more than 4.88 times smaller than measured before by B. Heinrich *et al.*. Fig.7.11 shows the line width of NiMnSb layers with thickness 5nm (■), 42nm (▶) and 85nm ($\star$) measured by B. Heinrich *et al.*[Hei04] at a frequency of 24GHz. All three samples were grown with the parameters described in [Bac03]. The main difference in the growth process compared to our sample are flux ratios, growth temperature and effusion cells temperatures. Because of the linear dependency from ΔH and the frequency as described above, we can divide the value of ΔH in Fig.7.11 by 1.92 to compare it with our measured line width at 12.5GHz. As a result we have achieved a line width ΔH 4.88 times smaller than before. The circumstance that the

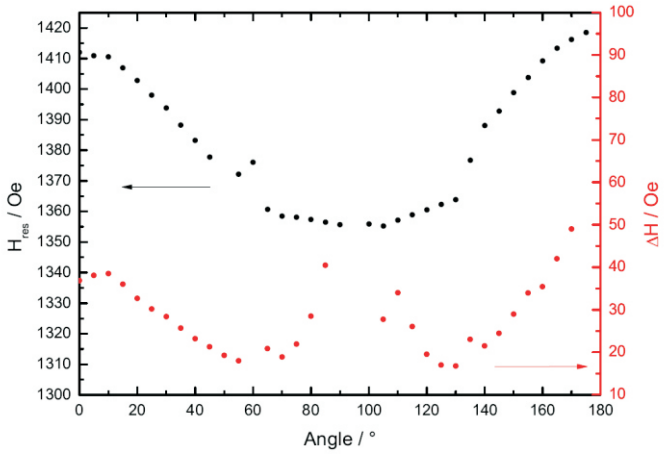

Figure 7.10.: Anisotropy behaviour in ΔH and H_{res} of a 40nm thick NiMnSb layer, measured at 12.5GHz.

line width in Fig.7.10 is not always low as 8 Oe and has a fourfold anisotropy leads to the assumption that the line width is direction dependent. To investigate this assumption, a NiMnSb layer is measured first in [100] direction and then in $[1\bar{1}0]$ direction with FMR. The result is shown in Fig.7.12. For [100] direction we receive $\alpha = 4.74 \cdot 10^{-3}$ and for $[1\bar{1}0]$ direction $\alpha = 3.33 \cdot 10^{-3}$. This means that the damping is changed of about 42% by changing direction. This result should be kept in mind when using NiMnSb as the material of choice for novel devices. As an additional result we have shown that we are able to produce high magnetic NiMnSb layers. The damping value α is lower than from Permalloy[3] $\alpha_{Py} = 6 - 7 \cdot 10^{-3}$ [Kob09], [Kal06] and in the same range like MBE grown Fe layers $\alpha_{Fe} = 4.33 \cdot 10^{-3}$ [Urb01].

[3]Permalloy = $Ni_{80}Fe_{20}$

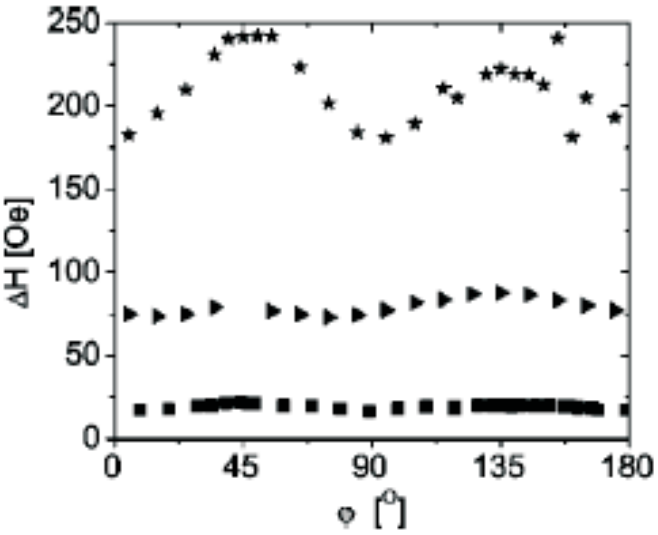

Figure 7.11.: FMR line width over the angle φ_m. φ_m is the angle between the external applied magnetic field and the in-plane [100]. ■,▶ and ⋆ corresponds to the thickness 5nm, 42nm and 85nm, respectively. For our measurements we compared the 42nm thick layer (▶). From [Hei04].

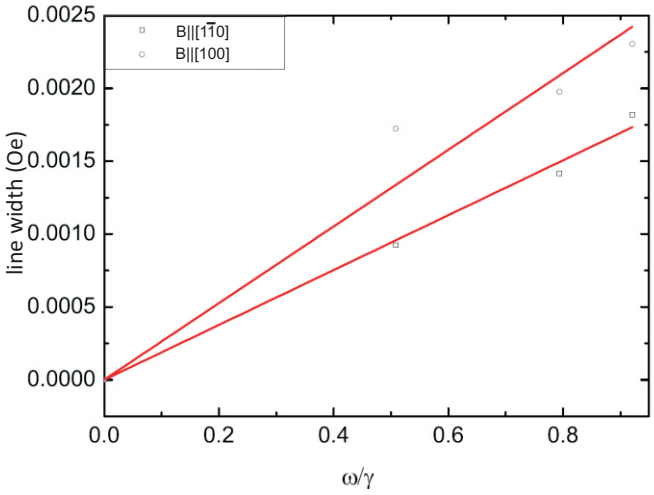

Figure 7.12.: Direction dependence of damping parameter α in NiMnSb layers.

Superconducting quantum interference device

With a SQUID fractional changes in magnetic fields and the saturation magnetization of magnetic layers can be detected. A SQUID is based on a system of superconducting detection coils with Josephson junctions. These junctions are a superconductor-non-superconductor-superconductor contact. One coil is the SQUID input coil and the others are the detection coils. The coils are connected with superconducting wires and all parts together build a superconducting loop. By moving the sample through the detection

coils, a current is induced in the coils. This leads to a small change in the magnetic flux in the detection coil and produces a change in the persistent current in the detection circuit. The SQUID converts this current change into voltage. This voltage is proportional to the magnetic moment of the sample. At Experimentelle Physik 3 a MPMS Controller Model 1822 is accessible. An external magnetic field is applied in-plane. All SQUID measurements were done by Dr. Charles Gould[4]. Before measuring a sample, it has to

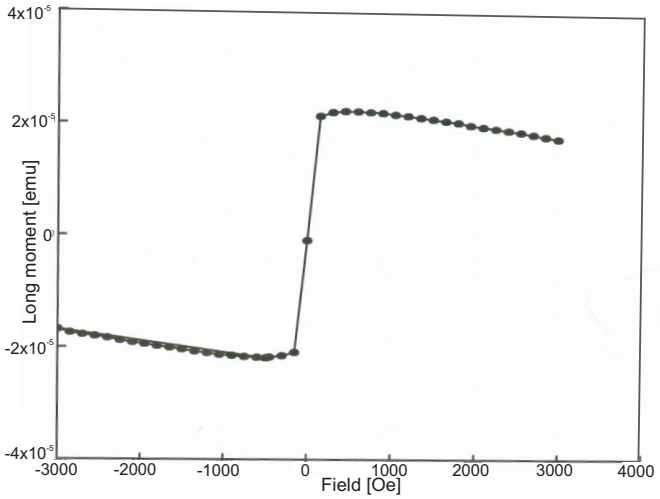

Figure 7.13.: Typical SQUID measurement of a NiMnSb layers.

be cut into a quad or rectangle of edge length 1.5mm up to 3mm. The edge length has to be measured with a calliper and the value should be noted. Also the thickness of the magnetic layer has to be known. It can be determined by different techniques like e.g. HRXRD or ***S**canning **E**lectron **M**icroscope* (SEM). As a result of the sample area, layer thickness and the SQUID data you can calculate the saturation magnetization M_s in units of *Bohr magneton* μ_B[5]. The value of μ_B is $9.27400915 \cdot 10^{-23} \frac{J}{T}$. Fig.7.13 shows a typical data produced by a SQUID measurement. From that graph we can determine graphically the magnetic moment in set-up-own-units [emu]. Now we are able to calculate the saturation magnetization M_S of the measured sample.
For our best investigated layer we receive a value of $M_S = 3.985\mu_b$. This value is almost identical to the value found in literature [Cas55],[Kab90]. This accordance to the value form literature emphasize the good quality of our magnetic layers.
It should be clear that this calculation has room for errors. First the inaccuracy when measuring with a calliper, second the graphical determination of the magnetic moment, third the determined thickness of the layer is afflicted with errors and last but not least the measuring inaccuracy of the SQUID set-up by itself with about $\approx 1\%$. As a conclusion, M_S values $\pm 5\%$ are in good agreement with the value found in literature [Cas55],[Kab90].

[4]gould@physik.uni-wuerzburg.de, tel.: +49 931 3185899
[5]Niels Bohr, * October 7, 1885 †November 18, 1962

7.1.3. Relaxation behaviour

In this subsection the relaxation behaviour of NiMnSb layers is discussed. For that experiments all layers were grown with the flux ratios

- Sb:Ni = 10:1
- Mn:Ni = 3:1

The influence of surface oxidation of the entire NiMnSb film is investigated by a comparison of Ti/Au capped and uncapped samples. The results have been published by Kumpf *et al.* [Kum07]. The work was done in a corporation between Experimentelle Physik 2 and Experimentelle Physik 3 from Würzburg university. The complete capping layer has a thickness of 20nm (10nm Ti + 10nm Au). All measurements are done at the synchrotron beamline BW2 of HASYLAB. To have the same properties of the capped and uncapped layers, the grown layers are transferred under UHV conditions in a in-situ metallisation. The capping layers are grown with shadow-mask technique, where one part is covered with a mask for preventing any Ti/Au on this side of the sample. By means of that process we have two identical samples with the only difference that one part is capped and the other uncapped. A six-circle-diffractometer is used for the **G**racing ***I**ncident* ***X**-**R**ay* ***D**iffraction* (GIXRD) measurements. The used wavelength is $\lambda = 1.29$Å. The following presented RSM measurements are performed in vertical z-axis geometry [Vli97],[Fei89]. The grazing incident angle of the beam is between 0.27° and 0.35°. The scans were done in a plane spanned by the l-direction and radial in-

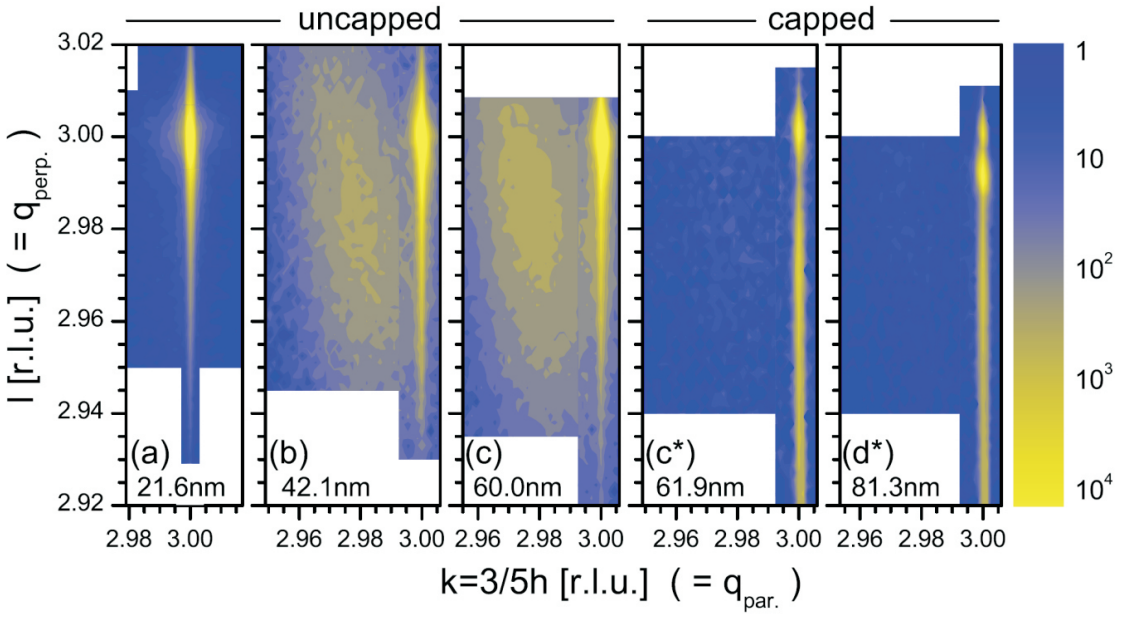

Figure 7.14.: Reciprocal space maps from capped and uncapped samples measured with GIXRD configuration at the synchrotron beamline BW2 at HASYLAB. Measurements from [Kum07].

plane-direction ($hk0$). l-direction is perpendicular to the surface and ($hk0$) direction is

parallel to the surface. With this geometry we have access to the vertical and horizontal relaxation behaviour in a RSM. The used reflex is (533).
Fig.7.14 presents five (533) reciprocal space maps. Sample notations (a), (b) and (c) are the uncapped ones and (c*) and (d*) are the Ti/Au capped ones. The measurements show a cut through reciprocal space in a plane defined by the direction normal to the surface and the (530) in-plane vector. The high intensity peaks at $q_{perp.} = 3.00$ and $q_{par.} = 3.00$ are from the InP and lattice-matched (In,Ga)As buffer layer. Only in (d*) the lattice match is not perfect, indicated as the second visible peak at $q_{perp.} = 2.99$ and $q_{par.} = 3.00$. The RSM shown in (c*) and (d*) have a clearly visible broad peak which is not seen in the RSMs (a), (b) and (c). In the uncapped samples this peak is nevertheless still present, just covered by the strong InP/(In,Ga)As peak and still causing an asymmetric broadening of that peak. The range of the presented RSMs contains the scattered intensity of materials which have the same lateral lattice spacing as the substrate meaning they all have the same *(hk)* position but a different vertical lattice spacing (smaller l-values). This means in our case, with InP as the substrate, (In,Ga)As lattice-matched buffer layer and NiMnSb, that by a pseudomorphic NiMnSb layer, its l-value is smaller. In (a), (c*) and (d*) this behaviour is only visible and accordingly all layers are grown pseudomorphically strained. In (b) and (c) we see some additional intensity in the region around *(h,k)* ≈(2.98, 2.98). This intensity is from the relaxed parts of the NiMnSb layers. There are still pseudomorphic parts of NiMnSb as well.
Comparing the thickness of the five samples we can conclude that the Ti/Au capping layer strongly influences the critical thickness of pseudomorphic growth from NiMnSb. Without a capping layer the NiMnSb layer starts to relax between 21.6nm and 42nm like seen in (a) and (b). It has been demonstrated earlier that the NiMnSb layer starts to relax around 40nm [[Bac05]]. With a capping layer a thickness of 81.3nm is reached without any relaxed parts from the NiMnSb layer (d*). While the capping layer was deposited directly after growth without breaking the UHV, the relaxation obviously occurs after growth when the sample leaves the UHV and enters air atmosphere.

7.2. Layers on (111) oriented substrates

As mentioned in the chapter about the growth process on InP(111)B substrates, it is more difficult to produce layers of good quality because of the difficulty to determine the accurate desorption point of the protective oxide layer and the higher sensitivity to the flux ratios. The structural examination starts again with HRXRD measurements. All here investigated layers are grown on InP(111)B substrates.

7.2.1. Structural properties

undoped and n-doped (In,Ga)As buffer layer

The sample consists of InP(111)B:Fe substrate and a ≈180nm undoped (In,Ga)As layer. The measurement uses the (444) reflex for the symmetrical $\omega - 2\Theta$ scan (Fig.7.15). Only one sharp peak can be identified at $\omega = 67.05°$. The absence of a second peak, which

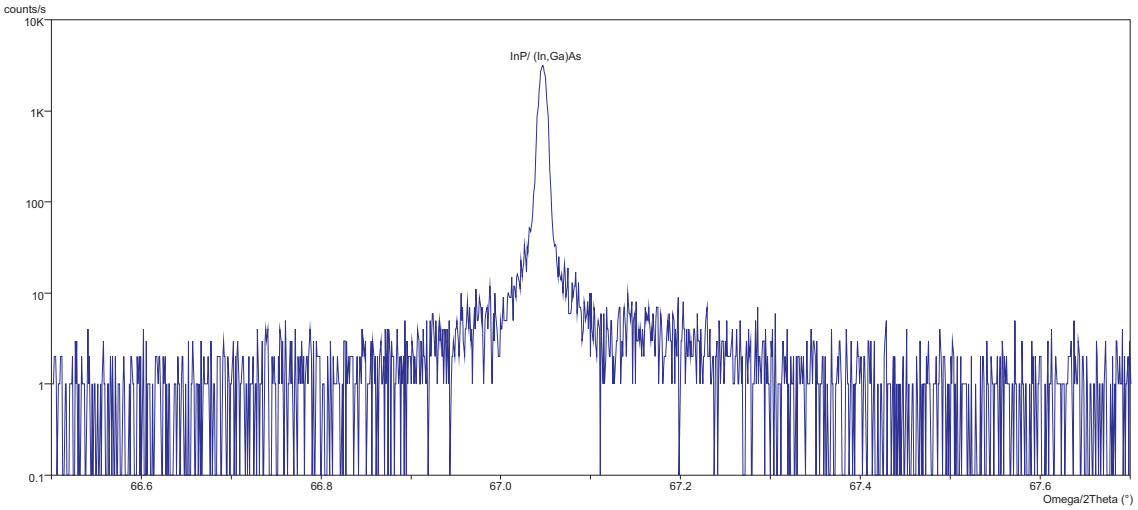

Figure 7.15.: HRXRD measurement of the (444) reflex of ≈ 180nm thick undoped (In,Ga)As layer on InP(111)B. The buffer is lattice-matched to the substrate.

would be assigned to the (In,Ga)As layer, leads to the result that the buffer layer is successfully grown strained on the substrate. By looking more accurate at the scan one

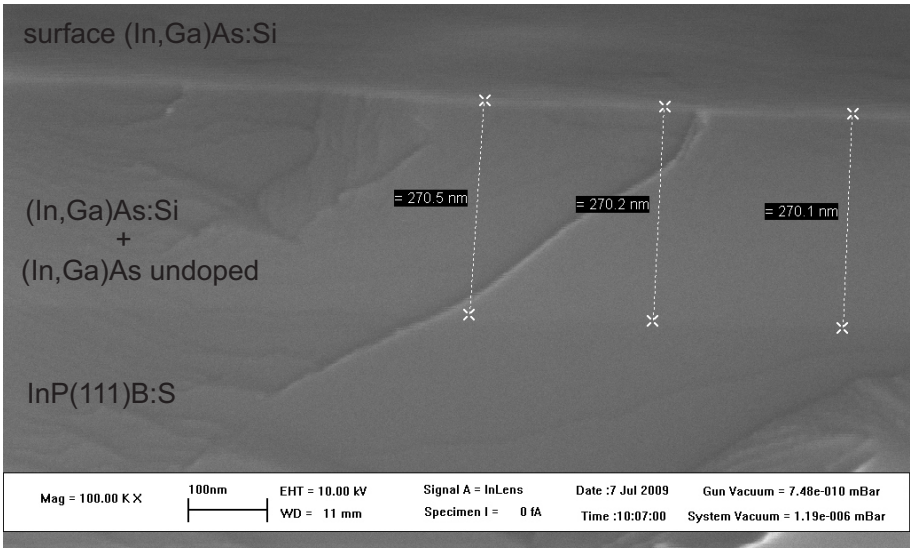

Figure 7.16.: Side view of a sample consisting of 170nm undoped (In,Ga)As/ 100nm n-doped (In,Ga)As on InP(111)B imaged with SEM.

can identify also some weak thickness fringes to the left and right of the main peak. This is a hint that the interfaces are not only rough but also flat parts are present.
When doping the buffer layer with Si, no change in the XRD scan is expected. Fig.7.16 shows a SEM side view photo of a sample consisting of InP(111)B:S substrate, 170nm undoped (In,Ga)As and 100nm n-doped (In,Ga)As layers. It can be clearly seen where the substrates ends and the buffer layer starts.
With SEM photos we are able to determine the growth rate of our (In,Ga)As layers on

(111) oriented layers, because with the weak thickness fringes from the XRD data no determination is possible. Indeed this approach is not absolutely accurate but the received values are good evidence of the growth rate magnitude. An additional information can be extracted form Fig.7.16. The three marked thickness values 270.5nm, 270.2nm and 270.1nm show the homogeneity thickness distribution of the grown layer. Of course only in the error bars of the SEM and the used software.

NiMnSb

NiMnSb is grown on InP(111)B substrates with an (In,Ga)As buffer layer. Fig.7.17 shows the HRXRD scan from the (222) reflex of a 5nm NiMnSb layer on ≈ 180nm undoped (In,Ga)As/InP(111)B substrate. At $\omega = 26.05°$ the InP peak is visible with a lattice matched (In,Ga)As layer. Right and left from the substrate peak thickness

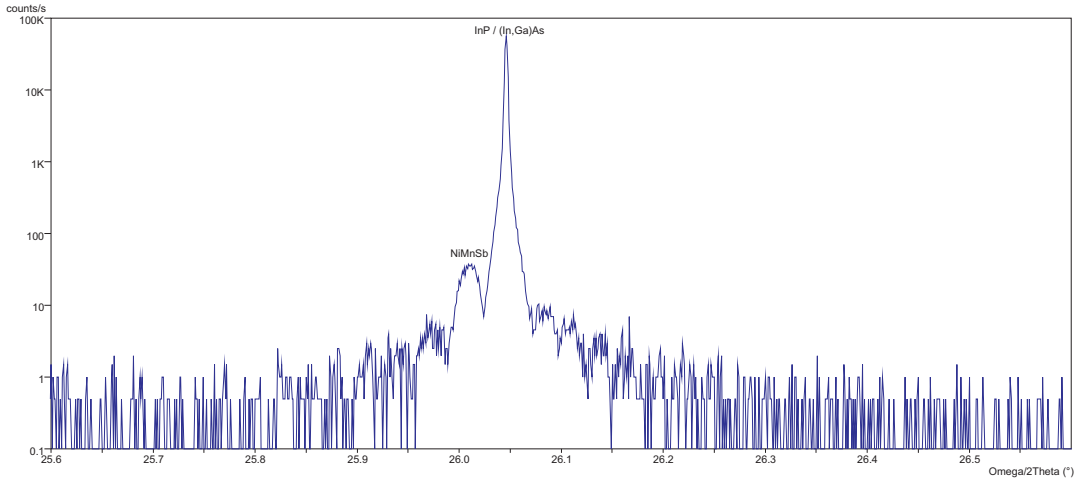

Figure 7.17.: HRXRD measurement of the (222) reflex of 5nm thick NiMnSb layer on ≈ 180nm thick undoped (In,Ga)As layer on InP(111)B. The buffer is lattice-matched to the substrate.

fringes from the buffer layer are visible at e.g. $\omega = 26.09°$, 26.11°, 25.97°, 25.94°. Also a clear peak from NiMnSb can be identified at $\omega = 26.01°$. The intensity of only 37 counts is owed to the small thickness of the half-Heusler layer. Again with *Bragg's law* and Eq. (4.9) we can calculate the vertical lattice constant analog to section 7.1.1. to $a_{vertical} = 6.017$Å. Caused by the low intensity count of the NiMnSb peak, it is hardly to determine the exact angle and accordingly the calculated value is not exact as well. Inside the error bars the determined value is still in good agreement with the value found in literature [Cas55].
An interesting aspect becomes visible if a (111)B sample is investigated with an ***A****tomic* ***F****orce* ***M****icroscope* (AFM). Fig.7.18 shows grown NiMnSb layers on undoped (In,Ga)As / InP(111)B with thickness of 10nm, 20nm and 40nm. In every AFM picture a clear equilateral triangle can be seen. All triangles a tilted towards the surface exposing a (111) plane. Fig.7.19 shows the depth of the triangle Z over the length X. With Z and X the angle of slope to the surface can be calculated. The highest angle of slope with a

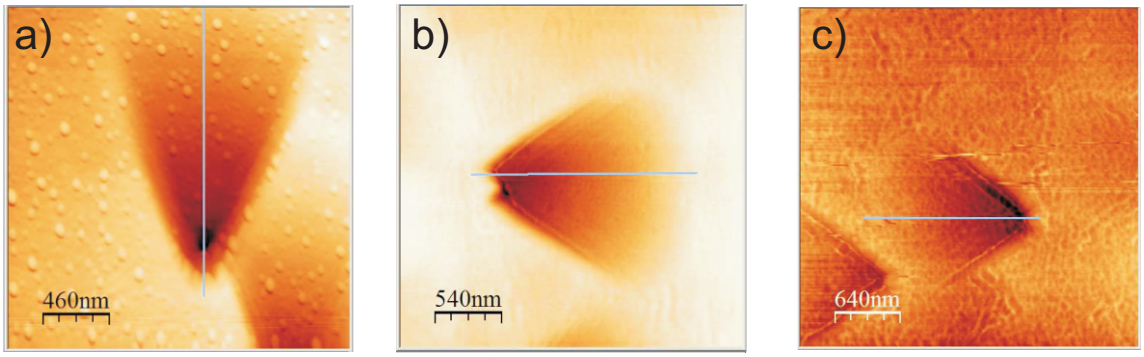

Figure 7.18.: AFM measurements of NiMnSb on InP(111)B substrate with (In,Ga)As buffer layer. a) corresponds to 10nm, b) to 20nm and c) to 40nm NiMnSb layer thickness. For all pictures the AFM was used in non-contact mode. The line in all three pictures is from the calculation software for determining the depth of the triangles (see Fig.7.19).

value of 1.5° is measured in Fig.7.19 a) corresponding to a NiMnSb thickness of 10nm. b) has a tilt of 1.37° and c) a value of 0.74°. These results mean that the angle of slope decreases with increasing thickness of the NiMnSb layer. Also they show that these defects are deeper than the NiMnSb layer and therefore originate from the buffer layer. Another conclusion we can draw is that the growth rates on the various surfaces are like

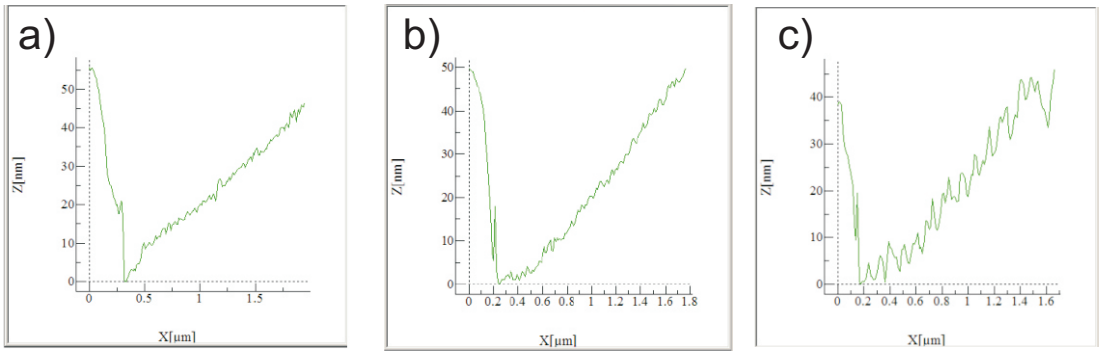

Figure 7.19.: Depth profiles measured with AFM of the three samples. a) 10nm, b) 20nm and c) 40nm NiMnSb on (In,Ga)As on InP(111)B.

the size of the observed defects. The depth of the defects decreases during the growth of NiMnSb and they will be completely closed when a layer thickness of approximately 60nm is reached. Fig.7.20 shows a SEM picture of the sample with 20nm NiMnSb. The triangle defects are distributed randomly over the complete sample. But they are all aligned in the same direction. These defects play an important role for the magnetic properties as explained in section 7.2.3.

7.2.2. Electrical properties

The electrical characterization of the doped and undoped layers are done with ETCH-CV. While for the measurements in a cryostat Hall-Bars have to be processed by chemical

Figure 7.20.: SEM picture from the sample with 20nm NiMnSb. The triangle defects are distributed randomly over the sample but all aligned in the same direction.

wet etching, this is not necessary for measurements with a ETCH-CV. ETCH-CV measures the capacity of the depletion layer from (In,Ga)As in dependence from a voltage. From this measured data the carrier concentration can be calculated. This technique uses the difference in electron affinity when the semiconductor is in contact with a different material. As a contact material we use an electrolyte solution which creates a

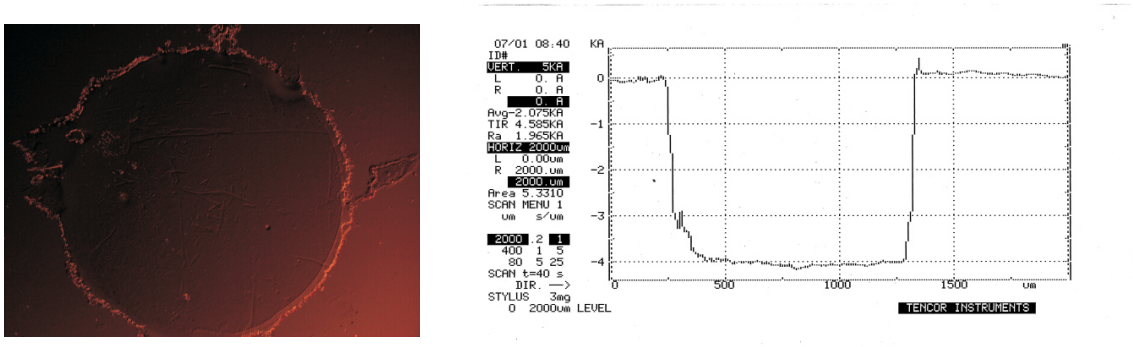

Figure 7.21.: *Left:* Nomarski picture of the etched hole caused by the ETCH-CV measurement. *Right:* Alpha step data. The depth and diameter of the etched hole is measured.

Schottky contact between the electrolyte and the (In,Ga)As. When applying a current to this solution it starts to etch the semiconductor. The measurement are done with a Biorad PN4300 Semiconductor Profiler. As the electrolyte solution $Na_2OH + Na_2SO_3$ is used. This method is destructive. The Biorad PN4300 etches a hole in the sample with a diameter of about 1mm. In Fig.7.21(*left*) a Nomarski photo of the etched hole is presented and in Fig.7.21(*right*) the depth profile measurement of this hole. The depth profile was measured with an Alpha Step from Tencor Instruments. The ground

of the hole is the substrate, outside is the surface of the doped (In,Ga)As. The etch depth is about 400nm and the diameter of the hole 1.1mm as seen in the depth profile (Fig.7.21). Fig.7.22 shows the carrier concentration over etch depth obtained by the ETCH-CV measurement. The three different layers are marked. From 0 to ≈ 100nm the (In,Ga)As:Si layer is etched with a maximum carrier concentration $n = 6 \cdot 10^{17} \frac{1}{cm^2}$ followed by an undoped (In,Ga)As layer from 100nm to ≈ 270nm with a minimum carrier concentration $n = 1 \cdot 10^{17} \frac{1}{cm^2}$. In depths higher than 270nm the InP(111)B:S substrate is present with a carrier concentration $n = 7 \cdot 10^{18} \frac{1}{cm^2}$.

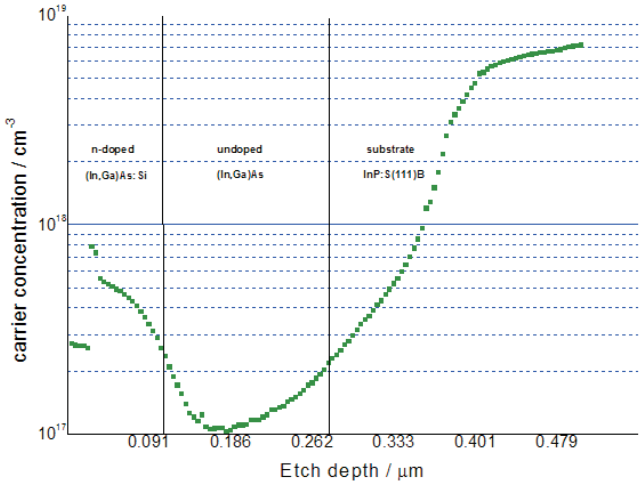

Figure 7.22.: Etch-CV measurement of a 100nm thick (In,Ga)As layer doped with Si followed by a 180nm thick undoped (In,Ga)As layer on InP(111)B substrate.

7.2.3. Magnetic properties

For investigating the magnetic properties of NiMnSb layers on (111) oriented substrates FMR measurements are performed again. During all measurements an external field is swept from 700 Oe to 2000 Oe and applied in-plane. A modulation field with 49 kHz modulation frequency is applied additionally.
The sample is mounted on a 360° rotating holder. At 0° the external field is along $[2\overline{1}\overline{1}]$ direction, at 60° along $[11\overline{2}]$, at 120° along $[1\overline{2}1]$ and at 180° parallel $[\overline{2}11]$. Sketch

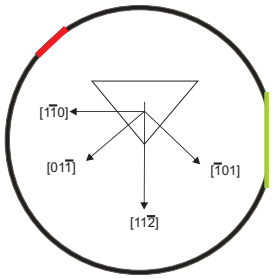

Figure 7.23.: Crystal directions and orientation of the triangle defect on a InP(111) wafer.

in Fig.7.23 shows the crystal directions and the orientation of the triangle defect on a InP(111) wafer. The orientation of the minor flat (red) and the major flat (green) can be found in appendix A.1. The high-frequency field has a frequency of 10.386GHz while rotating the magnetic field. For all three layers we receive a different anisotropy

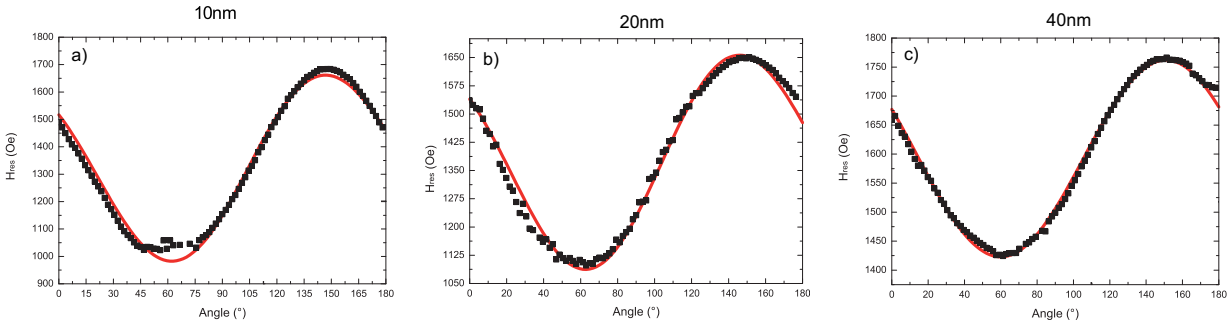

Figure 7.24.: Angle dependency of the resonance field for a) 10nm, b) 20nm and c) 40nm thick NiMnSb grown on InP(111)B. All layers show a pronounced uniaxial anisotropy behaviour. With increasing NiMnSb layer thickness the anisotropy field decreases.

strength. The anisotropy field decreases while the layer thickness increases (Fig.7.25). In every measurement the easy axis has a lower resonance field than the hard axis. The easy axis is at an angle of 60° while the hard axis is at 150°. The observed FMR spectrum is surprising because theory predicts a threefold symmetry in plane instead of the observed uniaxial anisotropy. One possible explanation is the presence of another symmetry breaking. This is provided by the miscut of the substrate resulting in a regular pattern of steps terraces as already explained in chapter 6.1 and its importance for a good quality of the grown layers. From the FMR measurements we also see that the anisotropy axis is aligned in the direction of the miscut. This observation suggests that the miscut is the origin of the uniaxial anisotropy. The defects discussed in the previous subsection are strongly anisotropic and the fact that their size decreases with increasing layer thickness suggests that triangle defects are causing the magnetic anisotropy we have measured. As a conclusion, with a defined miscut we are able to have control of

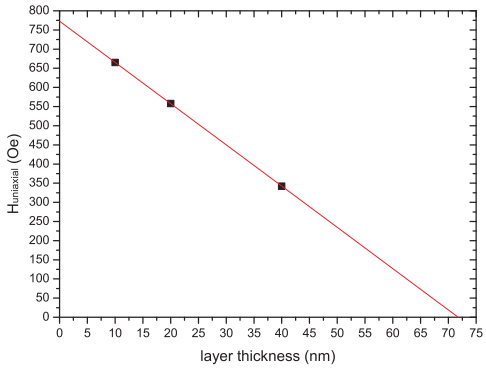

Figure 7.25.: Decreasing anisotropy field during increasing NiMnSb layer thickness on InP(111)B/(In,Ga)As.

the anisotropy in a NiMnSb layer. This might be interesting for future NiMnSb based spintronic devices.

8. Investigation of the 80K anomaly

In chapter 2 we discussed a possible present phase transition from a half-metallic ferromagnet to a normal ferromagnet in NiMnSb at 80K. Based on the results from our structural and magnetic characterization measurements, we investigate a 40nm thick NiMnSb layer. For our experiment we use a cryostat which can be adjusted in a temperature range between 4.2K and 293K in 1K steps.
The sample is grown with our best growth parameters shown in chapter 5. In Fig.8.1 the grown heterostructure is diagrammed. To investigate the behaviour at 80K you have to measure the normal Hall coefficient, the anomalous Hall coefficient and the Hall resistivity. If the Hall coefficient and the anomalous Hall term increase in temperatures under 80K, it is a hint for a phase transition [Hor00]. In the Hall resistivity measurement from [Hor00], see Fig.2.10 (*left*), the Hall resistivity follows the T^2 law between 4.2K and 80K and $T^{1.35}$ in higher temperatures up to room temperature. The authors say that ρ_{xy} follows the T^2 law if a half metal is measured and $T^{1.35}$ for a normal ferromagnet. To check the behaviour around 80K in our NiMnSb film, we need a cryostat to get all wanted temperatures and we have to process a structure with a Hall geometry on the layer. The process of structuring a so-called Hall-Bar on NiMnSb is the topic of the following chapter. It is described in detail how the process looks like and which steps and chemicals are needed for successfully creating a Hall-Bar on NiMnSb. The cryostat measurements with the processed sample are shown in chapter 8.2. There is also a short overview about the measurement geometry and the set-up.

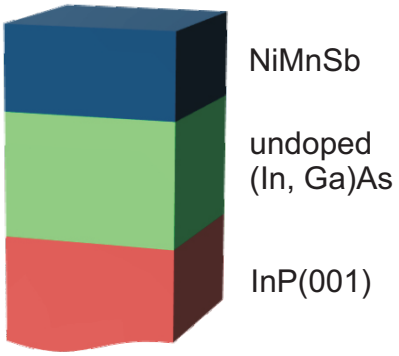

Figure 8.1.: Grown heterostructure for investigation of the 80K anomaly.

8.1. Hall-Bar processing

The processing of a Hall-Bar on NiMnSb is based on two major points of lithography. The used techniques are optical lithography and chemical wet etching. The used wavelength by optical lithography is in the range $\lambda = 200 - 400nm$. The transfer from the mask to the layer/resist occurs in contact printing meaning that there is a physical contact between the mask and the resist(Fig.8.2). With that transfer technique the critical dimension CD that can be printed is roughly

$$CD = \sqrt{\lambda g} \tag{8.1}$$

with λ being the wavelength of the radiation source and g being the gap between mask and the layer including the thickness of the resist. For our process we are using the photo resist ARU-4040. To get the resist on top of the sample we spin coat it for 40s at 5000 rounds per minute, resulting in a thickness of approximately 1300nm. With a mercury lamp as a source of radiation we have a spectral line wavelength $\lambda_{Hg} = 436nm$.

With 8.1 we get a value of 753nm for the critical dimension. In the next step the sample is baked out for 15min at 90°C on a hot plate under atmospheric pressure before we expose for 40s the mask with the contacts on the resist. After that we can do our first development with the developer $300 - 26 : Di = 4 : 1$. We dip the sample in the developer for 40s. Now we deposit a gold layer on top. For this step we use an external metallisation chamber in our clean room, not the metallisation chamber from our MBE cluster (Fig.4.5). To achieve a good sticking of Au on the sample we first deposit a 10nm thick Ti layer before producing the 100nm thick Au layer. Au is needed for our contacts. To get rid of the dispensable Au we make the lift-off for about 5min in acetone. Now the six Au contacts are ready. Next step is the Hall-Bar by itself. We start again with the photo resist ARU-4040, spin coated for 40s at 5000rpm. Then again we bake out the sample for 15min at 90°C under atmospheric pressure on a hot plate and expose the mask/sample for 30s. To reverse the lithography process we bake out again the sample for 10min at 105°C. Afterwards we expose without a mask for 25s. Now the unexposed parts of the resist will be removed when dipping the sample in the developer $300 - 26 = 1 : 2$ for 60s. Etching is done with the dilution $H_3PO_4 : H_2O_2 : H_2O = 3 : 1 : 50$ for 90s. With acetone we remove the remaining resist before we glue the sample in a chip carrier. This is done with the glue *Thermal Vanish* for 3min at 90°C on a hot-plate. Before we can start to measure with a cryostat we have to connect the contacts from the Hall-Bar with the contacts of the chip carrier. With an UV-Bonder we can connect all contacts we need with a small gold wire. The complete processed sample is shown in Fig.8.3. This sample can now be used in our cryostat.

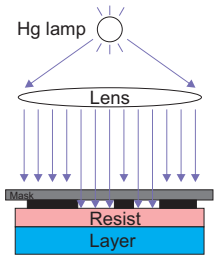

Figure 8.2.: Principle contact printing.

8.2. Temperature dependent measurements on NiMnSb

The Hall measurements are done in a simple bath cryostat working with He_4 to reach a temperature of 4.2K. The measurement principle of a Hall measurement is shown in Fig.8.4. The gold contact marked in pink is contact number 1. This dyed contact is only for illustration to find the correct contact number in the lower diagram of Fig.8.4. The magnetic field is generated by two coils inside the cryostat. A special feature of this cryostat is the possibility to set temperatures between 4.2K and room temperature. The displayed temperature by the cryostat (ITC) is not the real temperature. The conversion between the displayed temperature and the real temperature can be found in appendix C (C.1). In the following graphics the ITC values are used. A theoretical description of

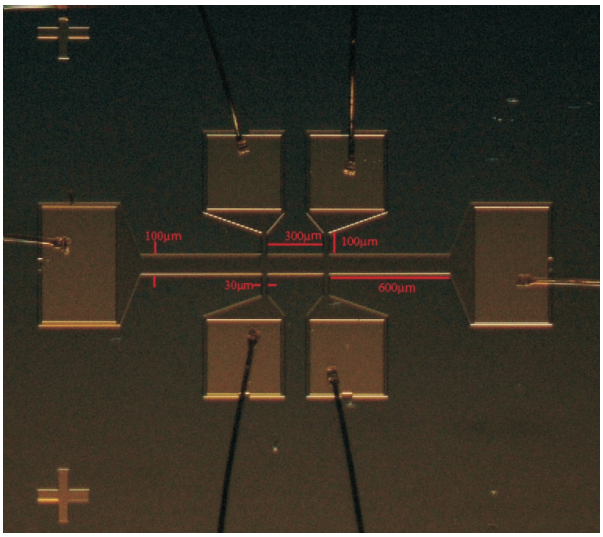

Figure 8.3.: Processed Micro-Hall-Bar with six contacts on NiMnSb/(In,Ga)As/InP(001) viewed with a Nomarski microscope.

the Hall effect can be found in many solid state physics books e.g. [Kit01] or [Iba02]. We apply a current I from contact 1 to 6, a magnetic field $\vec{B}$ perpendicular to I and measure voltages

- parallel to the current = U_{xx} (contacts 3 and 5)
- perpendicular to the current = U_{xy} (contacts 4 and 5)

U_{xy} is known as the Hall voltage U_H. With the measured voltages we can calculate the two resistors R_{xx} and R_{xy} with Ohms law to:

$$R = \frac{U}{I} \tag{8.2}$$

We arranged measurements in the temperature range between 4.2K and 293K divided into 22 steps. For every temperature step the magnetic field is driven from 0 to 5000mT. The resulting Hall resistor over magnetic field curve is shown in Fig.8.5. The cause for the negative values of R_{xy} between 0mT and 200mT is a longitudinal pickup. The longitudinal resistance of the measured sample is about 15Ω and the offset is about 0.01Ω. This circumstance means that if the Hall leads are slightly miss-aligned, so that they are not exactly opposite to each other, e.g. one of them is $\frac{1}{1000}$ of the length of the bar shifted compared to the other, than this can happen because this kind of miss-alignment is usually in the lithographic error. In addition to Hall you also measure a tiny part of the longitudinal resistance R_{xx}, which can be negative or positive depending on which direction the leads are offset.
From our data we followed the analysis of [Hor00] and calculated the Hall coefficient R_H and the anomalous Hall term $R_H M_S$ like explained in [McA79] and plotted them over

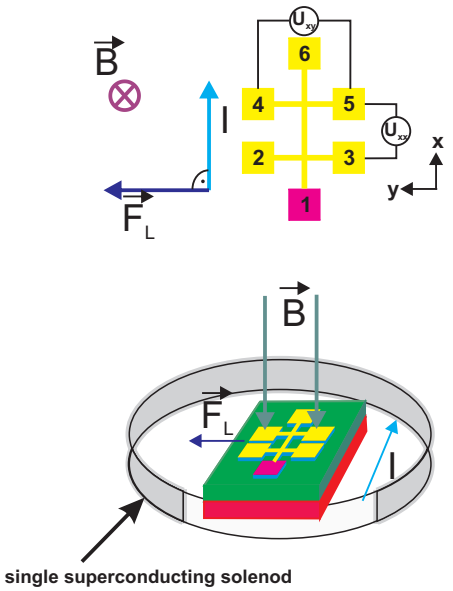

Figure 8.4.: Assembly of a bath cryostat. The magnetic field is generated by single superconducting solenoid inside the cryostat. Directions of I, $\vec{B}, \vec{F_L}$ are drawn. In the upper part the processed Hall-Bar is diagrammed with all connections for the measurements. The pink dyed contact is only for orientation reason.

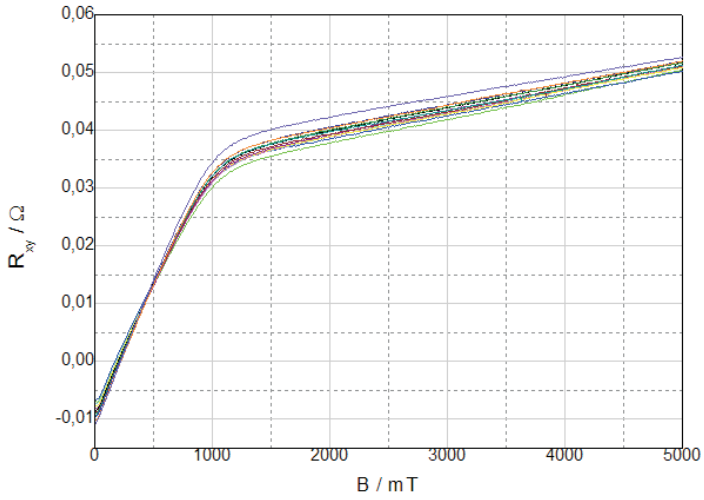

Figure 8.5.: From Hall measurements calculated R_{xy} over applied magnetic field for different temperatures.

temperature. Fig.8.6(*left*)shows the developing of the Hall coefficient with increasing temperature. Compared with Fig.2.10 (*right* / •) we see almost the same behaviour for

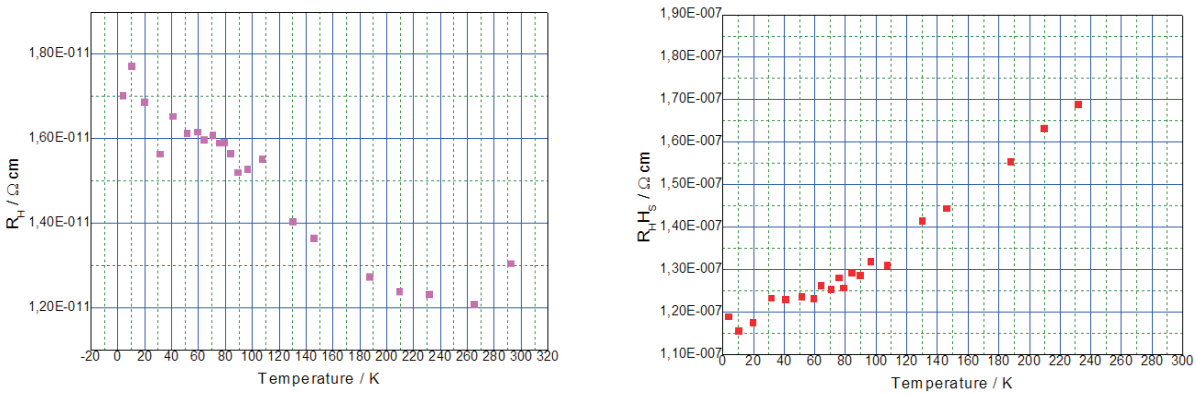

Figure 8.6.: *Left:* From Hall measurements calculated Hall coefficent R_H over temperature.
Right: From Hall measurements calculated anomalous Hall term $R_H H_S$ over temperature.

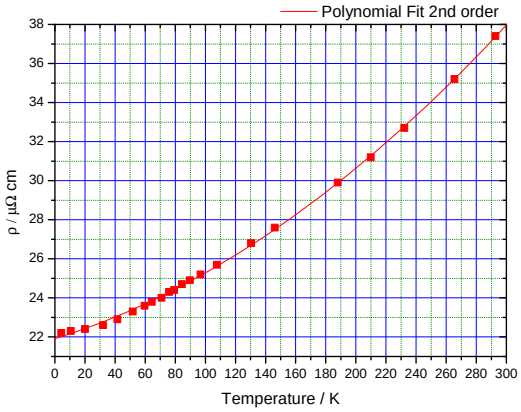

Figure 8.7.: From Hall measurements calculated resistivity over temperature.

the ordinary Hall coefficient between 4.2K and 293K. But in our case the data points are following one line and in [Hor00] they are following two lines, one between 4.2K up to 80K and one between 80K and 293K. The slope of the first part is much higher than the second part while the slope of our Hall coefficient is in the magnitude of the the second part.
In Fig.8.6(*right*) we also see a different behaviour in the developing of the anomalous Hall term compared to Fig.2.10 (*right* / ☒). In our case we do not see an upturn of the anomalous Hall coefficient in the range between 4.2K and 80K.
Fig.8.7 shows the Hall resistivity ρ plotted over temperature. The red fit line from a 2nd order polynomial fit is also shown in the graphic. With our sample we see that ρ_{xy} not follows $T^{1.35}$ in the range between 80K - 300K, indicated by the polynomial fit.
With the different behaviour in R_H, $R_H M_S$ and ρ_{xy} compared to [Hor00] it is possible that we have grown NiMnSb with the property of a half-metallic ferromagnet at room temperature.

9. NiMnSb based devices

9.1. GMR effect in a NiMnSb based device

Our first built device uses a quantum-mechanics effect namely the GMR effect[1]. This effect is already utilized in conventional hard drive discs as the read head [Tan94].

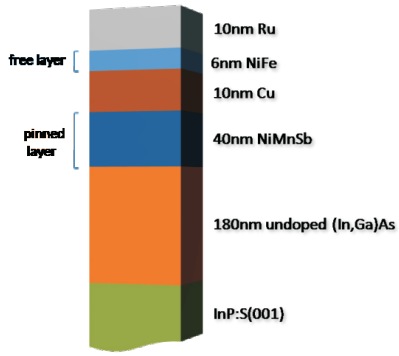

Figure 9.1.: GMR-STO Stack.

This magnetoresistance effect is caused by spin dependent scattering of the electrons at two magnetic electrodes [Bai88]. This circumstance leads to the assumption that a high spin-polarization in the electrodes will dramatically increase the GMR effect [Val93]. That makes NiMnSb a perfect candidate for such a device due to its properties characterized in chapter 2, especially the theoretical 100% spin-polarization and the far above room temperature Curie temperature T_C= 728K. In addition as a consequence of the ultra low damping of our NiMnSb layers (see chapter 7.1.2), we should be able to realise a spin valve GMR-device with a weaker magnetic field and lower power consumption because the magnetization of the layer can be switched much more easily. E. Girgis *et al.* already realised a NiMnSb based GMR device with CoFe and NiMnSb as the magnetic electrodes and Cu as the spacer [Gir05]. With their used CIP geometry they received a CIP-GMR of 3.5% at room temperature. Fig.9.1 shows the sample structure we have processed. The substrate is a conducting InP(001) wafer doped with S. Beside the substrate, the buffer layer (In,Ga)As is conducting as well, followed by the half-metallic ferromagnet NiMnSb. After completing the MBE grown parts the sample is transferred under UHV conditions into the sputter chamber (see Fig.4.5) where Cu, Py[2] and Ru are deposited with DC sputtering. The two electrodes in this GMR sample are Py and NiMnSb. The measurements are done in a 4 point needle probe station setup at room temperature with current I=10mA and the magnetic field parallel to the easy axis of the magnetic electrodes. In CPP geometry the magnetic field is swept from -375mT to +375mT and backwards. The voltage drop over the sample is measured and from that value the resistance change is calculated. The received magneto-resistance curve is shown in Fig.9.2. The Magneto-Resistance-Ratio is 3.4%. When sweeping the magnetic field from -375mT to +375mT (red curve) first the NiMnSb layer switches his in-plane magnetization and a high resistance is present. Afterwards the Py layer switches and the resistance becomes small again. That later

[1]Nobel prize for Grünberg und Fert 2008
[2]Py = Permalloy = 80% Ni + 20% Fe

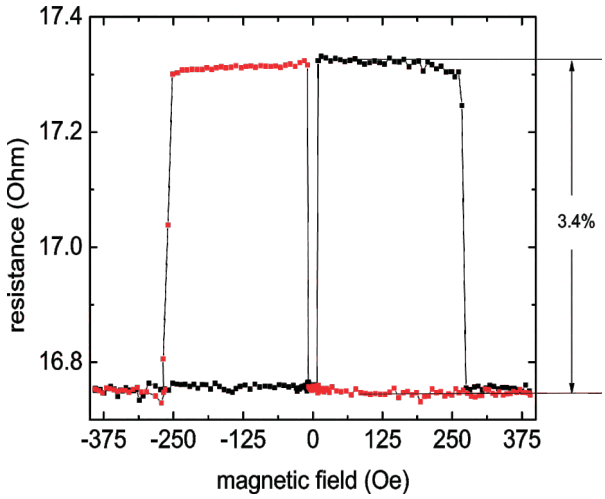

Figure 9.2.: GMR effect measured in CPP geometry. The resistance over the applied magnetic field is plotted. The GMR ratio is 3.4%.

switching is a result of the higher coercive field of Py.
A similar technique has been already tried out using the similar magneto-resistance effect TMR [Loc06]. In this device both electrodes consists of NiMnSb and the antiferromagnet NiMn was deposited on the top electrode to get an exchange bias effect on this layer.
When sweeping backwards again (black curve) the NiMnSb layer first switches the magnetization direction and afterwards the Py layer. The measured CPP-GMR ratio up to 3.4% at room temperature shows that the theoretical 100% spin-polarization from NiMnSb is not present in NiMnSb in (001) orientation at room temperature. This result shows the necessity for growing NiMnSb on (111) oriented substrates to achieve higher GMR ratios. But nevertheless NiMnSb is a promising candidate for future GMR devices.

9.2. Spin Torque Oscillator based on NiMnSb

A spin-polarized current and its resulting spin torque has the possibility to either switch the magnetic formation or to generate high frequency signals in the GHz range in a spin valve [Slo96],[Ber96]. For the presented measurements the same stack as for the spin valve GMR measurements is used, see Fig.9.1.
From that layer sequence elliptical pillars are defined with dimensions long axis $a = 200nm$, short axis $b = 100nm$ and height $h = 66nm$. That means the pillar ends where the buffer layer (In,Ga)As starts. Due to the fact that this buffer layer is conducting, an isolator, namely Si_3N_4, has to be deposited as the next step. The easy axis of the uniaxial anistropy NiMnSb fixed layer is arranged perpendicular to the easy axis of the free NiFe layer. The magnetic layers are in antiparallel state when the measurements starts. The measurement setup is diagrammed in Fig.9.4. The emitting frequency is measured in the connected spectrum analyser HP8560E. For combination of the dc[3] and rf[4] signals a biasT with a bandwidth of 40GHz is used.
In this measurement the current is sent from the fixed NiMnSb layer through the Cu spacer into the free NiFe layer.

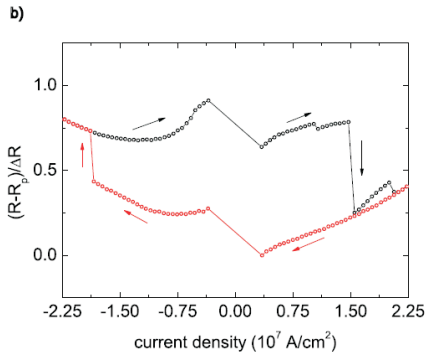

Figure 9.3.: Symmetrical switching of the processed pillar by certain current densities. The resistance normalized to the absolute change over the current density is plotted.

With the created spin transfer torque we are able to switch the magnetization of the free layer at certain current densities. The processed pillar shows an almost symmetrical switching (Fig.9.3). At a current density of $1.47 \cdot 10^7 \frac{A}{cm^2}$ the free layer switches its magnetization parallel to the fixed NiMnSb layer and at $-1.84 \cdot 10^7 \frac{A}{cm^2}$ back to the antiparallel state of the device. Our built STO generates different frequencies for different applied currents. Fig.9.5a shows the different output spectra resulting from the applied currents. From all presented spectra in Fig.9.5 a reference spectrum is subtracted. This reference spectrum is the frequency spectrum measured at our sample without any applied current. Fig.9.5 shows the emitted high frequency spectra for different currents. It is clear visible that different currents shift the emitted frequency. Fig.9.6 presents the determined q-factors and emitted frequencies over the applied current of our STO. The q-

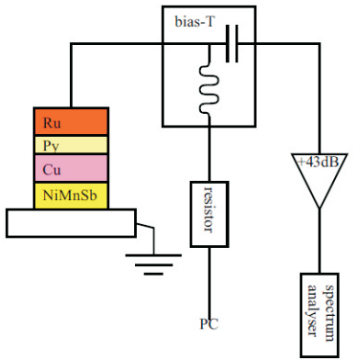

Figure 9.4.: Experimental setup for measuring the STO sample.

[3] ***d**irect **current***
[4] ***r**adio **f**requency*

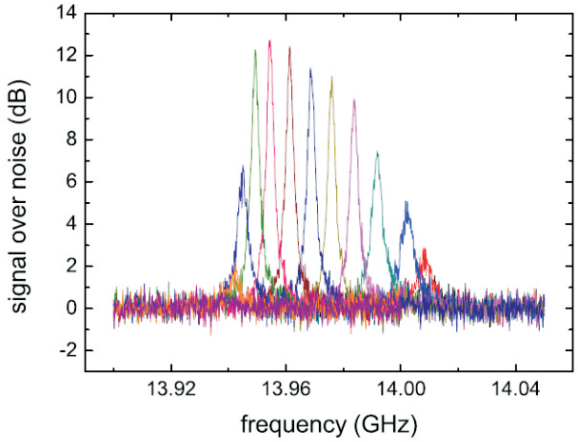

Figure 9.5.: Emitted high frequency spectra for different currents. From [Rie10].

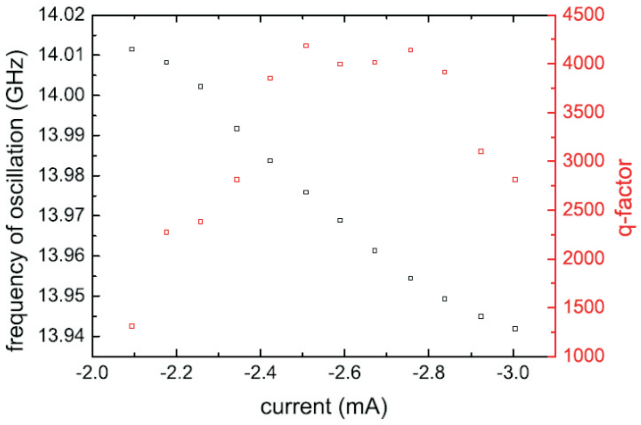

Figure 9.6.: Emitted high frequency and achieved q-factors over applied current. From [Rie10].

factor is defined as:

$$Q = \frac{f}{\Delta f} \tag{9.1}$$

With a current I = -2.51mA and an emitted frequency f = 13.976GHz we receive a q-factor of 4180. This is the highest Q factor reported so far for a STO. Compared to [Dev07] this is a factor of $\approx 15x$ higher. Again all results are achieved without any external applied field. This makes such a STO a very good candidate for a future application for high frequency devices compared with low power consumption e.g. cell phones.
A more detailed description of the fabrication process and the measurement setup can be found here [Rie10], [Rie2].

9.3. Frequency-controlled magnetic vortex memory

The following section describes the work done in corporation between Service de Physique de l'*É*tat Condensé and Experimentelle Physik 3 during the EU project DynaMax[5]. The results have been published by B. Pigeau *et al.*[Pig10].
In modern times technology is looking for different approaches of realising a non-volatile random access memory. The main aims are very low power consumption and small size of these devices, which can be achieved. One approach uses magnetic nano-objects where, with their bistable properties, binary information can be stored. A major problem is to find a performant mechanism to reverse the magnetization inside such an individual cell [Sch03].
By using a low dissipation material like NiMnSb, a magnetic nano-object can take advantage of the high dynamical susceptibility at his ferromagnetic resonance frequency. Experiments by B. Van Waeyenberge *et al.*[Wae06] and K. Yamada *et al.* [Yam07] have

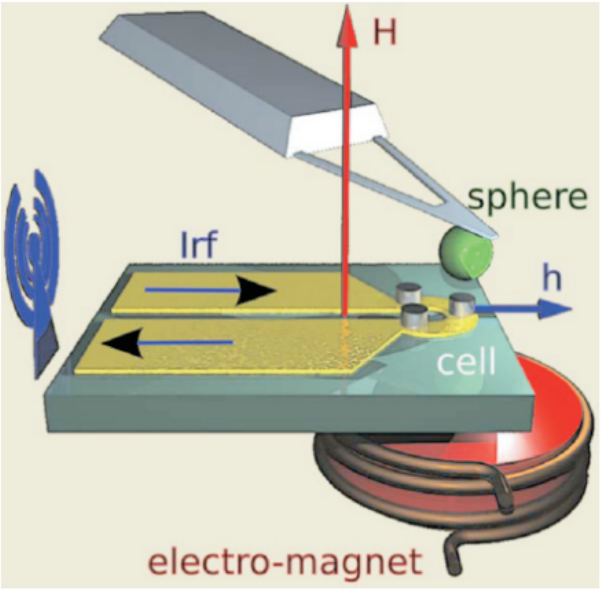

Figure 9.7.: The setup of a frequency-controlled magnetic memory. The memory elements are vortex-state NiMnSb disk of 44nm thickness and 1 μm diameter. From [Pig10].

shown that the core polarity in such a so-called vortex-state magnetic nano dot [Gus08] can be reversed in zero magnetic field through the excitation of the gyrotropic rotation of the vortex core about its equilibrium position. B. Pigeau *et al.* used NiMnSb layers grown by Experimentelle Physik 3 at Würzburg university. In this work a frequency-controlled memory is demonstrated with resonance reading and writing schemes realized with NiMnSb nano dots with a magnetic bias field H perpendicular to the dot surface (Fig.9.7). The read and write mechanism is realised by an in-plane linearly polarized microwave magnetic field h. The local addressing is achieved by means of magnetic

[5]http://dynamax.tnw.utwente.nl/

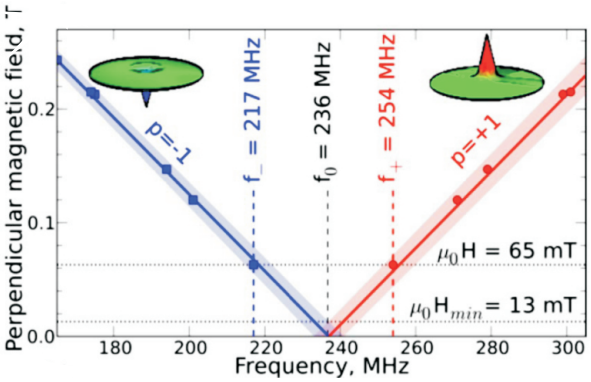

Figure 9.8.: Consequence of a static magnetic field H to the frequency at two different polarities p=+/- 1 of magnetic nano disc. From [Pig10].

resonance force microscope. The static magnetic field H introduces a controlled splitting of the frequency of the gyrotropic mode depending on the core polarity [Lou09]. Now it is possible to selectively address the polarity state of individual magnetic dots by controlling the frequency of a linear polarized microwave pulse excitation. In Fig.9.8 the consequence of the static magnetic field H for the frequencies of the two different polarities p=+/- 1 is shown.
This resulting frequency splitting is direct proportional to H:

$$f_+(H) - f_-(H) = 2f_0(H/H_S) \tag{9.2}$$

with H_S being the required magnetic field to saturate the NiMnSb dot along its normal and f_0 is the frequency of the gyrotropic mode at H=0.
NiMnSb is a very good choice for the magnetic nano dots. First of all, the static magnetic field H has to be chosen that Eq. (9.3) exceed the line width Δf of the gyrotropic mode, which can be expressed as:

$$\Delta f = \alpha_v f_0 . \alpha_v = \alpha[1 + ln(R/R_C)] \tag{9.3}$$

with α_v being the damping parameter for the gyrotropic mode [Gus06] and α being the dimensionless Gilbert damping constant of NiMnSb of the nano dot. The minimum for a perpendicular bias field is given by the following equation:

$$H_{min} = (\alpha_v/2)H_S \tag{9.4}$$

To minimize H, the nano dots material should have a low damping. A low damping increases the aspect ratio β [6], which leads to a decrease in the saturation field H_S. As a result a lower power consumption can be assumed for such a ***M**agnetoresistive **R**andom **A**ccess **M**emory* (MRAM) device. The parameters for the presented device are:

- $\alpha = 0.002$

[6] $\beta = t/R$, with t = thickness and R = radius of the dot

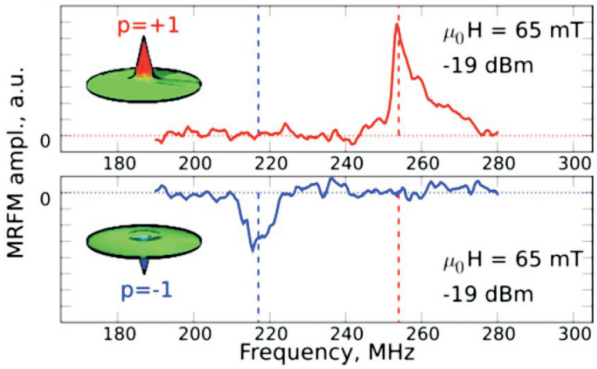

Figure 9.9.: Read process of a magnetic vortex memory. From [Pig10].

- $\mu_0 M_0 = 690\text{mT}$
- $T_C = 730\text{K}$
- $\beta = 0.1$ (t = 44nm, R = 500nm)
- separation between single dots = 10 μm
- saturation field $\mu_0 H_S = 800\text{mT}$

The dots are placed on a gold microwave strip-line which provides h. h couples to the gyrotropic rotation of the vortex core for both polarities due that h contains right and left circular components. By changing the frequency f of the microwave field h, it is possible to resonantly excite gyrotropic rotation of the vortex core in the magnetic dots. When applying a weak microwave field h, the amplitude of the gyrotropic rotation is small but enough to read the polarity when using the technique of ***M**agnetic **R**esonance **F**orce **M**icroscope* (MRFM) . A detailed description of a MRFM can be found here [Kle08]. On the other hand, if the microwave field h is large and the frequency f is the gyrotropic resonance frequency for a given core polarity, the velocity of the vortex core rotation reaches a point where the core polarity is reversed. This can be treated as a writing process. For the shown measurements a total static magnetic field $\mu_0 H = 65mT \approx 5\mu_0 H_{min}$ is used. With that value the magnetic dot has the gyrotropic frequencies $f_+ = 254MHz$, $f_- = 217MHz$ and $f_0 = 236MHz$. In addition the frequency line width Δf of the gyrotropic rotation in the dot is known. It is in the order of $\Delta f \approx 8MHz$. In Fig.9.9 is shown a measurement of the reading process of this frequency-controlled magnetic vortex memory by using a MRFM. While the weak reading microwave signal is varied in the interval containing f_+ and f_-, the amplitude of the MRFM cantilever oscillation is measured.
The writing process is shown in Fig.9.10. In 9.10a the writing frequency f_w of the strong writing pulses with τ_w=50ns and power $P_w \approx 100\mu W$ is illustrated. The weak reading signal frequency f_r of power $P_r \approx 10\mu W$ is shown in 9.10b. f_r is applied throughout the whole writing process but interrupted every second in order to apply a strong writing pulse. Again by measuring the amplitude of the MRFM cantilever oscillation, it is

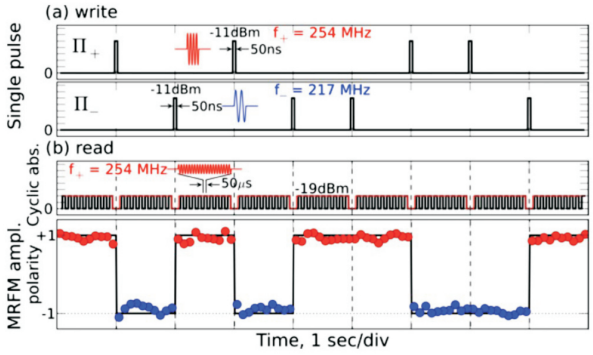

Figure 9.10.: Write process of a magnetic vortex memory. From [Pig10].

possible to read out the core polarity of the magnetic dots.
From 9.10 it is clear that with these parameters for writing the core polarity reversal is deterministic. In this experiment with this configuration, the reversal efficiency has been determined with a success rate above 99%. For developing a frequency-controlled magnetic memory the setup in 9.8 can be extended like diagrammed in Fig.9.11. To

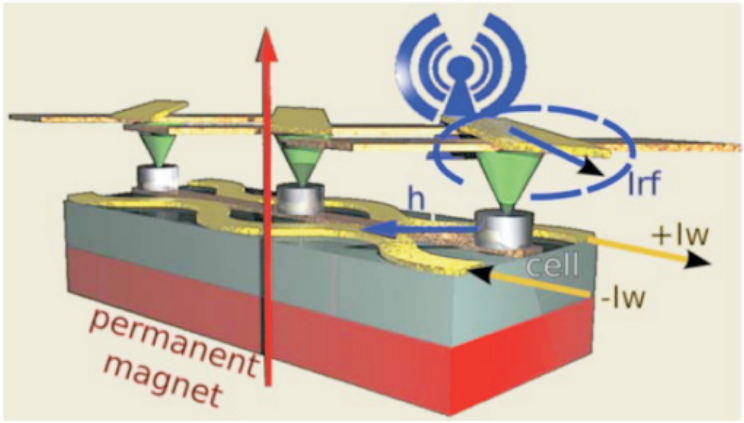

Figure 9.11.: Possible design of a complete magnetic vortex memory device. From [Pig10].

improve the functionality of this extended frequency-controlled magnetic memory, the following parameters should be adjusted. First of all β should be increased to 1 to reduce the dot saturation field H_s and accordingly the minimum perpendicular bias magnetic field to $\mu_0 H_{min} \approx 5mT$. As a result a static magnetic field of only 20mT would be sufficient. This can be realised by a small permanent magnet, meaning that there is no need of extra power for the static magnetic field.
An optimal control of the core polarity in the magnetic nano dot realised with an optimization of the microwave-pulse duration for switching the core polarity is described here [Pig11].

10. Outlook

We have shown that NiMnSb can be grown epitaxial with high magnetic and crystalline quality. With these layers some more promising experiments are possible.
First of all it would be useful to take advantage of the special feature of 100% spin-polarization in NiMnSb (chapter 2). All MBE pre-work has already been done when growing a n-doped (In,Ga)As layer on top of undoped (In,Ga)As/InP(111)B followed by NiMnSb. Also an e-beam process with dry-etching has been tried but without success. A new approach would be a wet-etch process based on the optical-lithography process used for our Hall-Bar in chapter 8. The sample structure of a future experiment is diagrammed in Fig.10.1. The procedure of this experiment can follow the setup used by

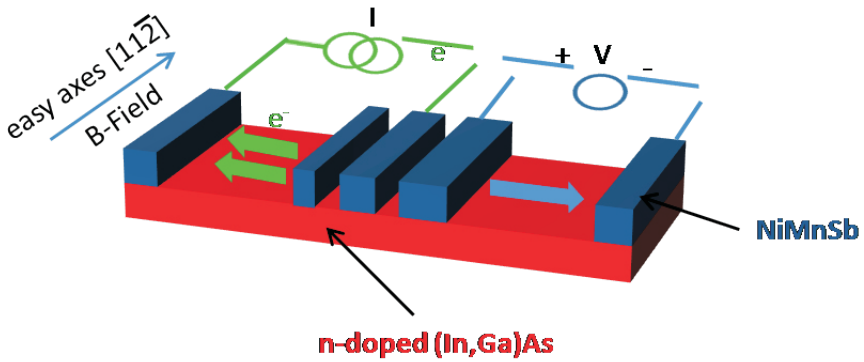

Figure 10.1.: Possible spin injection experiments with NiMnSb on n-doped (In,Ga)As InP(111)B.

Xiaohua Lou *et al.*[Lou07]. In their experiment they investigated a lateral ferromagnet-semiconductor device consisting of doped and undoped GaAa and Fe.
Another challenging topic would be to use the NiMnSb layers grown on InP(111)B for the basis of GMR devices. The high spin-polarization should raise the MR-ratio clearly. Our preliminary work has shown that there is the possibility of no phase transition in NiMnSb around 80K and we are able to grow NiMnSb on (111) oriented substrates.
Thirdly the relaxation behaviour should be investigated when using the new flux ratios. It should be possible to reach higher thickness for capped layers due to the higher crystalline quality of our layers grown with the new flux ratios. Different capping layers should be investigated as well and it should be checked if this would influence the relaxation behaviour.
Another device with NiMnSb would be a TMR stack on InP(111)B. TMR stacks have been already investigated at Experimentelle Physik 3, but these where also grown on InP(001) substrates. The advantage is that the necessary pinning layer could be grown in

one step with the second electrode of a TMR stack, because NiMn is an anti-ferromagnet and can be produced just by closing the shutter in front of the Sb effusion cell.
Also it would be promising to build a logic device based on the different damping behaviour of NiMnSb in different direction. The easy axis can be used as logical 1 and the hard axis as logical 0. Also because of the ultra low damping of our NiMnSb layers it should be possible to build a GMR device with very low external magnetic fields.
In addition to our achieved high Q-factor the emitted output power of the STO device should be raised. A possible device can be consist out of many connected STOs.

Summary

In this work the epitaxial growth and characterization of the half-metallic ferromagnet NiMnSb was presented. NiMnSb crystallizes in the $C1_b$ structure which is similar to the zinc blende structure from widely used III-V semiconductors. One special property of NiMnSb is the theoretical 100% spin-polarization at the Fermi edge. This makes it a perfect candidate for spintronic experiments and the material of choice for building novel spintronic devices. Another important topic in this work were the magnetic properties of NiMnSb, especially the low magnetic damping of the grown thin films.
All grown layers were fabricated with the technique of ***M**olecular **B**eam **E**pitaxy* (MBE). The layer stacks for all different experiments and devices were grown on InP substrate in (001) or (111)B orientation. Before the NiMnSb layer a buffer layer of undoped (In,Ga)As was grown to provide a flat surface for the growth start of NiMnSb. Additional for some samples on InP(111)B, a Si doped (In,Ga)As layer was grown on top of the undoped (In,Ga)As layer. The dopant concentration of this n-doped layer was determined by ETCH-CV. The n-doped (In,Ga)As had a doping concentration of $n = 6 \cdot 10^{17} \frac{1}{cm^2}$ and the undoped (In,Ga)As layer of $n = 1 \cdot 10^{17} \frac{1}{cm^2}$. For the now following NiMnSb layer, different flux ratios were used as in [Bac05]. All layers were investigated by structural and the NiMnSb layer additional by magnetic properties.
For the structural investigation the in-situ technique ***R**eflection **H**igh **E**nergy **E**lectron **D**iffraction* (RHEED) and ex-situ tool ***H**igh-**R**esolution **X**-**R**ay **D**iffraction* (HRXRD) were used. RHEED observations showed a good quality of the grown buffer and half-metallic ferromagnet layers on both orientations. These results were strengthened by the HRXRD measurement. The symmetrical reflex (004) showed that it is possible to grow a lattice-matched (In,Ga)As layer on InP(001) and InP(111)B with a good crystalline quality proofed by the visible thickness fringes. For NiMnSb again thickness fringes were visible indicating a good structural quality. Additional the vertical lattice constant could be determined. The received value of $a_{NiMnSb-vertical} = 5.925$Åfor NiMnSb on InP(001) is in good agreement to the value $a_{NiMnSb-Lit} = 5.903$Åfound in literature [Cas55]. For NiMnSb on InP(111)B a vertical lattice constant of $a_{NiMnSb-vertikal} = 6.017$Åcould be determined. The deviation from the value found in literature is caused by the small layer thickness and low intensity of the peak. Caused by this just an unexact determination of the diffraction angle is possible. But not only the vertical lattice constant also the horizontal lattice constant and the proof of pseudomorphical growth was investigated. To get access to this parameters a ***r**eciprocal **s**pace **m**ap* (RSM) of a (001) oriented sample was measured with HRXRD using the asymmetrical reflex (115). The horizontal lattice constant of the buffer and the half-metallic ferromagnet layer could be determined as the same of the substrate meaning that all three peaks were lying on one perpendicular line. For NiMnSb this conclusion is only valid up to a thickness of ≈40nm. To increase this

maximum thickness, NiMnSb samples were grown on InP(001) substrates and capped with Ti/Au layers. Afterwards a reciprocal space map of the (533) reflex was drawn with ***G**razing-**I**ncident **X**-**R**ay **D**iffraction* (GIXRD) at the synchrotron beamline BW2 of HASYLAB [Kum07]. It has been shown that the critical thickness is more than doubled by depositing a Ti/Au capping directly after growth of NiMnSb without breaking the ***u**ltra**h**igh **v**acuum* (UHV). Up to now the highest reached thickness is 81.3nm without any relaxed parts in the layer. This result showed that the relaxation of the NiMnSb layer occurs when the sample leaves the UHV.
The magnetic properties were determined with ***F**erro**m**agnet **R**esonance* (FMR) experiments and ***S**uperconducting **Qu**antum **I**nterference **D**evice* (SQUID) measurements. The received magnetic damping parameter α from a 40nm thick NiMnSb layer on InP(001) could be determined to $3.19e^{-3}$ along $[1\bar{1}0]$. This value is lower than from Permalloy and in the range of MBE grown Fe. The resulting line width of our NiMnSb layers on InP(001) is more than 4.88 times smaller than measured before [Hei04]. Another result is the direction dependence of the damping. It has been measured that the difference of the damping is changed by more than 42% when rotating the applied field by 45° from $[1\bar{1}0]$ to [100].
With SQUID we measured a saturation magnetization of a 40nm thick NiMnSb layer as $4\mu_B$. This value is in very good agreement with the saturation magnetization found in literature [Cas55],[Kab90].
NiMnSb layers on InP(111)B substrate where also measured with FMR with a surprising result. These layers not only showed a decreasing in the anisotropy field with increasing thickness but also an uniaxial anisotropy. This is surprising because theory predicts a threefold symmetry. This behaviour can be explained with defects on these samples. With an ***A**tomic **F**orce **M**icroscope* (AFM) triangle-like defects were measured. These defects originated from the buffer layer and influenced the magnetic properties.
Another part of this work is dedicated to the behaviour of NiMnSb at temperatures around 80K. Different publications already investigated NiMnSb at this temperature with the result that a phase transition takes place at this point from a half-metal ferromagnet to a normal ferromagnet. With our samples, no phase transition can be observed in the data of the Hall, anomalous Hall term and resistivity. This leads to the conclusion that NiMnSb still is a half-metallic ferromagnet at room temperature.
The last part of this work discusses different spintronic devices build with our NiMnSb layers. In a first device the magnetization acts on the current. This ***G**iant **M**agneto **R**esistance* (GMR) device consisted of InP:S(001) - 180nm undoped (In,Ga)As - 40nm NiMnSb - 10nm Cu - 6nm NiFe - 10nm Ru in ***c**urrent **p**erpendicular to **p**lane* (CPP) geometry. GMR effect measurements were performed at room temperature. We received a Magneto-Resistance-Ratio of 3.4%.
In a second device the current acts on the magnetization and makes use of the spin torque phenomena. This so called ***S**pin **T**orque **O**scillator* (STO) emitted frequencies in the GHz range (13.94GHz - 14.1GHz) and the Q-factor could be determined as 4180 which is 15 times higher than in [Dev07]. At current densities of $1.47 \cdot 10^7 \frac{A}{cm^2}$ and $-1.84 \cdot 10^7 \frac{A}{cm^2}$ the switching of the electrodes magnetization could be detected.
The last fabricated device is based on the magnetic vortex phenomena. For switching

the core polarity the gyrotropic frequencies $f_+ = 254MHz$ $f_- = 217MHz$ and a total static magnetic field of only $mu_0H = 65mT$ were necessary. The reversal efficiency has been determined as better than 99% [Lou09]. This frequency controlled magnetic vortex memory is the first step towards building a small-sized memory device without the use of a power-supplied static magnetic field. Such a device will be only controlled by a frequency and a small permanent magnet.

Zusammenfassung

In dieser Dissertation wurde das epitaktische Wachstum und die Charakterisierung des halb-metallischen Ferromagneten NiMnSb vorgestellt. NiMnSb kristallisiert in der $C1_b$ Kristallstruktur, welche ähnlich der Zinkblendestruktur von häufig verwendeten III-V Halbleitern ist. Eine besondere Eigenschaft von NiMnSb ist die theoretische 100% Spinpolarisation an der Fermikante, die es zu einem perfekten Kandidaten für Spintronikexperimente macht. Desweiteren ist das Material NiMnSb erste Wahl für neuartige Spintronikanwendungen. Eine weitere große Rolle für diese Arbeit spielten die magnetischen Eigenschaften von NiMnSb, insbesondere die niedrige magnetische Dämpfung der abgeschiedenen Schichten.
Alle gewachsenen Schichten wurden mit der Molekularstrahl-Epitaxie Technick (MBE[1]) hergestellt. Die Schichtstapel für alle unterschiedlichen Experiemente und Anwendungen wurden auf InP Substrate in (001) oder (111)B Orientierung abgeschieden. Vor der NiMnSb Schicht wurde eine undotierte (In,Ga)As Pufferschicht gewachsen, um eine glatte Oberfläche für das Wachstum für NiMnSb bereitzustellen. Für einige Proben auf InP(111)B wurde zusätzlich eine Si-dotierte (In,Ga)As-Schicht auf die undotierte (In,Ga)As-Schicht gewachsen. Die Dotierungskonzentration der n-dotierenten Schicht wurde per ETCH-CV bestimmt. Die n-dotierte (In,Ga)As-Schicht hatte ein Dotierungskonzentration von $n = 6 \cdot 10^{17} \frac{1}{cm^2}$ und die undotierte (In,Ga)As-Schicht von $n = 1 \cdot 10^{17} \frac{1}{cm^2}$. Für die nun folgenden NiMnSb-Schichten wurden abweichende Flussverhältnisse verwendet, wie in [Bac05] beschrieben. Alle Schichten wurden auf strukturelle Eigenschaften und die NiMnSb-Schichten zusätzlich auf magnetische Eigenschaften untersucht.
Für die strukturellen Untersuchungen wurde die in-situ Technik RHEED[2] und das exsitu Werkzeug der hochauflösenden Röntgenbeugung (HRXRD) verwendet. Auf beiden Orientierungen zeigten die RHEED-Beobachtungen eine gute Qualität der gewachsenen Puffer- und halb-metallischen Ferromagnetschichten. Dieses Ergebnis wurde durch die HRXRD-Messungen bestärkt. Die Röntgenbeugungsmessungen zeigten ebenfalls, dass es möglich ist, eine auf InP gitterangepasste (In,Ga)As-Schicht mit guter Qualität zu wachsen, was durch die sichtbaren Schichtdickenoszillationen bestätigt wurde. Für NiMnSb waren ebenfalls Schichtdickenoszillationen sichtbar, welche eine gute strukturelle Qualität anzeigen. Zusätzlich konnte die vertikale Gitterkonstante bestimmt werden. Der erhaltene Wert von NiMnSb auf InP(001) $a_{NiMnSb-vertikal} = 5.925$Åist in guter Übereinstimmung mit dem Literaturwert $a_{NiMnSb-Lit} = 5.903$Å[Cas55]. Für NiMnSb auf InP(111)B wurde eine vertikale Gitterkonstante von $a_{NiMnSb-vertikal} = 6.017$Åbestimmt.

[1] vom englischen ***M**olecular **B**eam **E**pitaxy*
[2] von der englischen Bezeichnung: ***R**eflection **H**igh **E**nergy **E**letron **D**iffraction*

Die Abweichung zum Literaturwert ist eine Folge der geringen Schichtdicke und der geringen Peakintensität. Hierdurch ist die Bestimmung des Beugungswinkels nicht exakt möglich. Aber nicht nur die vertikale Gitterkonstante, ebenso die horizontale Gitterkonstante und der Beweis eines pseudomorphen Wachstums wurden untersucht. Um Zugriff auf die Parameter zu bekommen, wurde eine reziproke Gitterkarte mit dem asymmetrischen Reflex (115) mit HRXRD gemessen. Die horizontale Gitterkonstante des Puffers und des halb-metallischen Ferromagneten konnte in guter Übereinstimmung mit der Substratgitterkonstante bestimmt werden. Dies bedeutet, dass alle drei Peaks auf einer senkrechten Linie liegen. Allerdings ist dieses Ergebnis ausschließlich bis zu einer Schichtdicke von ≈40nm für NiMnSb gültig. Um diese maximale Schichtdicke zu erhöhen, wurden NiMnSb auf InP(001) Substrate gewachsen und mit einer Ti/Au-Schicht als Schutz versehen. Mit diesen Proben wurden reziproke Gitterkarten des (533) Reflex mit streifender Einfalls - Röntgenbeugung (GIXRD) am Synchrotron BW2 des HASYLAB gemessen [Kum07]. Es hat sich gezeigt, dass sich die kritische Schichtdicke mehr als verdopppeln lässt, wenn eine Ti/Au- Schicht direkt nach dem Wachstum von NiMnSb abgeschieden wird, ohne das ***U**ltra**h**och**v**akuum* (UHV) zu verlassen. Die höchste bis jetzt erreichte kritische Schichtdicke liegt bei 81.3nm. Bis zu diesem Punkt sind keine relaxierten Teile in der Schicht entstanden. Dieses Ergebnis zeigt auch, dass das Relaxieren von NiMnSb erst auftritt, wenn die Probe das UHV verlässt.
Die magnetischen Eigenschaften wurden mit ***F**erromagnet **R**esonanz* (FMR) Experimenten und einem superleitenden Quanteninterferenz Messsystems (SQUID[3]) bestimmt. Der gemessene magnetische Dämpfungsparameter α einer 40nm dicken NiMnSb Schicht auf InP(001) wurde zu $3.19e^{-3}$ entlang $[1\bar{1}0]$ bestimmt. Dieser Wert ist niedriger als von Permalloy und in der Größenordnung von MBE gewachsenen Fe. Die resultierende Linienbreite von unseren Schichten auf InP(001) ist mehr als 4.88 mal kleiner als bei [Hei04] gemessen. Ein weiteres Ergebnis ist die Richtungsabhängigkeit der Dämpfung. Es wurde gemessen, dass die Dämpfung sich um mehr als 42% ändert, wenn das angelegte Feld um 45° von $[1\bar{1}0]$ nach [100] gedreht wird.
Mit SQUID messten wir die Sättigungsmagnetisierung von einer 40nm dicken NiMnSb-Schicht zu $4\mu_B$. Dieser Wert ist in sehr guter Übereinstimmung mit dem Literaturwert der Sättigungsmagnetisierung [Cas55],[Kab90].
NiMnSb-Schichten auf InP(111)B Substrate wurden ebenfalls mit FMR untersucht, mit einem überraschenden Ergebnis. Diese Schichten zeigten nicht nur eine Abnahme im Anisotropiefeld mit ansteigender Schichtdicke, sondern auch ein uniaxiales Anistropieverhalten. Das ist überraschend, weil die Theorie eine dreifache Anisotropie voraussagt. Dieses Verhalten kann mit Defekten in diesen Proben erklärt werden. Mit einem Rasterkraftmikroskop (AFM[4])wurden dreieckige Defekte gemessen. Diese Defekte haben ihren Ursprung in der Pufferschicht und beeinflussen die magnetischen Eigenschaften.
Ein weiterer Teil dieser Arbeit widmete sich dem Verhalten von NiMnSb bei Temperaturen um die 80K. Verschiedene Veröffentlichungen haben bereits NiMnSb bei dieser Temperatur untersucht, mit dem Ergebnis, dass an diesem Punkt ein Phasenübergang

[3] **S**uper conducting **Qu**antum **I**nterference **D**evice)
[4] **A**tomic **F**orce **M**icroscope

von einem halb-metallischen Ferromagneten zu einem normalen Ferromagneten stattfindet. In unserer Probe konnte solch ein Phasenübergang in den Messdaten des normalen Hall Koeffizienten, anomalen Hall-Term und Leitungswiderstand nicht beobachtet werden. Dies führt zu der Folgerung, dass NiMnSb immer noch ein halb-metallischer Ferromagnet bei Raumtemperatur ist.
Der letzte Teil dieser Arbeit behandelt verschiedene Spintronikanwendungen, welche aus unseren NiMnSb-Schichten gebaut wurden. In einer ersten Anwendung agiert die Magnetisierung auf einen Strom I. Die so genannte GMR[5]-Anwendung besteht aus InP:S(001) - 180nm undotierten (In,Ga)As - 40nm NiMnSb - 10nm Cu - 6nm NiFe - 10nm Ru in CPP Geomtrie[6]. Die GMR-Effekt Messungen wurden bei Raumtemperatur durchgeführt. Wir erhielten ein MR-Verhältnis von 3.4%.
In einer zweiten Anwendung agiert der Strom I auf die Magnetisierung und nutzt dabei das Phänomen des Spin-Drehmomentes aus. Dieser so genannte ***S**pin **T**orque **O**scillator* (STO) emittiert Frequenzen im GHz Bereich (13.94GHz - 14.1GHz) und der Q-Faktor wurde zu 4173 bestimmt, welcher mehr als 20mal höher ist als in [Dev07]. Bei Stromdichten von $1.47 \cdot 10^7 \frac{A}{cm^2}$ und $-1.84 \cdot 10^7 \frac{A}{cm^2}$ konnte ein Umschalten der Magnetisierung der Elektroden detektiert werden.
Die letzte hergestellte Anwendung basiert auf dem magnetischen Wirbelphänomen. Für das Umschalten der Kernpolarität sind die gyrotropischen Frequenzen $f_+ = 254MHz$ $f_- = 217MHz$ und ein totales, statisches magnetisches Feld von nur $mu_0H = 65mT$ nötig. Die Umkehreffizienz wurde besser als 99% bestimmt. Dieser frequenzkontrollierte magnetische Wirbel-Speicher ist der erste Schritt zur Herstellung von stark verkleinerten Speicheranwendungen, welche ohne ein statisches magnetisches Feld auskommen. Die Ansteuerung erfolgt alleine über die eingekoppelte Frequenz.

[5] ***G**iant **M**agneto **R**esistance*
[6] ***c**urrent **p**erpendicular to **p**lane*

A. Materials data and constants

A.1. Wafer map InP(001)

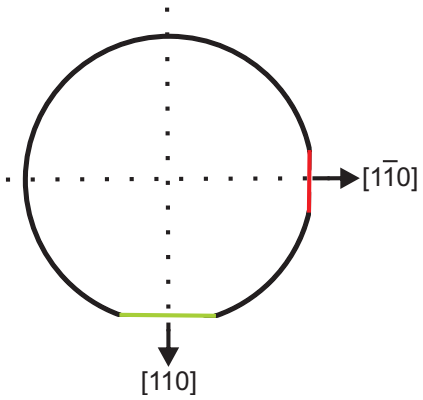

Figure A.1.: Wafer map of our used InP(001) samples. The crystal directions are marked. The minor flat is dyed red and the major flat is dyed green.

A.2. Wafer map InP(111)

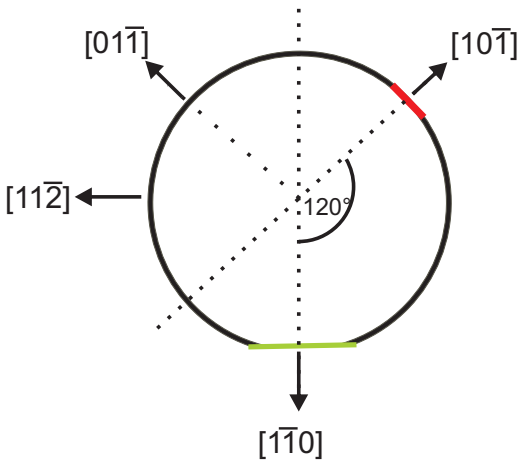

Figure A.2.: Wafer map of our used InP(111) samples. The crystal directions are marked. The minor flat is dyed red and the major flat is dyed green.

A.3. Lattice constants

Material	a_0 **[Å]**
InP	5.868
$GaAs$	5.653
$NiMnSb$	5.903
Ni_2MnSb	6.002

Table A.1.: Important lattice constants a_0 of materials used or discussed in this work.

B. Hall-Bar processing recipes

B.1. Recipe for Hall-Bars on NiMnSb

- Clean sample : Dip in acetone, then in isopropanol and last in distilled water (DI)
- Photoresist ARU-4040 on sample with spin coater (40s@5000rpm)
- Bake-out for 15min@90°C on hot plate
- Exposure for 20s with mask "Hall-Bar negative"
- Developing 40s in Developer 300-26:DI=1:4
- Evaporating 10nm Ti + 100nm Au
- Lift-off in acetone
- Photoresist ARU-4040 on sample with spin coater (40s@5000rpm)
- Bake-out for 15min@90°C
- Exposure for 30s with mask "Hall-Bar negative"
- Bake-out 600s@1005°C on hot plate
- Exposure for 25s
- Developing 60s in Developer 300-26:DI=1:2
- Etching NiMnSb : 90s with $H_3PO_4 : H_2O_2 : H_2O = 3 : 1 : 50$
- Remove resist in acetone
- Glue sample in chip carrier with Glue Thermal Vanish for 180s@90°C on hot plate
- Bond the sample

B.2. Recipe for Hall-Bars on (In,Ga)As

- Clean sample : Dip in acetone, then in isopropanol and last in distilled water (DI)
- Photoresist ARU-4040 on sample with spin coater (40s@5000rpm)
- Bake-out for 15min@90°C
- Exposure for 20s with mask "Hall-Bar negative"
- Developing 35s in Developer 300-26:DI=1:4
- Evaporating 10nm Ti + 100nm Au
- Lift-off in acetone
- Photoresist ARU-4040 on sample with spin coater (40s@5000rpm)
- Bake-out for 15min@90°C
- Exposure for 30s with mask "Hall-Bar positive"
- Bake-out 600s@1005°C on hot plate
- Exposure for 25s
- Developing 60s in Developer 300-26:DI=1:2
- Etching : Citron acid : $H_2O_2 = 1:1$ etching rate = $1\frac{nm}{sec}$ at (In,Ga)As
- Remove resist in acetone
- Glue sample in chip carrier with Glue Thermal Vanish for 180s@90°C on hot plate
- Bond the sample

B.3. Hall-Bar mask

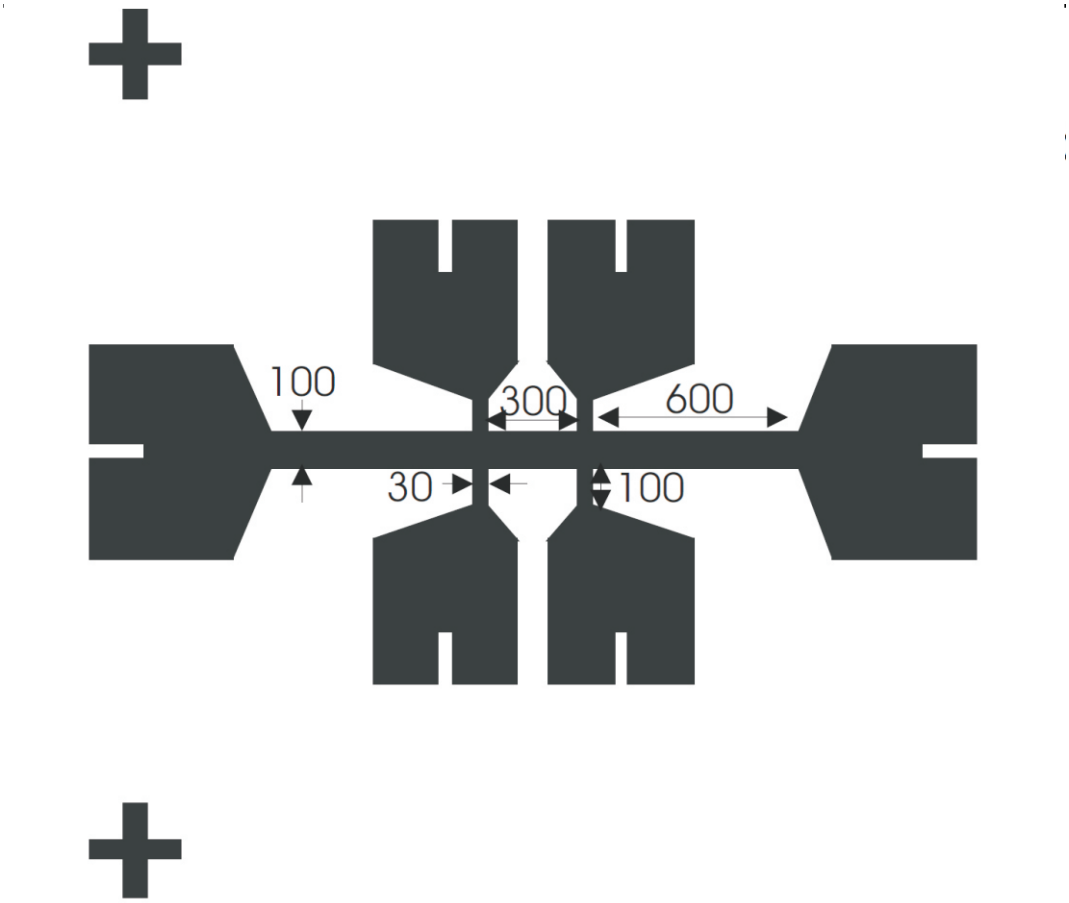

Figure B.1.: Used Hall-Bar mask with length and width in μm.

C. Temperature conversion table

In following table the reader can find the conversion between the temperature displayed by the cryostat (ITC) and the real present temperature during cool down.

ITC / K	real temperature / K
173	292.8
160	265.6
145	232.3
135	210.0
125	188.0
105	146.2
97	130.4
85	107.7
79	96.8
75	89.7
72	84.5
69	79.3
67	75.9
64	70.9
60	64.4
57	59.6
52	51.8
45	41.5
38	32.0
28	20.0
18	10.6
4.2	4.2

Table C.1.: Conversion table for ITC value from cryostat to real present temperature during cool down.

Bibliography

[Bac03] P. Bach *et al.*, Appl. Phys. Lett. **83**, 521 (2003)

[Bac05] P. Bach *Growth and Characterization of NiMnSb-based Heterostructures* Ph. D. thesis, university Würzburg

[Bar48] J. Bardeen, W.H. Brattain and W. Shockley, Phys. Rev. **74**, 230 (1948)

[Zin90] J. Barnas, A. Fuss, R.E. Carnley, P. Grünberg and W. Zinn, Phys. Rev. **B** 42, 8110 (1990)

[Ber96] L. Berger, Phys. Rev. B. **54**, 9353 (1996)

[Bai88] M. N. Baibich, J. M. Broto, A. Fert *et al.*, Phys. Rev. Lett. **61**, 2472 (1988)

[Bos88] S.S. Bose *et al.*, J. Appl. Phys. **63**, 743 (1988)

[Cas55] L. Castelliz.,Z. Metallkd. **46**, 201 (1955)

[Dev07] T. Devolder *et al.*, J. Appl. Phys. **101**, 063916 (2007)

[Eic07] Ch. EIckhoff, H. Kolev, M. Donath, G. Rangelov and L. F. Chi, Phys. Rev. B **76**, 205440 (2007)

[Fei89] R. Feidenhans'l, Surf. Sci. Rep. **10**, 105 (1989)

[Gil55] T. L. Gilbert, Phys. Rev. **100**, 1243 (1955)

[Gir05] E. Girgis, P.Bach, C. Rüster, C. Gould, G. Schmidt, and L. W. Molenkamp , Appl. Phys. Lett. **86**, 142503 (2005)

[Gro83] R.A. de Groot and F.M. Mueller, Phys. Rev. Lett. **50**, 2024 (1983)

[Gru86] P. Grünberg *et al.*, Phys. Rev. Lett. **57**, 2442 (1986)

[Gus06] K. Y. Guslienko, Appl. Phys. Lett. **89**, 022510 (2006)

[Gus08] K.Y. Guslienko, J. Nanosci. Nanotechnol. **8**, 2745 (2008)

[Hei04] B. Heinrich*et al.*, J. Appl. Phys. **95**, 7462 (2004)

[Her89] M.A. Herman and H. Sitter. *Molecular Beam Epitaxy, Fundamentals and Current Status, Springer Series in Materials Science* Volume 7, Springer-Verlag Berlin Heidelberg 1989

[Heu03] F. Heusler, Verh. Deutsche Physikalsiche Gesellschaft, **5**, 219ff, (1903)

[Hor96] C. Hordequin, J. Pierre, R. Currat, J. Magn. Magn. Mat. **162**, 75-84 (1996)

[Hor00] C. Hordequin, D. Ristou, L. Ranno, and J. Pierre, R. Currat, Eur. Phys. J. B **B**, 287-293 (2000)

[Hor00] C. Hordequin, D. Ristoiu, L. Ranno and J. Pierre, Eur. Phys. J. **B** 16, 287-293 (2000)

[Iba02] H. Ibach, H. Lüth *Festkörperphysik - Einführung in die Grundlagen*, volume 6, chapter 12, Springer-Verlag Berlin, 2002

[Kab90] R. Kabani, M. Terada, A. Roshko, J.S. Moodera, J. Appl. Phys. **67** (9), 4898 (1990)

[Kal06] S. S. Kalarickal, P. Krivosik, M. Z. Wu, C. E. Patton, M. L. Schneider, P. Kabos, T. J. Silva and J. P. Nibarger, J. Appl. Phys. **99** (9), 093909 (2006)

[Kob09] K. Kobayashi, N. Inaba, N. Fujita, Y. Sudo, T. Tanaka, M. Ohtake, M. Futamoto and F. Kirino, IEEE Transactions on Magnetics **45**, (6), 2541 (2009)

[Kil76] Jack S. Kilby, IEEE Transactions on Electron Devices **23**, 648 (1976)

[Kit01] C. Kittel *Einführung in die Festkörperphysik*

[Kle08] O. Klein, G. de Loubens, V.V. Naletov *et al.*, Phys. Rev. B **78**, 144410 (2008)

[Kum07] C. Kumpf *et al.*, Phys. Stat. Sol. (c) **4**, No.9, 3150-3160 (2007)

[Loc06] F. Lochner. Wachstum und Charakterisierung von NiMnSb-basierenden TMR-Heterostrukturen, Master's thesis, University of Würzburg (2006)

[Lou07] Xiaohua Lou *et al.*, Nat. Phys. **3**, 197 (2007)

[Lou09] G. de Loubens, A. Riegler, B. Pigeau *et al.*, Phys. Rev. Lett. **120**, 177602 (2009)

[McA79] S.P.McAlister and C.M. Hurd, J. Appl. Phys. **50**, 7526 (1979)

[Moo94] J. S. Moodera and D. M. Mootoo, J. Appl. Phys. **76**(10), 6101 (1994)

[Moo65] Gordon Moore, Electrons **38**, (1965)

[Nex11] http://thenextwavefutures.wordpress.com/2009/08/02/the-end-of-moores-law/, April 21th 2011

[Ott01] M.J. Otto, R.A.M. van Woerden, P.J. van der Valk, J. Wijngaard, C.F. van Bruggen, C. Haas and K.H.J. Buschow, J. Phys.: Condens. Matter **1**, 2341-2350 (1989)

[Ott02] M.J. Otto, R.A.M. van Woerden, P.J. van der Valk, J. Wijngaard, C.F. van Bruggen and C. Haas, J. Phys.: Condens. Matter **1**, 2351-2360 (1989)

[Pal69] P.W. Palmberg *et al.*, Appl. Phys. Lett. **15**, 254 (1969)

[Pig10] B. Pigeau, G. de Loubens, O. Klein, A. Riegler, F. Lochner, G. Schmidt, L.W. Molenkamp, V.S. Tiberkevich and A.N. Slavin, Appl. Phys. Lett. **96**, 132506-1 (2010)

[Pig11] B. Pigeau, G. de Loubens, O. Klein, A. Riegler, F. Lochner, G. Schmidt and L.W. Molenkamp, Nat. Phys. **7**, 26 (2011)

[Ral02] D. C. Ralph, M. D. Stiles, J. Magn. Magn. Mat. **320**, 1190 (2008)

[Rat93] C. Ratsch and A. Zangwill, Appl. Phys. Lett. **63**, 2348 (1993)

[Rie10] Andreas Riegler. *Ph D thesis: Ferromagnetic resonance study of the Half-Heusler alloy NiMnSb, 2011*

[Rie2] A. Riegler *et al.*, *Very high quality factor for spin torque oscillator in zero field*, in progress

[Ris00] D. Ristoiu, J.P. Nozieres, L. Ranno, J. Magn. Magn. Mat. **219**, 97 (2000)

[Roy00] W. van Roy, J. De Boeck, B. Brijs, G. Borghs, Appl. Phys. Lett. **77**, 4190 (2000)

[Roy02] W. van Roy, G. Borghs, J. De Boeck, J. Magn. Magn. Mat. **242-245**, 489 (2002)

[Roy01] W. van Roy *et al.*, J. Cryst. Growth **227-228**, 862 (2001)

[Sch03] H.W. Schumacher, C. Chappert, R.C. Sousa *et al.*, Phys. Rev. Lett. **90**, 017204 (2003)

[Seg73] A. Segmüller and A. E. Blakeslee, J. Appl. Crys. **6**, 19 (1973)

[Slo96] J. C. Slonczewski, J. Magn. Magn. Mat. **159**, L1 (1996)

[Tan94] C. Tang, R. Fontana, T. Lin *et al.*, IEEE Trans. Magn. **30**, 3801 (1994)

[Tse02] Y. Tserkovnyak *et al.*, Phys. Rev. Lett. **88**, 117601-1 (2002)

[Urb01] R. Urban, G. Woltersdorf and B. Heinrich, Phys. Rev. Lett. **87**, (21) 217204 (2001)

[Tun05] http://www.imec.be/tunamos/public/index.html, April 21th 2011

[Val93] T. Valet and A. Fert , Phys. Rev. **B**, 7099 (1993)

[Veg21] L. Vegard, Zeit f. Physik **5**, 17 (1921)

[Vli97] E. Vlieg, J. Appl. Crystallogr. **30**, 532 (1997)

[Wae06] B. Van Waeyenberge, A. Puzic, H. Stoll *et al.*, Phys. Rev. Lett. Nature (London) **444**, 461 (2006)

[Wij01] G.A. de Wijs and R.A. de Groot, Phys. Rev. **64**, 020402 (2001)

[Yam07] K. Yamada, S. Kasai, Y. Nakatani *et al.*, Phys. Rev. Lett. Nature Mater. **6**, 270 (2007)

Publications

B. Pigeau, G. de Loubens, O. Klein, A. Riegler, F. Lochner, G. Schmidt and L. W. Molenkamp
Optimal control of vortex-core polarity by resonant microwave pluses
Nat. Phys. **7**, 26 (2011)

B. Pigeau, G. de Loubens, O. Klein, A. Riegler, F. Lochner, G. Schmidt, L. W. Molenkamp, V.S. Tiberkevich and A. N. Slavin
A frequency-controlled magnetic vortex memory
Appl. Phys. Lett. **96**, 132506 (2010)

G. de Loubens, A. Riegler, B. Pigeau, F. Lochner, F. Boust, K. Y. Guslienko, H. Hurdequint, L. W. Molenkamp, G. Schmidt, A. N. Slavin, V. S. Tiberkevich, N. Vukadinovic and O. Klein
Bistability of vortex core dynamics in a single perpendicularly magnetized nanodisk
Phys. Rev. Lett. **120**, 177602 (2009)

C. Kumpf, A. Stahl, I. Gierz, C. Schumacher, S. Mahapatra, F. Lochner, K. Brunner, G. Schmidt, L. W. Molenkamp and E. Umbach
Structure and relaxation effects in thin semiconducting films and quantum dots
Phys. Stat. Sol. (c) **4**, No. 9, 3150-3160 (2007)

F.Lochner, C. Gould, G. Schmidt and L. W. Molenkamp
High magnetic and crystalline NiMnSb grown by MBE
In progress

A. Riegler, F. Lochner, C. Gould, G. Schmidt and L. W. Molenkamp
Substrate induced uniaxial anisotropy in NiMnSb(111) layers
In progress

A. Riegler, F. Lochner, C. Gould, G. Schmidt and L. W. Molenkamp
Very high q-factor for spin torque oscillator in zero field
In progress

A. Riegler, F. Lochner, C. Gould, G. Schmidt and L. W. Molenkamp
Magnetostatic modes in arrays of sub-micrometer sized elements of NiMnSb(001)
In progress

Curriculum vitae

Danksagung

An dieser Stelle möchte ich mich bei allen Menschen bedanken, die zum Gelingen dieser Dissertation beigetragen haben.
Besonderer Dank gilt Prof. Dr. Laurens Molenkamp, der mir die Möglichkeit gegeben hat, an seinem Lehrstuhl meine Promotion durchzuführen, und der mir mit immer neuen Denkanstößen zum Gelingen dieser Arbeit verholfen hat.
Ebenfalls großen Dank verdient Prof. Dr. Georg Schmidt, der ehemalige Leiter der Spintronics-AG, für seine gute Betreuung und sein immer offnes Ohr hinsichtlich Fragen und Korrekturen. Desweiteren danke ich seinem Nachfolger, Dr. Charles Gould, zum einen für die Weiterführung der Arbeit und zum anderen für seinen unermüdlichen Forscherdrang, welcher mir immer wieder neue Impulse gegeben hat.
Danken möchte ich meinen ehemaligen Bürokollegen, Matthias Mühlbauer, Christoph Brüne und besonders Andreas "Herbert" Roth, für die unzähligen lustigen Stunden in unserem Büro.
Ein weiteres großes Dankeschön gilt Volkmar Hock, für die große Hilfsbereitschaft in allen Reinraumangelegenheiten und für die amüsanten Fussballdiskussionen.
Weitere Worte meines Dankes richten sich an Alfred Schönteich und Martin Zipf für sämtliche Reparaturen in Situationen, in denen das Ultrahochvakuum kein Ultrahochvakuum mehr sein wollte und für alle sonstigen unverschuldeten und selbstverschuldeten Havarien im MBE-Labor.
Den technischen Assistenten Petra Wolf-Müller und Anita Gebhard danke ich für die unzähligen eingeschleusten und wieder ausgeschleusten Proben und die durch beide verbreitete nette Atmosphäre im Labor.
Dr. Claus Schumacher für die vielen aufschlussreichen Diskussionen über Epitaxie und MBE im Allgemeinen.
Lars Ebel für so manche Diskussion über MBE sowohl im Labor als auch in der Cafeteria.
Bastian Büttner für die große Hilfe bei den Messungen am Kryostaten.
Andreas Riegler für die Unterstützung bei den FMR Messungen.
Christian Kehl und Sven Issing für die Bereitstellung von kalkfreiem Kaffee aus ihrer Philips Senseo Kaffemaschine.
Jonas Bachmann und Manuel Poller für das gemeinsame Lösen von Übungsblättern, das Lernen auf Klausuren und die Abenteuer im nächtlichen Würzburg.
Großer Dank gilt den Personen, welche auf vielfältige Weise zum Gelingen dieser Arbeit beigetragen haben:
Matthias Grünewald, Stefan Mark, Utz Bass, Holger Thierschmann, Dr. Tanja Borschenko, Matthias Albert, Dr. Tobias Kiessling, Alexander Frei, Dr. Peter Bach und Dr. Peter Grabs.

Meinen beiden Katzen Chloe und Micky für das Zerknabbern von so manchen Unterlagen. Meinen beiden Hunden Asta und Hutch, die mir durch lange Spaziergänge wieder einen klaren Kopf verschafften, um die Dissertation zu vollenden.
Meinen Eltern und Schwiegereltern für die finanzielle Unterstützung während meines Studiums und der Promotionszeit.
Und last but not least meiner Frau Corinna, die so manch stressige Zeit mit mir durchmachen musste, mich aber immer unterstützt und zum Weitermachen ermutigt hat,wenn es mit dem Kristallwachstum mal wieder nicht so vorwärts ging, wie es sollte.

Erklärung an Eides statt

gemäß §5 Abs. 2 Ziff. 2 und 5
der Promotionsordnung der
Fakultät für Physik und Astronomie
der Universität Würzburg
vom 22. September 2003

Hiermit erkläre ich ehrenwörtlich, dass ich die Dissertation selbstständig und ohne Hilfe eines Promotionsberaters angefertigt und keine weiteren als die angegebenen Quellen und Hilfsmittel benutzt habe.

Die Dissertation wurde bisher weder vollständig noch teilweise einer anderen Hochschule mit dem Ziel, einen akademischen Grad zu erwerben, vorgelegt.

Am 10. März 2006 wurde mir von der Universität Würzburg der akademische Grad *Diplom-Ingenieur (Univ.)* verliehen.

17.05.2011

Florian Lochner